COMPARISON OF AUTOMATIC AND SEMI-AUTOMATIC METHODS
FOR CLASSIFICATION OF SIDE SCAN SONAR IMAGERY

Tiago Rafael de Barros Pereira[1], Helenice Vital[1],
André Giskard Aquino da Silva[2] and Cecília Alves de Oliveira[1]

ABSTRACT. The main scope of this paper is the analysis of seafloor classification using acoustic remote sensing data. These data were acquired in a hydroacoustic survey of bathymetry and sonography using an interferometric swath bathymetry system. The study area is a sector of the internal northeast Brazilian shelf adjacent to the Ponta Negra beach - Natal (RN, Brazil). The objective of the work is to identify and draw the different textural patterns, which characterize the seafloor of the study area. In addition, two approaches for textural classification of sonograms were compared and evaluated, which were: Automatic Gray Level Co-occurrence Matrix (GLCM) classification available in SonarWiz software; and the semi-automatic Maximum Likelihood, available in ArcGIS software. The comparison tested the capacity for identifying and drawing the textural patterns distribution. The automated classification identified 5 patterns while on the semi-automated 6 patterns were identified. It was made the correlation between the textural patterns found in each classification, besides the correlation between textural patterns and the levels of intensity of reflectance presents on the sonogram.

Keywords: sonography, textural classification, textural patterns, hydroacoustic.

RESUMO. Este trabalho foi realizado a partir da análise de dados geofísicos adquiridos em levantamento hidroacústico de batimetria e sonografia utilizando um sonar interferométrico EdgeTech 4600. A área de estudo é uma porção da plataforma interna do nordeste brasileiro adjacente Natal (RN). O objetivo deste trabalho é identificar e delimitar os diferentes padrões texturais que caracterizam o substrato marinho da área de estudo. Adicionalmente, são avaliadas e comparadas duas abordagens distintas de classificação textural de sonogramas, sendo elas: a classificação automática GLCM disponível no *software* SonarWiz, e a classificação semi-automática máxima verossimilhança (*Maximum Likelihood*) disponível no *software* ArcGIS. A comparação foi realizada com base na capacidade de identificação e delimitação da distribuição dos padrões texturais. A utilização da classificação automática identificou 5 padrões, enquanto que, na classificação semi-automática 6 padrões foram identificados. Foi feita a correlação entre os padrões texturais encontrados em cada classificação, além da correlação entre os padrões texturais e os níveis de intensidade de reflectância presente no sonograma.

Palavras-chave: sonografia, classificação textural, padrões de textura, hidroacústica.

[1]Universidade Federal do Rio Grande do Norte, Centro de Ciências Exatas e da Terra - CCET, Departamento de Geologia, Campus Universitário – Lagoa Nova, 59078-970, Natal, RN, Brazil – E-mails: tiagogeof@gmail.com; helenice@geologia.ufrn.br; cecieperi@hotmail.com
[2]University of Kiel, Germany – E-mail: ag@gpi.uni-kiel.de

INTRODUCTION

The intensification of marine resources exploration requires the application of geophysical techniques for detailed seabed mapping (Simons & Snellen, 2009). Advances in high-resolution hydroacoustic techniques for seabed imaging led to the increase in mapping accuracy, quality and velocity. Such advances improved the geological, biological and geomorphological classification of the seabed allowing the identification of geohabitats (Brown & Collier, 2008).

The accurate mapping of geohabitats, seabed morphology and sedimentology (i.e. textural classification of sonograms) are the first necessary steps for the implementation of hydro-ways, construction of new harbors, installation of structures for hydrocarbons exploration and production (E&P), and other mineral resources (e.g. gas hydrates, manganese nodules, sand extraction, etc.). Moreover, seabed mapping is an important tool for coastal zone management and coastal protection projects (Che Hasan et al., 2014).

Seabed mapping for bottom classification is based on the analysis of the backscattered hydroacoustic wave (Blondel, 2009). Different types of substrate result in different intensities of the backscatter (Che Hasan et al., 2014). However, the seabed sedimentological (or textural) classification requires in situ samples (e.g. sediment samples, observational dives, video records of seabed, etc.) to validate the textural classification based on backscatter intensity. Moreover, textural classification using backscatter signal is based on the visual observation of the different patterns on the sonogram, therefore, dependent of the interpreter's experience and knowledge of the area (Souza, 2006). Automatic and semi-automatic classifications have been used to minimize subjectivity on the seabed classification process, which is based on statistical analysis of the backscatter signal to define the spatial limits of the textural classes which are present in a given location.

In this sense, this work targeted the comparison between automatic and semi-automatic seabed classification, using side scan sonar backscatter signal, of the inner shelf adjacent to Ponta Negra beach (Natal-RN), which is located at the northeast Brazilian coast (approximately -5.8° latitude) (Fig. 1).

The area has approximately 18.0km², with depths varying between 2.0m and 13.0m. The continental shelf is ∼25.0km wide with the shelf break occurring at ∼60.0m water depth. In the adjacent Ponta Negra beach, the Morro do Careca sandy costal dune occurs on top of a rocky headland. Tides on this location are semi-diurnal with amplitudes ranging from ∼1.4m to ∼2.2m, for neap- and spring tide, which characterizes a meso-tidal regime.

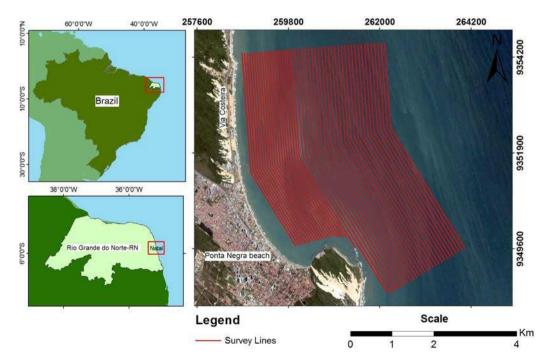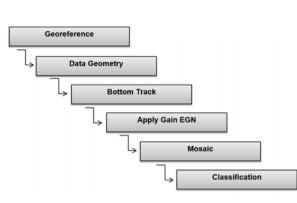**Figure 1** – Location of the study area and survey lines.

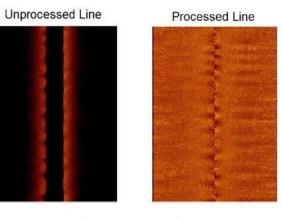**Figure 2** – Flowchart presenting the steps to process the sonograms.

Figure 3 – Raw (left) and processed (right) sonograms showing the improvement in image quality.

METHODOLOGY

The data were acquired with an integrated interferometric system EdgeTech 4600 which records simultaneously high resolution multi-beam bathymetry and side scan sonar. It has a maximum angular coverage of 200° which allows covering 12 times the water depth (limited to a maximum of 140m swath coverage for bathymetry data acquisition) and operates at 54kHz.

A GPS, a depth sounder, a motion reference unit and a gyrocompass were used in the survey to record the position information of sonar data. The side scan sonar data were acquired with 150m swath coverage. The insonified area covered approximately 18km² totaling 50 coastal parallel lines ranging of 4.9km to 5.5km length. The survey lines were spaced 60m to 80m from each other, depending on water depth (Fig. 1).

To process the bathymetry data the software Hypack 2014 was used to integrate sound velocity, tide and bathymetry data. The SonarWiz 5.0 software was applied to process the sonograms following the steps described in the flowchart of Figure 2.

The sonograms were georeferenced (Datum WGS84, UTM projection Zone 25S), and the swath percentage was defined based on visual inspection of the backscatter intensity of the far beams in relation to the near beams, when imaging the same textural sediment type. This evaluation revealed that using 90% of swath coverage would guarantee both total (100%) bottom coverage (yet minimizing data overlap) and uniformity of backscatter data across swath. Moreover, the bottom tracking tool was used to eliminate the blank area at nadir. The Empirical Gain Normalization (EGN) standardized colors of areas which have similar reflectance (i.e. same backscatter signal intensity) using the average of amplitudes of all sonogram cells.

The processing flow (Fig. 2) significantly improved the sonograms quality and facilitated visual identification of the textural patterns (Fig. 3).

The side scan sonar mosaic was done following reflectance tones and was adjusted to initiate seabed textural classification.

Automatic classification was performed using the software SonarWiz 5.0 by applying the Gray Level Co-occurrence Matrix (GLCM). In this classification the following image attributes were used: standard deviation, entropy, auto-correlation and pixel contrasts.

Semi-automatic classification was performed using the software ArcGIS. In this classification the number of classes was determined by visual analysis of the sonogram which had the color tone variation as the major parameter for determining textural classes. The software uses Maximum Likelihood to determine the spatial limit between adjacent classes. The validation of the textural classification was done using sediment samples archived at the Geologia e Geofísica Marinha e Monitoramento Ambiental (GGMMA) laboratory located at Universidade Federal do Rio Grande do Norte (UFRN).

RESULTS

Bathymetry

Bathymetry depth ranges in the area from 13.9m to a minimum of 2.5m and mean depths of 8.29m (Fig. 4).

Sonography

In the post processing of sonography data all files were amalgamated to produce a mosaic (Fig. 5).
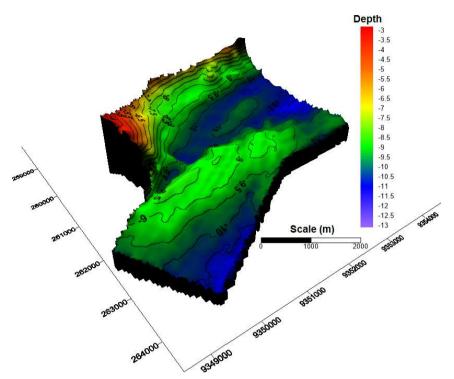
Figure 4 – Digital Terrain Model.

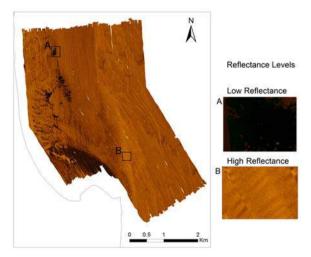**Figure 5** – Sonography mosaic.

Figure 6 – Mosaic of the sonograms showing details of low (A) and high (B) reflectance sites.

The color tones are directly related to reflectance (backscatter intensity), hence, regions showing dark color tones are characterized by low reflectance (high attenuation of the acoustic wave) while regions of bright color tones are characteristic of high reflectance (low attenuation of the acoustic wave) (Fig. 6).

For ease description and understanding of the results, the survey area was divided in three zones according to their respective distance from the shoreline (proximal, intermediate, distal) (Fig. 7).

CLASSIFICATION

Automatic Classification

In GLCM automatic classification 5 textural patterns were identified named P1 to P5 (Fig. 8).

In the proximal zone the pattern P1 appears more frequently with 42.74% occurrence along the entire zone (Table 1). Textural pattern P2 covers 7.66% of the proximal zone, occurring in contact to P4. In turn, P4 covers approximately 16.4% of the proximal zone, occurring predominantly on the south. P3 correspond to 32.64% of the proximal zone and occurs predominantly at the central part of this zone.

On the intermediate zone all textural patterns were present, however, P1 covers 77.59% of this zone (Fig. 8). P3 is the second most representative textural pattern found on the intermediate zone. P1 and P3 represent 92.55% of the textural variability of this one, with P3 occurring predominantly at east and west extremities of this zone (Table 1, Fig. 8). The textural pattern P2 occurs predominately on the south part of this zone and corresponds to 5.97% of it. The pattern P4 covers 1.36% of the textural variability of this zone and its occurrence is concentrated on the center west portion (Fig. 8).
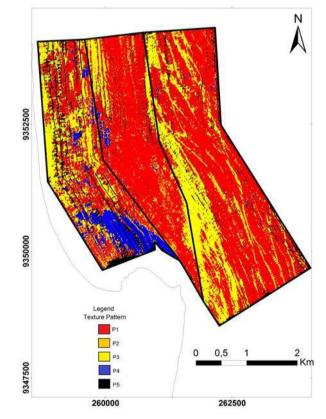

Figure 7 – Division of the survey area in three zones: proximal, intermediate and distal.

Figure 8 – Automatic classification GLCM done in SonarWiz 5.0.

On the distal zone also predominates the textural patterns P1 and P3 which correspond to 67.16% and 31.63%, respectively (Table 1). P3 occurs predominantly on the west part of this zone while P1 occurs throughout the entire zone. Together P2 and P4 represent 1.03% of the textural variability of this zone; hence, the distal zone has the least textural variability when compared to the proximal and intermediate zones (Fig. 8).

In general, the textural pattern P1 occurs more frequently than all others added, corresponding to 63.60% of the survey area. P3 was the second more abundant textural pattern, covering 27.48% of the survey area. P4 and P5 together represent 4.74% and 0.27% of the survey area, respectively, while P2 covers 3.92% (Table 1).

Table 1 – Percentages of the textural patterns found on the survey area according to the automatic classification.

Textural patterns	Proximal	Intermediate	Distal	Total area
P1	42.74%	77.59%	67.16%	63.60%
P2	7.66%	5.97%	0.74%	3.92%
P3	32.64%	14.96%	31.63%	27.48%
P4	16.40%	1.36%	0.29%	4.74%
P5	0.56%	0.12%	0.18%	0.26%
	100.00%	100.00%	100.00%	100.00%

Table 2 – Percentages of the textural patterns found on the survey area according to the semi-automatic classification

Textural patterns	Proximal	Intermediate	Distal	Total area
P1	42.71%	65.23%	60.11%	56.62%
P2	12.15%	14.24%	4.18%	8.98%
P3	21.90%	14.49%	34.02%	25.62%
P4	4.49%	0.87%	0.51%	1.70%
P5	8.92%	3.84%	0.95%	3.90%
P6	9.83%	1.33%	0.23%	3.18%
	100.00%	100.00%	100.00%	100.00%

Semi-automated classification

On the semi-automated classification 6 textural patterns were identified named P1 to P6 (Fig. 9). The proximal zone shows highest heterogeneity among the three zones (Fig. 9). P1 is the textural most abundant pattern, covering 42.71% occurring predominantly on the west part of this zone (Fig. 9). P3 is the

second more abundant pattern of this zone covering 21.90% of it, and found preferably to the east part. P2 represents 12.15% of the proximal zone occurring in contact to P1and P5. In turn, P5 correspond to 8.92% of the textural variability of this zone, associated to P6 and P2. The textural pattern P6 corresponds to 9.83% of this zone and it is found on the south. (Fig. 9). P4 represents 4.49% of the proximal zone, found at its central and south parts and always in contact to P6 (Fig. 9).

On the intermediate zone predominates the textural patterns P1, P2 and P3 which add up 93.96% of this zone (Table 1). P1 is the most common, corresponding to 65.23% and occurring throughout the entire zone. P2 and P3 are found with approximately the same frequency (14.24% and 14.49%, respectively). P2 was found predominantly on the center-south portion, while P3 occurs along the east limit and to the northwest. The patterns P4, P5 and P6 add 6.04% of this zone and are found preferably at its midwest portion (Fig. 9).
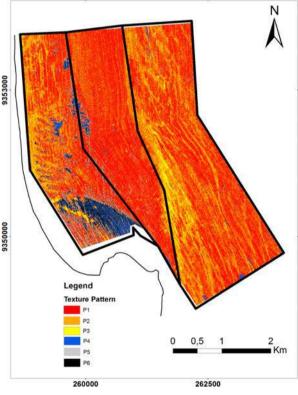

Figure 9 – Semi-automatic classification performed using the software ArcGIS.

The distal zone shows the least textural variability and it is composed predominately by P1 and P3, which add 94.13% of the textural patterns found on this zone (P1=60.11% and P2=34.02%, respectively) (Table 2). P1 occurs throughout the
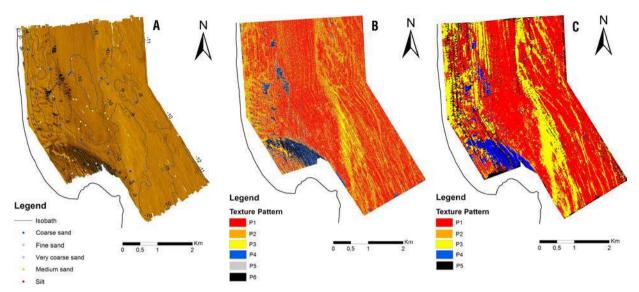
Figure 10 – A – Sonography mosaic with location and textural classification of seabed samples/ B – Semi-automatic classification/ C – Automatic classification

entire zone, however, it is concentrated on the east (Fig. 9). P3 is commonly found at the midwest portion. The textural patterns P2, P4, P5, and P6 add 5.87% of this zone occurring mainly to the east part, where P1 predominates (Fig. 9).

DISCUSSION

Texture is one of the characteristics of a sonogram used to distinguish reflectance levels of a given acoustic wave on the seabed (Lurton, 2002; Blondel, 2009). In this way data from the automatic and semi-automatic classification were associated to textural patterns, which in turn correspond to different reflectance levels (Fig. 10). On the survey area low reflectance was correlated to fine to very-fine grained unconsolidated sediments (i.e. silt or clay) (Fig. 10A). Conversely, regions of high reflectance were correlated to unconsolidated sediment sand (i.e. siliciclastic, carbonate or mixed sands) or bedrocks (i.e. rocks or compacted sediments) (Collier & Brown, 2005; Brown & Collier, 2008).

Automatic classification generates faster results and it is independent from the interpreter's subjectivity on the determination of the number of textural classes present on the sonogram (Souza, 2006). However, its comparison with the semi-automatic textural classification revealed that automatic classification underestimated the number of classes. (Figs. 10B and 10C).

The textural pattern P3 represent the same textural pattern on the classifications automatic and semi-automatic, respectively. They represent maximum reflectance sites, hence, brighter color tones on the sonograms.

P4 on the automatic classification represent the merge of P4 and P6 of the semi-automatic classification. At these sites occurs the highest attenuation of the acoustic wave on the survey area (i.e. lowest reflectance).

The pattern P1 on automatic and semi-automatic classifications, are correlated and represent an intermediate reflectance level.

P2, of the automatic classification, was correlated to P5, of the semi-automatic classification, and they represent sites of low to intermediate reflectance levels. The textural pattern P5, of the automatic classification, represent an artifact resulted from the application of the bottom tracking tool to remove the water column (nadir blank area) from the sonogram. This artifact was not present on the semi-automatic classification.

The textural pattern P2 of the semi-automatic classification could not be correlated to any of the automatic classification. On the sonogram this pattern represents an intermediate reflectance level and considered as a transition from P1 to P5 (Fig. 11).

A qualitative analysis of the products from automatic and semi-automatic classifications reveal that they represent approximately on the same manner the major textural patterns. However, automatic classification drew abrupt contacts between different classes while semi-automatic classification managed to capture a gradational transition between them, which commonly occurs in nature (Wang et al., 1998; Trindade & Ramos-Pereira, 2009).

The automatic classification was not able to resolve the gradational transition between adjacent textural classes.
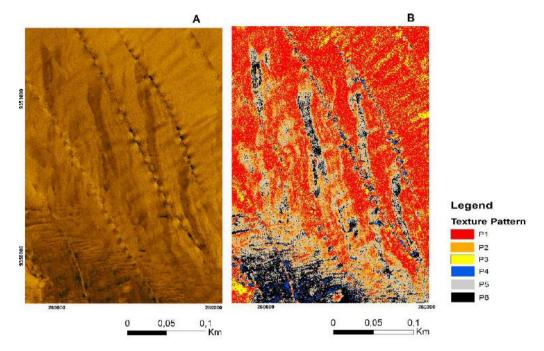
Figure 11 – A - Transition zone from low reflectance to intermediate reflectance/B - Transition zone in semi-automatic classification showing the transition from P5 and P2.
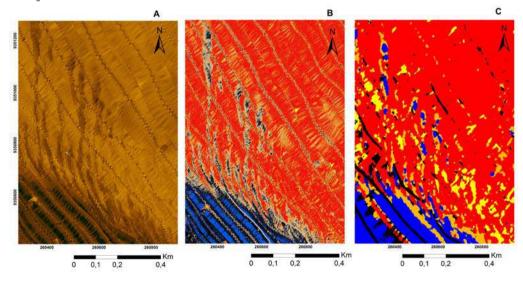

Figure 12 – Transition zone between different textural patterns (A - Sonography mosaic/ B - Semi-automatic classification/ C - Automatic classification).

Moreover, in coastal depositional systems the faciologic distribution is directly related to the hydrodynamic conditions of the area which promote gradational transition between the facies (e.g. beach system) (Wang et al., 1998; Calliari et al., 2003; Trindade & Ramos-Pereira, 2009).

Once the survey area is inserted on the inner continental shelf (Coutinho, 1976; Vital et al., 2010; Vital, 2014) it is likely that such gradational contact occurs and that the semi-automatic classification most accurately described the sedimentological variability on the survey area (Fig. 12).
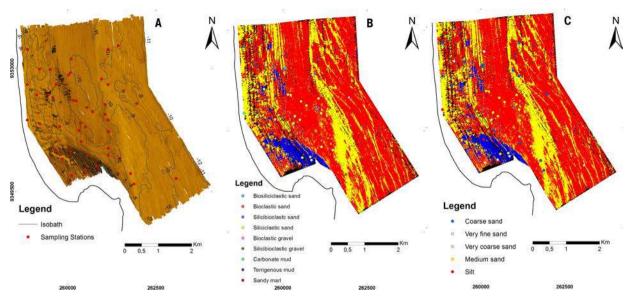
Figure 13 – A - Sonography mosaic and sampling station/ B - Integration between sediment composition and automatic classification/ C - Integration between grain size of sediment and automatic classification.
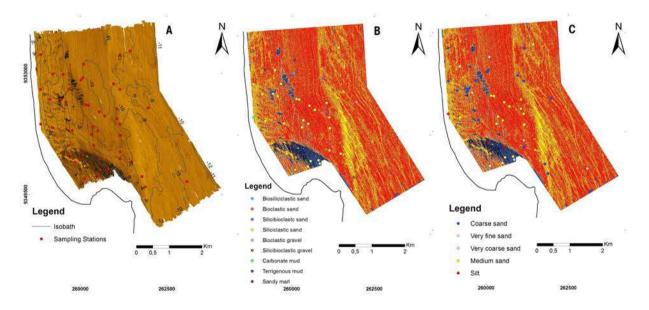

Figure 14 – A - Sonography mosaic and sampling station/ B - Integration between sediment composition and semi-automatic classification/ C - Integration between grain size of sediment and semi-automatic classification.

The comparison with seabed sediment samples reveal that the variability of the reflectance patterns is related not only to grain size but also to sediment composition (i.e. different proportions of siliciclastic versus bioclastic material in the samples). However, low reflectances are still related to fine grained sediment (P4 of automatic classification and P4 and P5 of the semi-automatic classification), while on higher reflectances the variability is associated to compositional changes of the sand (i.e. variations on the bioclastic vs siliciclastic material) (Figs. 13 and 14).

CONCLUSION

The processing steps applied on the sonograms revealed to be efficient on the improvement of the sonogram's quality by reducing color variability over the same bottom type. The EGN

allowed the use of both automatic (GLCM) and semi-automatic (Maximum Likelihood) classifications. The algorithm applied on the automatic classification could not resolve the gradational transition between adjacent sedimentary facies. On the other hand, the semi-automatic classification efficiently resolved the gradational transition between adjacent sedimentary facies. Therefore, the experience of the interpreter still plays a significant role on the analysis of sonograms for textural classification of seabed.

ACKNOWLEDGMENTS

REFERENCES

BLONDEL P. 2009. The Handbook of Sidescan Sonar. Geophysical Sciences. Berlin Heidelberg: Springer-Verlag. 326 pp.

BROWN CJ & COLLIER JS. 2008. Mapping benthic habitat in regions of gradational substrata: An automated approach utilising geophysical, geological, and biological relationships. Estuarine, Coastal and Shelf Science, 78(1): 203-214.

CALLIARI JL, MUEHE D, HOEFEL FG & TOLDO Jr E. 2003. Morfodinâmica praial: Uma breve revisão. Revista Brasileira de Oceanografia, 51: 63-78.

CHE HASAN R, IERODIACONOU D, LAURENSON L & SCHIMEL A. 2014. Integrating Multibeam Backscatter Angular Response, Mosaic and Bathymetry Data for Benthic Habitat Mapping. PLOS ONE, 9(5): e97339. doi: 10.1371/journal.pone.0097339.

COLLIER JS & BROWN CJ. 2005. Correlation of sidescan backscatter with grain size distribution of surficial seabed sediments. Marine Geology, 214(4): 431-449.

COUTINHO PN. 1976. Geologia marinha da plataforma continental Alagoas-Sergipe. Tese (livre docência) - Centro de Tecnologia. Universidade Federal de Pernambuco. Brazil. 112 pp.

LURTON X. 2002. An Introduction to Underwater Acoustics. Springer Science & Business Media. 680 pp.

SIMONS DG & SNELLEN M. 2009. A Bayesian approach to seafloor classification using multi-beam echo-sounder backscatter data. Applied Acoustics, 70: 1258-1268.

SOUZA LAP. 2006. Revisão crítica da aplicabilidade dos métodos geofísicos na investigação de áreas submersas rasas. Doctorate thesis. Instituto Oceanográfico. Universidade de São Paulo, Brazil. 311 pp.

TRINDADE J & RAMOS-PEREIRA A. 2009. Sediment Textural Distribution on Beach Profiles in a Rocky Coast. (Estremadura – Portugal). Journal of Coastal Research, 56(SI): 138-142.

VITAL H. 2014. The north and northeast Brazilian tropical shelves. In: CHIOCCI FL & CHIVAS AR (Eds.). Continental Shelves of the World: Their Evolution during the Last Glacio-Eustatic Cycle. volume 41, p. 35-46. Geological Society of London. URL https://dx.doi.org/10.1144/M41.4.

VITAL H, GOMES M, TABOSA W, FRAZÃO EP, SANTOS CLA & PLÁCIDO JÚNIOR JS. 2010. Characterization of the Brazilian continental shelf adjacent to Rio Grande do Norte state, NE Brazil. Brazilian Journal of Oceanography, 58(SPE1): 43-54.

WANG P, DAVIS RA & KRAUS NC. 1998. Cross-shore distribution of sediment texture under breaking waves along low-wave-energy coasts. Journal of Sedimentary Research, 68(3): 497-506.

ANALYSIS OF THE PRINCIPAL CONSTITUENTS OF SOLID EARTH TIDES ESTIMATED WITH GRAVIMETRIC AND GNSS DATA IN MANAUS AND BRASÍLIA

Mário A. de Abreu[1], Giuliano S. Marotta[1], Lavoisiane Ferreira[1], Denizar Blitzkow[2],
Ana C. O. C. de Matos[2] and João Francisco Galera Monico[3]

ABSTRACT. Solid Earth tide is the periodic displacement due to the tidal force. This effect is present in all geodesic and geophysical observations and should be eliminated when high accuracy surveying is required. It is necessary to determine the amplitudes and phases of the harmonic constituents to estimate the terrestrial tide effect magnitude. This article presents a methodology for estimating and analyzing the amplitudes and phases of the solid Earth tide principal constituents from gravimetric/GNSS observations. The methodology was applied to data collected in the Manaus/AM and Brasília/DF stations, Brazil, to determine the amplitude and phase values for the long period, monthly, diurnal and semidiurnal constituents, besides determining the time required for the convergence of the estimated constituent values. The estimated amplitude and phase values, using gravimetric data, converged between the 2nd and 6th months of the time series. For the positioning observations, the constituents values converged between the 2nd and 17th months of the data series, except for the long period constituent, which requires a longer time series to obtain satisfactory values for both methods. The results show that the solid Earth tide constituents were better estimated by the gravimetric data compared to the positioning data considering the series analyzed.

Keywords: gravimetry, GNSS, solid Earth tide, tidal constituents.

RESUMO. Maré terrestre é o deslocamento periódico decorrente da força de maré. Este é um efeito que deve ser eliminado quando se deseja realizar levantamentos nos quais é necessária alta acurácia tanto em observações geodésicas quanto geofísicas. Para estimar o efeito de maré terrestre deve-se determinar as amplitudes e fases de suas componentes harmônicas. Este artigo apresenta uma metodologia para a estimativa das amplitudes e fases das principais componentes de maré terrestre, a partir de observações gravimétricas/GNSS. A metodologia foi aplicada a dados coletados em estações instaladas em Manaus/AM e Brasília/DF, Brasil, resultando na determinação dos valores de amplitude e fase para componentes de longo período, mensais, diurnas e semidiurnas, além da análise da convergência dos valores estimados para estas componentes. As amplitudes e fases calculadas, utilizando dados gravimétricos, convergiram entre o 2° e o 6° mês analisados, enquanto para os dados de posicionamento a convergência ocorreu entre o 2° e o 17° mês observado, com exceção da componente de longo período, que não pôde ser determinada em ambos os métodos. Para o período analisado, as componentes de maré terrestre foram melhor estimadas utilizando dados gravimétricos, se comparadas aos resultados obtidos com dados de posicionamento.

Palavras-chave: gravimetria, GNSS, maré terrestre, componentes de maré.

---

[1]Universidade de Brasília, Observatório Sismológico, Campus Universitário Darcy Ribeiro, SG 13, Asa Norte, 70910-900, Brasília, DF, Brazil. Phone: +55(61) 3107-0912 – E-mails: mario.abreu@ibge.gov.br, marotta@unb.br, lavoisiane@outlook.com

[2]Universidade de São Paulo, Escola Politécnica, Departamento de Engenharia de Transportes, Prédio da Engenharia Civil, Cidade Universitária, Av. Prof. Almeida Prado, travessa 2, no. 83, 05424-970, São Paulo, SP, Brazil. Phone: +55(11) 3091-5501 Fax: +55(11) 3091-5716 – E-mails: dblitzko@usp.br, acocmatos@gmail.com

[3]Universidade Estadual Paulista Júlio de Mesquita Filho, Faculdade de Ciências e Tecnologia, Departamento de Cartografia, Centro Educacional, Rua Roberto Simonsen, 305, 19060-900, Presidente Prudente, SP, Brazil. Phone: +55(18) 3229-5511 Fax: +55(18) 3229-5353 – E-mail: galera.monico@unesp.br

INTRODUCTION

Solid Earth tide is the phenomenon resulting from the tidal force, through the Earth crust movement, which can be observed by the periodic displacement measured on the Earth surface. The tidal force is understood as the difference between the Earth mass center and surface forces due to the gravitational effect.

Solid Earth tide studies started in 1863, according Ekman (1993), when William Thomson introduced the idea that the Earth is not a completely rigid body, but subject to viscoelastic deformations, especially due to the lunisolar attraction. Now a day, the solid Earth tide studies have become more important due to the development of geophysical and geodetic methods, and new data observation techniques, which improved measurement accuracy so that previously neglected effects must be corrected now.

Currently, the global models used to reduce the effect of solid Earth tide were developed using gravity field observations and displacements measured on the Earth surface. Therefore, more refined and accurate models require densifying the observations and, for this purpose, gravity meters and GNSS receivers prove to be very useful.

Superconductor gravimeters are considered the most accurate technique for estimating gravity variations caused by solid Earth tides, but relative gPhone gravimeters are also effective for observing the phenomenon. Based on gravimetric surveys, several studies were conducted to understand better the solid Earth tide effect, among which Baker & Bos (2003); Arnoso et al. (2011); Miranda et al. (2015); Middlemiss et al. (2016) and Benedito et al. (2017).

In Geodesy, since the 1980s, Very Long Baseline Interferometry (VLBI) observations have been used to analyze solid Earth tide effects, as seen in Krásná et al. (2012). More recently, GNSS has been presented as a useful tool to study the crustal movement since it allows continuous observations, has good accuracy, besides the large number of stations distributed on the Earth's surface. When using GNSS to monitoring solid Earth tide, it is necessary to take into account the errors related to the satellites, receivers and signal propagation, besides the deformational effects related to the oceanic, atmospheric and hydrological loads and the pole movement as well. These errors and effects must be analyzed and removed to obtain a reliable modeling for this phenomenon. Among the several works using GNSS to study the solid Earth tide, Watson et al. (2006); Ito et al. (2009); Yuan (2009); Yuan et al. (2013) and Alihan et al. (2017) are highlighted.

Understanding the deformations resulting from the solid Earth tides is important because this effect is present in all geophysical and geodetic observations while having a significant impact on the Earth geological processes. In this sense, studies by Kasahara (2002); Cochran et al. (2004); Chen et al. (2012) and Varga & Grafarend (2019) demonstrated that tides could contribute to Earthquakes and volcanism.

The objective of this study is to estimate the principal solid Earth tide constituents using gravimetric and positioning observations conducted in two stations in Manaus and Brasília, thus contributing to improve the knowledge for modeling this important effect since the solid Earth tide modeling is still poorly understood, with very limited application in Brazil.

METHODOLOGY TO DETERMINING THE SOLID EARTH TIDE CONSTITUENTS

To determine the solid Earth tide constituents, the data must be treated to decrease the uncertainty inherent to the identification and estimation of these constituents. For this, the gravimetric and positioning data must be edited, corrected and processed.

Gravimetric Data Editing, Correcting and Processing

The flowchart in Figure 1 shows the sequence followed for editing, correcting and processing the gravity variation data measured continuously by a relative gravimeter.

The data editing consists of identifying and removing the spikes from the time series so that only the measured periodic signal remains. From the analysis of the time series, the spikes are identified and removed. Only the most discrepant spurious points need to be eliminated, and this can be done visually. These removed spikes are usually related to recording problems or seismic movements recorded by the equipment. The purpose of spike removal is to maintain only the periodic signal measured by the gravimeter, to improve the accuracy when determining the solid Earth tide constituents. However, the removed spikes leave gaps where the missing data were in the series as seen in Figure 2.

Subsequently, the data were corrected for the gravimeter level (Melchior, 2008), atmospheric pressure (Boy et al., 2002) and barometric compensation (Warburton & Goodkind, 1977), thus minimizing the atmospheric effects recorded by the gravimeter. Other important corrections to be considered are related to the pole movement effect (Jekeli, 2012) and ocean load (Farrell, 1972).

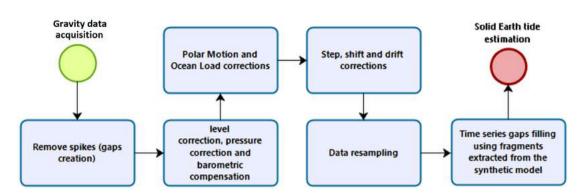The steps and shift (instrumental displacement) must also be corrected.

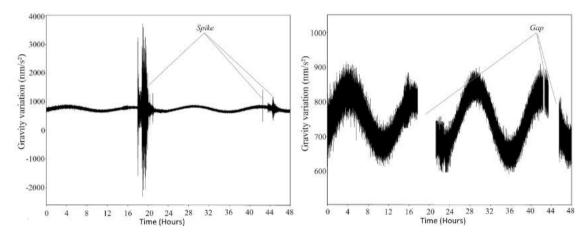**Figure 1** – Gravity data processing sequence.

Figure 2 – The graph on the left shows the spikes in the raw signal data extracted from a gravimeter. The graph on the right shows the same signal, after eliminating the spikes, and the resulting gaps.
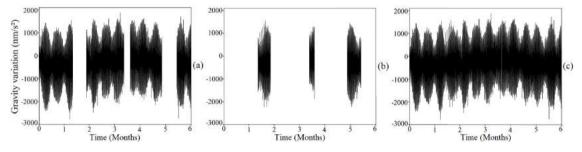

Figure 3 – (a) graph shows the corrected signal with gaps; (b) graph shows the sections extracted from the theoretical model of the solid Earth tide to fill in the gaps; and (c) the complete corrected signal, resulting from the sum of the signals in (a) and (b).

In addition, it is important to correct the drift using a polynomial equation that fits the observed data. To correct these instrumental errors, the parameters of the recommended functional model can be obtained by the LSM (least squares method):

$$F(t) = a + bt + ct^2 + \sum_{i=1}^{n} dH(t)_i \qquad (1)$$

a is the shift (instrumental displacement); t is the time; b and c are the drift coefficients; d is the step; and H is the step function.

To free the time series from the discontinuities, the gaps can be filled using fragments of the theoretical solid Earth tide model. The information at the starting and ending sections of each gap left by the spike removal is used to extract the data using the theoretical model of solid Earth tide to fill in the gap, resulting in a

non-disruptive time series. The result of extracting the gaps from the theoretical signal and the filling in of the observed signal is shown in Figure 3.

It is important to fill in the gaps of the observed data series using the synthetic model as a reference since interpolation methods would not allow the complete reconstruction of the solid Earth tide signal while the theoretical model calculates a signal closer to the observed one.

The gap filling is necessary because lack of data in the time series can be interpreted as the beginning of a new observation sequence during processing, resulting in a greater uncertainty associated with the results. A continuous time series (Fig. 3c), without gaps, must be used for determining the constituents more accurately.

To estimate tidal constituents, it is important to define which of the various constituents to determine. According to Petit & Luzum (2010), tides have 11 principal constituents, shown in Table 1.

i is Doodson number, t the mean solar time, τ the mean lunar time, s variation of the moon declination, p the revolution of the mean lunar perigee, and h one-year period (365.25 days).

After defining the constituents to be estimated, it is convenient to analyze the spectrum of the observed signal as to identify the frequency intervals (Fig. 4) where the desired constituents are located.

The frequency intervals identified in the spectrum can be entered in the processing and used to determine the amplitude factor and the phase difference of the solid Earth tide harmonic constituents.

The tidal constituents can be determined using the tidal generating potential presented by Hartmann & Wenzel (1995):

$$V(t) = \sum_{l=1}^{l_{max}} \sum_{m=0}^{l} \left(\frac{r}{a}\right)^l P'_{lm} \cos(\theta) \sum_i [C_i^{lm}(t) \cos(\alpha_i(t)) + S_i^{lm}(t) \sin(\alpha_i(t))] \qquad (2)$$

Where $C_i^{lm}(t)$ and $S_i^{lm}(t)$ are the time-dependent tidal potential coefficients; P'_{lm} are the fully normalized Legendre functions; a s the semi major axis of the reference ellipsoid; t s the time from J2000 in Julian centuries; $l = 1, \ldots, l_{max} = 6$ and m are the degree and order of the series, respectively; r, θ and λ are the geocentric spherical coordinates; and $\alpha_i(t) = m\lambda + \sum_{j=1}^{11} k_{ij} arg_j(t)$ are the astronomical arguments.

Positioning Data Editing, Correcting and Processing

The positioning dataset collected by the GNSS stations was edited, standardized and processed using the methodology outlined in Figure 5 and explained below.

First, the GNSS data were checked for file integrity to detect any flaws that could affect processing using specific software, such as the TEQC (Translation, Editing, and Quality Check), described by Estey & Meertens (1999).

he GNSS coordinates can be determined by applying the kinematic mode (Monico, 2007) of the PPP (Precise Point Positioning) method (Zumberge et al., 1997). Also, processing should use precise orbits, as well as other corrections such as satellites clocks, antenna phase center, tropospheric and ionospheric effects, pole movement, and oceanic load for obtaining coordinates that are more precise. The solution is static, at first, to solve the ambiguities and determine the tropospheric correction parameters. After solving the ambiguities, the positioning in the kinematic mode is performed to improve positioning quality.

The solid Earth tide constituents are determined from the calculated latitude (ϕ), longitude (λ) and geometric altitude (h) coordinates. It is important to define the constituents to be estimated. Table 1, shown above, shows the 11 major tidal constituents, and Solid Earth tide constituents can be estimated from the astronomical arguments.

STUDY AREA

The used data were collected in the gravimetric and GNSS stations located in Manaus and Brasília, Brazil.

In Manaus, the gravimeter and the GNSS receiver were installed at CENSIPAM (Operational and Management Center of the Amazon Protection System), shown in Figure 6. Manaus is located at 92 m average altitude, having 2300 mm average annual rainfall, with very well defined rain and dry seasons. It is located in the Amazon basin, a region of great scientific interest due to the global environmental and climatic relevance and biodiversity (Costa et al., 2012). Additionally, this region lacks gravimetric data due to the difficult access for field surveys.

In Brasília, the gravimeter was installed at Seismological Observatory of the Universidade de Brasília (UnB), and the GNSS receiver was located in the IBGE Ecological Reserve, as seen in Figure 6. Brasília is located in the central Brazilian plateau, at about 1170 m average altitude while the 1540 mm average annual rainfall is 35% less than in Manaus, it is also characterized by very well defined rain and dry periods.

Table 1 – Principal tidal constituents (adapted from Melchior, 1983).

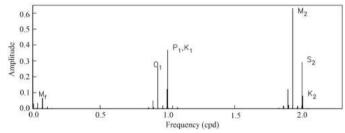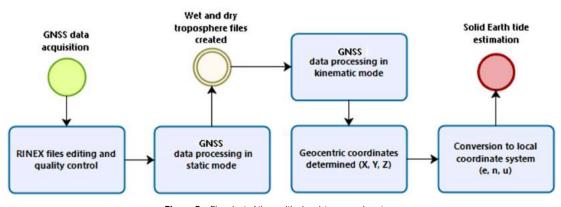| Name	i	Argument	Frequency (°/h)	Source
Long term constituents				
S_{sa}	057.555	$2h$	0.082137	Solar semiannual
M_m	065.455	sp	0.544375	Lunar monthly
M_f	075.555	$2s$	1.098033	Lunisolar fortnightly
Diurnal constituents				
Q_1	135.655	$(\tau s)(sp)$	13.398661	Larger lunar elliptic
O_1	145.555	τs	13.943036	Lunar diurnal
P_1	163.555	τh	14.958931	Solar diurnal
K_1	165.555	$\tau + s$	15.041069	Lunisolar diurnal
Semidiurnal constituents				
N_2	245.655	$2\tau(sp)$	28.439730	Larger lunar elliptic
M_2	255.555	2τ	28.984104	Principal lunar
S_2	273.555	$2t$	30.000000	Principal solar
K_2	275.555	$2(\tau + s)$	30.082137	Lunisolar semidiurnal

Figure 4 – Frequency spectrum expanded to degree 2, showing some tidal constituents (source: Agnew, 2010).

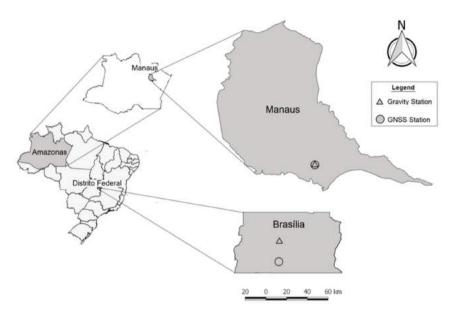**Figure 5** – Flowchart of the positioning data processing steps.

Figure 6 – Map showing the gravimetric and GNSS stations in Manaus and Brasília.

Another important factor for choosing the sites to be studied was the fact that both cities had available time series longer than one year, in addition to active GNSS stations belonging to SIRGAS-CON (Geocentric Reference System for the Americas – Continuous Monitoring) and RBMC (Brazilian Network for Continuous Monitoring of GNSS Systems).

DATA ACQUISITION

The relevant information regarding the acquisition of gravimetric and GNSS data follows.

Gravity Data

The used gravimetric data were obtained by a gPhone gravimeter manufactured by the Micro-g LaCoste, with 0.1 μGal resolution and 1 μGal accuracy (LaCoste, 2018), constructed to allow a low instrumental drift ($\approx$1.5 mGal/month) and recommended for observing periodic signals and, therefore, indicated for studying solid Earth tides.

Both gravimeters were installed on a concrete pillar, isolated from the building, allowing reasonable stability and minimizing noise. The calibration of the gravimeters was done before the beginning of the acquisition of the data and, after, the verification of the gravimetric level was done frequently.

The gravimetric data were generated daily at 1 Hz sampling rate. The gravimeter records more than four channels but only four were used, as follows: continuous gravity measurement,

gPhone level, atmospheric pressure corrections, and barometric compensation, all expressed in μGal.

It is noteworthy that the gravity measurements analyzed in this work were not automatically corrected for any effect.

GNSS Data

The used positioning data were collected in two active GNSS stations, NAUS (installed in 2005) and BRAZ (in 1995) stations. Both stations currently use a Trimble GNSS receiver (model NetR9) connected to a Zephyr Geodetic Model II antenna that enables tracking the GPS, GLONASS, Galileo, and Beidou systems. This equipment static positioning accuracy is $\sim$ 3 mm and 3.5 mm for the horizontal and vertical components, respectively.

The two stations have the data available free of charge through the IBGE (Brazilian Institute of Geography Foundation and Statistics) site.

The GNSS data were stored daily at a 15-second sampling rate ($\approx$ 0.067 Hz) per record in the RINEX format (Receiver Independent Exchange Format).

DETERMINING SOLID EARTH TIDE CONSTITUENTS

The procedures for data editing and processing to determine solid Earth tide constituents using gravimetric and GNSS observations are shown in the sequence.

The procedures were performed on the historical data of both time series covering 21 (from 01/26/2016 to 01/11/2017) and 18 (from 04/25/2016 to 11/11/2017) months in Manaus and Brasília, respectively.

Determining Solid Earth Tide Constituents using Gravimetric Observations

Data preparation for determining the solid Earth tide constituents using gravimetric data obtained by gPhone followed the methodology described in section "Gravimetric Data Editing, Correcting and Processing".

Thus, the first step consisted of removing the spikes of the time series. Subsequently, the data were corrected using information from the gravimeter level, atmospheric pressure, and barometric compensation.

The datasets were also corrected for the pole movement provided by the Paris Observatory and the ocean load generated on the Onsala Space Observatory (OSO) site. The ocean load chosen for this work was the FES2004 (Finite Element Solution 2004), recommended by Petit & Luzum (2010), which takes into account the 11 principal harmonic constituents with their respective amplitudes and phases.

A routine developed in MATLAB was used for the step, shift and drift corrections shown in Eq. (1).

Following the corrections, the data that originally had a one-second sample rate was re-sampled for one minute, using a low-pass filter with a cut-off frequency of 720 cycles per day (Kang et al., 2011), applied to a 480-point moving window, equivalent to 16 hours of observation. Using this window in the data re-sampling allows the difference between the observed and the re-recorded tide frequencies be less than 0.05% (Van Camp & Vauterin, 2005).

The last step of the time series preparation was to remove the gaps from the theoretical solid Earth tide model using a new routine developed in MATLAB.

The signals of the corrected time series are shown in Figure 7.

To estimate the solid Earth tide constituents in this work, we used the 11 principal tidal constituents defined by Petit & Luzum (2010) as shown in Table 1.

The tide potential catalog of Hartmann & Wenzel (1995), computing 12395 tidal waves and totaling 19300 adjusted parameters, was used for calculating the solid Earth tide constituents.

The methodology described in "Gravimetric Data Editing, Correcting and Processing" indicated that the intervals of the tide constituents to be determined were identified by analyzing the spectrum of gravity signal variation of both stations, as seen in Figures 8 and 9. The long period constituent (S_{sa}) could not be accurately identified and, therefore, it is not shown in the charts.

The intervals identified in the spectrum were inserted in the processing and used to determine the harmonic constituents of solid Earth tide.

No filter was used in the processing of the constituents since the filter could affect the calculated frequencies, by minimizing or eliminating relevant variations that might be analyzed.

Firstly, the processing used the data covering one month only, and then another month was added, followed by another month resulting in the processing of three months, and so on until the full-time data series was processed. This method was used to analyze the convergence of the computed values of amplitude, phase and their respective deviations over time.

Figures 10, 11, 12 and 13 show the results obtained after the processing of the 11 principal tide constituents. It should be
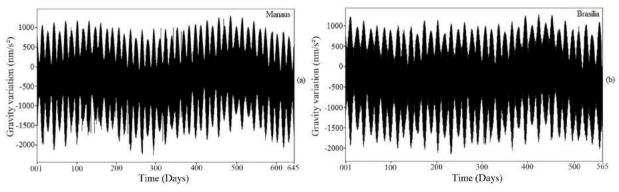

Figure 7 – Corrected time series showing the Manaus station data on the left and the Brasília station data on the right.

noted that the graphs were not normalized to allow visualizing the variability of all the constituents.

The Figures 10 to 13 show the amplitude factor, phase difference, and their respective uncertainties estimated for the long period (S_{sa}), monthly (M_m and M_f), diurnal (Q_1, O_1, P_1, and K_1) and semidiurnal (N_2, M_2, S_2 and K_2) constituents for the time data series of both stations.

The analysis of Figures 10, 11, 12 and 13 allow the following considerations:

- The results for the long-term constituent S_{sa} (Fig. 10) were not satisfactory since it was not possible to determine the values for both stations. This result is because this

constituent requires a time data series covering a longer period to be accurately determined;

- The monthly constituents M_m and M_f (Fig. 11), the amplitude factor and the RMSE begin converging after 3 months and 5 months in the Manaus and Brasília stations, respectively. The analysis of the phase difference graphs and their uncertainties shows that data convergence started from the 6th and 8th months in the Manaus and Brasília stations, respectively.

- Figure 12 shows that the diurnal constituents (Q_1, O_1, P_1, and K_1) begin the convergence of the amplitude factor from the 2nd month, which was similar for both stations.

Figure 8 – Spectrum of the harmonic constituents of Manaus station. (a) shows the complete spectrum; (b), (c) and (d) show respectively the amplified spectrum only for the monthly, diurnal and semidiurnal constituents.
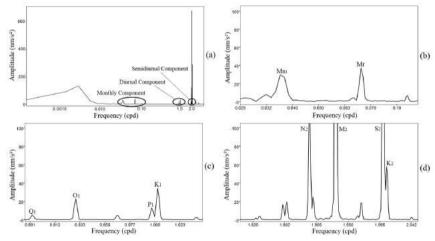

Figure 9 – Spectrum of the harmonic constituents of Brasília station. (a) shows the complete spectrum; (b), (c) and (d) show respectively the amplified spectrum only for the monthly, diurnal and semidiurnal constituents.

Figure 10 – Amplitude factor, phase difference, and respective root mean squared errors (RMSE) estimated for the long period (S_{sa}) constituent of the Manaus (left) and Brasília (right) stations.

Figure 11 – Amplitude factor, phase difference, and respective RMSE estimated for the monthly (M_m and M_f) constituents of the Manaus (left) and Brasília (right) stations. Dotted lines show the change of scale on figure to represent amplitude factor and phase difference.

Figure 12 – Amplitude factor, phase difference, and respective RMSE estimated for the diurnal (Q_1, O_1, P_1, and K_1) constituents of the Manaus (left) and Brasília (right) stations. Dotted lines show the change of scale on figure to represent amplitude factor and phase difference.

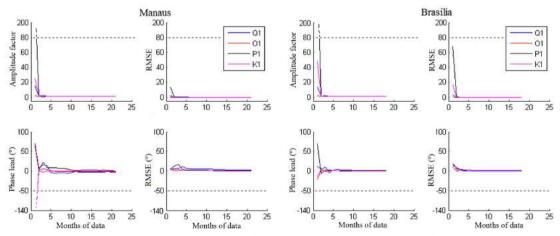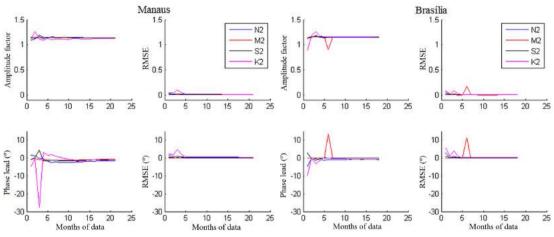**Figure 13** – Amplitude factor, phase difference, and respective RMSE estimated for the semidiurnal (N_2, M_2, S_2, and K_2) constituents of the Manaus (left) and Brasília (right) stations.

In the case of phase differences, the diurnal constituents converged after 5 months, in both stations. The RMSE of the phase differences of the Manaus station indicated a better convergence after 14 months.

- For the semidiurnal constituents (N_2, M_2, S_2, and K_2) shown in Figure 13, the amplitude factor and the RMSE presented a good fit from the 2nd month, in both stations. The calculated phase differences show convergence after 4 months in the Manaus station, except for the K_2 constituent, which varied more and began to converge after 9 months. In the Brasília station, the estimated phase differences converge after 5 months while the M_2 constituent behaves atypically in the 6th month but returns to the convergence line in the subsequent month. Similar behavior was also observed in the amplitude factor of the M_2 constituent, it was concluded that possibly some problem might have caused interference in the constituent frequency.

Tables 2 and 3 show the values of the amplitude factor (δ), phase difference (α), and their respective root mean squared errors (RMSE), for each tide constituent calculated for the Manaus and Brasília stations, respectively. The theoretical amplitude (At) is obtained from the rigid inelastic model of Wahr-Dehant (Dehant, 1987), for a planet without oceans, and the amplitude factor is given by the ratio between the measured amplitudes and those obtained from the rigid inelastic model, according to the local geographic coordinates Costa et al. (2012).

Tables 2 and 3 show that the long period constituent (S_{sa}) could be precisely defined. As mentioned previously, this result stems from the short time series available to determine the constituent since the Manaus and Brasília data series were collected over a period of 21 and 18 months, respectively. Therefore, only one full annual cycle was available becoming impossible to obtain redundancy in the observations.

On the other hand, the amplitude factor of the monthly M_m and M_f constituents was well estimated, but a longer time series is also necessary for determining the phase more precisely. This is evident, especially for the Brasília station since the values of phase difference and the respective RMSE of these constituents were high.

The other diurnal and semidiurnal constituents were well estimated, except for the Q_1 constituent in the Manaus station, which had higher phase difference and RMSE compared to other diurnal constituents.

Figure 14 shows the graphs for the calculated and theoretical tide signals, and the residual resulting from the subtraction of the tide signals from the Manaus and Brasília stations.

The determined monthly, diurnal and semidiurnal constituents were used for reconstructing the calculated tide signal. The long-period tide (S_{sa}) constituent was not included since its results were not satisfactory.

The theoretical tide signal was generated using the same constituents employed for constructing the calculated signal.

The difference between the calculated and the theoretical models, in absolute values, was below 180 and 130 nm/s² for

Table 2 – Solid Earth tide parameters and RMSE estimated from the time data series covering 21 months from the Manaus station, where δ is the amplitude factor and α is the phase difference.

Wave	At (nm/s^2)	δ	RMSE	$\alpha(°)$	RMSE (°)
S_{sa}	31.8501	2.1818	0.4219	-15.3164	11.0136
M_m	33.0586	1.0781	0.0503	-1.0864	2.6786
M_f	68.5361	1.1739	0.0220	2.6360	1.0778
Q_1	6.4742	1.0816	0.0454	-3.2291	2.4022
O_1	33.8560	1.1290	0.0105	-1.6805	0.5309
P_1	15.7176	1.0813	0.0180	0.5982	0.9531
K_1	47.1243	1.0918	0.0067	0.4292	0.3522
N_2	143.0996	1.1380	0.0042	-1.4821	0.2134
M_2	747.7105	1.1391	0.0008	-0.5758	0.0408
S_2	347.5228	1.1379	0.0018	-0.8447	0.0916
K_2	101.0867	1.1223	0.0087	-0.7401	0.4428

Table 3 – Solid Earth tide parameters and RMSE estimated from the time data series covering 18 months from the Brasília station, where δ is the amplitude factor and α is the phase difference.

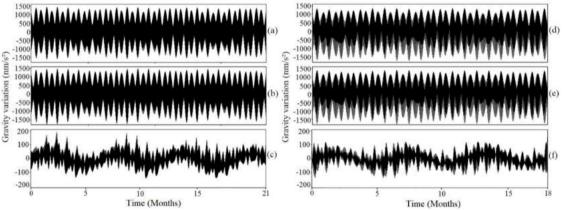| Wave	At (nm/s^2)	δ	RMSE	$\alpha(°)$	RMSE (°)
S_{sa}	25.0458	3.8773	1.8887	0.2638	27.5354
M_m	25 .9961	1.1029	0.2454	-15.0626	12.7522
M_f	53.8944	1.0294	0.0965	7.7549	5.3717
Q_1	32.1543	1.1367	0.0364	-0.1024	1.8369
O_1	168.1466	1.1444	0.0071	-0.0799	0.3576
P_1	78.0620	1.1227	0.0127	0.7165	0.6468
K_1	234.0442	1.1220	0.0047	0.2830	0.2397
N_2	132.9573	1.1485	0.0050	-0.7581	0.2507
M_2	694.7159	1.1560	0.0009	0.0881	0.0467
S_2	322.8918	1.1525	0.0021	0.0332	0.1048
K_2	93.9221	1.1540	0.0099	-0.5257	0.4925

Figure 14 – Tide and residual signals found in the gPhone analysis. The graph on the left shows (a) the calculated tide signal, (b) the theoretical tide signal, and (c) the difference between the calculated and theoretical signals for the Manaus station. The graph on the right shows (d) the calculated tide signal, (e) the theoretical tide signal, and (f) the difference between the calculated and theoretical signals for the Brasília station.

the Manaus and Brasília stations, respectively. This difference is explained by the fact that the computed model allows considering local variations that cannot be quantified precisely by the theoretical model.

The difference between the calculated and theoretical tide signals allows identifying variations of frequency, phase and amplitude. Also, allows identifying a seasonal behavior in both stations, possibly caused largely by the hydrological load. However, to reach a more conclusive answer, it is recommended to conduct studies to investigate this phenomenon further in both sites.

Determining Solid Earth Tide Constituents using GNSS Observations

The GNSS data were treated, processed and the constituents of solid Earth tide were estimated following the methodology presented in section "Positioning Data Editing, Correcting and Processing".

Firstly, the RINEX files for the NAUS and BRAZ stations were edited and standardized. Subsequently, the information regarding the station name, equipment nomenclature and antenna height present in the file header were verified. In addition, the integrity

of the RINEX files was analyzed using the TEQC program to ensure a problem-free processing.

Initially, to determine the geodetic coordinates, the processing was done using the PPP method in the static mode (Monico, 2007), necessary to solve the ambiguities and to estimate the tropospheric correction parameters to be applied in the kinematic processing.

The kinematic processing was set to determine a coordinate every 3600 seconds (1 hour), so that it became possible to evaluate the displacements suffered by the station over time and to analyze the behavior of the altimetric and planimetric components, aiming at extracting information related to solid Earth tide.

The orbit, clock, and antenna phase center (APC) correction files used in the processing were provided by JPL (Jet Propulsion Laboratory) managed by NASA (National Aeronautics and Space Administration). This work used non-fiducial orbits in the processing. According to Blewitt et al. (1992) non-fiducial orbits do not suffer from reference frame errors.

It is noteworthy that, although the GNSS stations have a long historical data series, the calculations included only the data from the same period of the gPhone, to allow comparing the performance of both methods for determining the solid Earth tide constituents.

In addition, the GLONASS, Galileo, and Beidou observations were discarded because the used version 6.4 of the GIPSY/OASIS (GNSS Inferred Positioning System and Orbit Analysis Simulation Software) was able to process only observable GPS.

Table 4 shows the strategy used to determine the GPS coordinates.

After GPS processing, the first calculated coordinate was defined as a reference, subtracted from all subsequent coordinates, so that only the positional variation along the time series was represented. Figure 15 shows the signal processed for the NAUS and BRAZ GPS stations of the constituents East (e), North (n) and Up (u).

The graphs (Fig. 15) are on the same scale to facilitate visualizing the stations undergoing greater altimetric movement compared to planimetric. The signals presented below were used for estimating the solid Earth tide constituents.

The values of the displacement velocity vectors of the NAUS and BRAZ stations were inserted before the tidal constituents estimation to adjust the stations coordinates over time.

The amplitudes and phases of the 11 principal solid Earth tide constituents were calculated using the Tidal Fitting Toolbox developed in MATLAB by Aslak Grinsted of the University of Copenhagen.

The solid Earth tide constituents estimated by GPS followed the same standard set for gPhone. We started by processing the data of one month, adding the subsequent months one by one, and performing new processing for each month added, thus allowing to follow the convergence of the amplitude and phase values along the analyzed time series.

Table 4 – Solid Earth tide parameters and RMSE estimated from the time data series covering 18 months from the Brasília station, where δ is the amplitude factor and α is the phase difference.

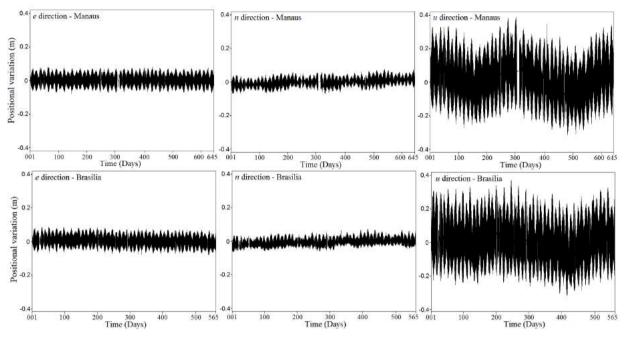| Site	Manaus	Brasília
Position (Lat.; Long.; h)	$-03°\ 01'\ 22.5''$; $-60°\ 03'\ 18.1''$; 93.89 m	$-15°\ 56'\ 50.9''$; $-47°\ 52'\ 40.3''$; 1106.02 m
Observation period	01/26/2016 to 11/01/2017	04/25/2016 to 11/11/2017
Processing interval	3600 seconds (1 hour)	
2nd order ionosphere correction	IONEX (*Ionosphere Exchange*)	
Troposphere mapping function	Vienna Mapping Function (VMF)	
Orbit, clock and antenna phase center corrections	JPL (*Jet Propulsion Laboratory*)	
Ocean load correction	FES2004	
Solid Earth tide correction	Not applied	
Reference frame	ITRF2008 (IGb08 orbits)	

Figure 15 – GPS time series, the three graphs above refer to *e*, *n* and *u* directions of the Manaus station and the three graphs below refer to *e*, *n* and *u* directions of the Brasília station.

The amplitude and phase behavior determined for the long period (S_{sa}), monthly (M_m and M_f), diurnal (Q_1, O_1, P_1, and K_1) and semidiurnal (N_2, M_2, S_2 and K_2) constituents for the components East, North, and Up of the Manaus and Brasília stations can be seen in Figures 16, 17, 18 and 19.

The solid Earth tide constituents were not estimated individually by GPS, therefore, it was not possible to estimate the standard deviation of the computed amplitudes and phases.

A careful analysis of Figures 16, 17, 18 and 19 allows inferring the following:

- The long period constituent S_{sa} (Fig. 16) did not have satisfactory results for both stations. As stated earlier, this constituent requires a longer observation period to be determined with high precision;

- In both stations, the monthly constituents M_m and M_f (Fig. 17) show amplitude values converging from the 7th and 4th months for the *e* and *n* positions, respectively. On the other hand, the *u* component showed a greater dispersion but started to converge from the 14th month. The estimated phases for the two stations begin to converge between the 5th and 10th months, depending on the component but dispersed throughout the analyzed series. Possibly, a longer observation series could lead to more consistent results;

- The diurnal constituents (Q_1, O_1, P_1, and K_1) shown in Figure 18 indicate that the amplitude begins to converge from the 2nd month, a similar behavior was observed for the positional components of the two stations. The phases of the diurnal constituents converge between the 2nd and 5th months, but some results were not satisfactory. A longer historical series would be important to verify whether there is an improvement when determining the phase of these constituents;

- The results for the semidiurnal constituents (N_2, M_2, S_2, and K_2) are shown in Figure 19. The amplitude values show a good adjustment from the 2nd month for both stations. The estimated phases show convergence between the 3rd and 10th months, except for the K_2 constituent, which showed a sudden behavior change for the *n* component in the Manaus station, and started to converge from the 17th month. Similar to the diurnal constituents, some phases have not been well determined, and it is understood that a larger historical series would allow determining the phases with higher precision.

Tables 5 and 6 show the calculated amplitude (A) and phase (F) values for the 11 principal tidal constituents determined for each of the positional components and for the NAUS and BRAZ stations, respectively.

Figure 16 – Amplitudes and phases estimated for the annual constituent (S_sa), for the East (e), North (n) and Up (u) positions of the Manaus and Brasília stations.

Figure 17 – Amplitudes and phases estimated for the monthly constituents (M_m and M_f) for the East (e), North (n) and Up (u) positions of the Manaus and Brasília stations.

Figure 18 – Amplitudes and phases estimated for the diurnal constituents (Q_1, O_1, P_1, and K_1) for the East (e), North (n) and Up (u) positions of the Manaus and Brasília stations.

Figure 19 – Amplitudes and phases estimated for the semidiurnal constituents (N_2, M_2, S_2, and K_2), for the East (e), North (n) and Up (u) position of the Manaus and Brasília stations.
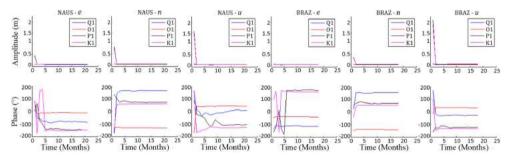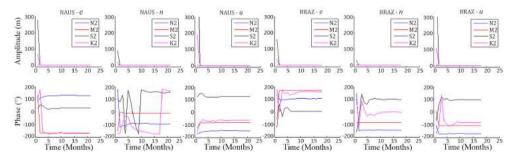
Table 5 – Solid Earth tide parameters estimated from the time series of positioning data of the NAUS station, where A is the amplitude and F is the phase.

Wave	A (m)	F (°)	A (m)	F (°)	A (m)	F (°)
	(e direction)	(e direction)	(n direction)	(n direction)	(u direction)	(u direction)
$S_s a$	0.0013	113.86	0.0018	126.62	0.0227	172.98
M_m	0.0009	146.13	0.0010	87.74	0.0083	69.17
M_f	0.0007	104.38	0.0004	155.72	0.0094	26.03
Q_1	0.0006	-86.17	0.0030	163.80	0.0011	9.82
O_1	0.0024	-11.33	0.0156	-131.10	0.0048	45.04
P_1	0.0010	-148.51	0.0084	72.62	0.0017	-101.18
K_1	0.0033	-147.04	0.0241	61.20	0.0062	-123.22
N_2	0.0074	128.99	0.0006	-95.89	0.0284	-146.95
M_2	0.0378	-167.26	0.0026	-11.24	0.1478	-81.92
S_2	0.0168	30.58	0.0004	155.60	0.0687	122.87
K_2	0.0026	-168.61	0.0004	165.65	0.0120	-63.10

Table 6 – Solid Earth tide parameters estimated from the time series of positioning data of the BRAZ station, where A is the amplitude and F is the phase.

Wave	A (m)	F (°)	A (m)	F (°)	A (m)	F (°)
	(e direction)	(e direction)	(n direction)	(n direction)	(u direction)	(u direction)
$S_s a$	0.0025	134.88	0.0018	120.90	0.0198	-175.09
M_m	0.0008	134.32	0.0023	79.57	0.0088	66.15
M_f	0.0005	78.53	0.0013	22.10	0.0053	25.17
Q_1	0.0012	-115.42	0.0023	154.91	0.0053	-28.89
O_1	0.0050	-41.30	0.0130	-142.22	0.0270	31.60
P_1	0.0023	171.68	0.0071	66.59	0.0141	-123.00
K_1	0.0067	157.16	0.0205	51.82	0.0357	-133.00
N_2	0.0068	105.14	0.0020	-145.43	0.0260	-169.29
M_2	0.0360	167.29	0.0093	-82.81	0.1386	-106.45
S_2	0.0155	3.80	0.0036	98.88	0.0609	99.06
K_2	0.0038	159.16	0.0006	-6.64	0.0109	-80.12

Figure 20 – Residual difference between the observed and adjusted signals, after applying the estimated solid Earth tide correction, to the e, n and u directions of the Manaus station.
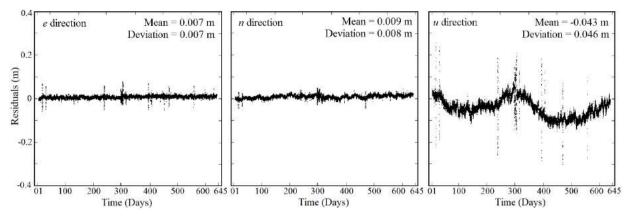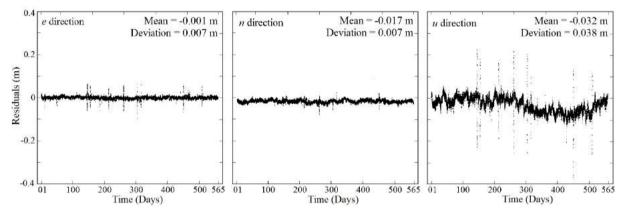

Figure 21 – Residual difference between the observed and adjusted signals, after applying the estimated solid Earth tide correction, to the e, n and u directions of the Brasília station.

Tables 5 and 6 show that the effect of the vertical component (u) of the solid Earth tide is greater than the horizontal components (e and n). This result stems from the fact that the Earth deformation, related to the tidal force, has a greater effect on the altimetric compared to the planimetric component. It is also seen that some estimated phases had negative values, a result that requires further and more accurate investigation.

Figures 20 and 21 show the residue plots that resulted from the difference between the observed and adjusted signals.

The adjusted signal was generated by applying the correction values of the solid Earth tide constituents estimated in this work to the observed signal.

The analysis of Figures 20 and 21 shows clearly that the residuals in the u direction have a cyclical behavior in both stations. This may be related to some other phenomena, such as hydrological load, atmospheric load and other unmodified effects of smaller magnitude.

CONCLUSIONS

This paper presents a methodology for estimating the amplitude and phase values of the principal constituents of the solid Earth tide at Manaus and Brasília, using the gPhone and GPS data. Given the results presented in this paper, some conclusions and recommendations can be presented.

The analysis of the generated data indicated that for the analyzed period, the solid Earth tide constituents were estimated better by the gravimetric data compared to positioning data, especially when determining the phases of the considered constituents. Clearly, a larger historical GPS series should be used for determining these constituents more accurately.

The residual graphs obtained from the processing of the gPhone and GPS data show a cyclical behavior, which may be related to non-modeled effects that may cause greater uncertainty when determining the solid Earth tide constituents. The hydrological load cycle is one of the effects that was not modeled and has great influence on the observations; however, due to the difficulty in measuring this effect, it still does not have a satisfactory modeling to be applied to high precision geophysical and geodetic observations.

In the light of what has been exposed in this article, it is recommended to continue the analysis using GPS observations to obtain results that could be more conclusive, especially regarding estimations of the long-term constituents of the determined phase values for the solid Earth tide constituents, and cyclical effects.

ACKNOWLEDGMENTS

REFERENCES

AGNEW D. 2010. Earth Tides. In: HERRING T (Ed.). Treatise on Geophysics, Volume 3: Geodesy, p. 163–195.

ALIHAN NSA, WIJAYA DD, DIN AHM, BRAMANTO B & OMAR AH. 2017. Spatiotemporal Variations of Earth Tidal Displacement over Peninsular Malaysia based on GPS Observations. In: PRADHAN B (Ed.). Global Civil Engineering Conference (GCEC 2017). Singapore. Springer, p. 809–823. doi: 10.1007/978-981-10-8016-6_59.

ARNOSO J, BENAVENT M, BOS MS, MONTESINOS FG & VIEIRA R. 2011. Verifying the body tide at the Canary Islands using tidal gravimetry observations. Journal of Geodynamics, 51(5): 358–365.

BAKER TF & BOS MS. 2003. Validating Earth and ocean tide models using tidal gravity measurements. Geophysical Journal International, 152(2): 468–485.

BENEDITO PMP, ALBARICI FL & TRABANCO JLA. 2017. Determinação preliminar do modelo de maré terrestre para Presidente Prudente/SP. Revista Brasileira de Geomática, 5(3): 420–432.

BLEWITT G, HEFLIN MB, WEBB FH, LINDQWISTER UJ & MALLA RP. 1992. Global coordinates with centimeter accuracy in the International Terrestrial Reference Frame using GPS. Geophysical Research Letters, 19(9): 853–856.

BOY JP, GEGOUT P & HINDERER J. 2002. Reduction of surface gravity data from global atmospheric pressure loading. Geophysical Journal International, 149(2): 534–545.

CHEN L, CHEN JG & XU QH. 2012. Correlations between solid tides and worldwide earthquakes $M_S \geq 7.0$ since 1900. Natural Hazards and Earth System Sciences, 12(3): 587–590.

COCHRAN ES, VIDALE JE & TANAKA S. 2004. Earth tides can trigger shallow thrust fault earthquakes. Science, 306(5699): 1164–1166.

COSTA SMA, MATOS ACOCD & BLITZKOW D. 2012. Validation of the land water storage from gravity recovery and climate experiment (GRACE) with gauge data in the Amazon basin. Boletim de Ciências Geodésicas, 18(2): 262–281.

DEHANT V. 1987. Tidal parameters for an inelastic Earth. Physics of the Earth and Planetary Interiors, 49(1-2): 97–116.

EKMAN M. 1993. A concise history of the theories of tides, precession-nutation and polar motion (from antiquity to 1950). Surveys in Geophysics, 14(6): 585–617.

ESTEY LH & MEERTENS CM. 1999. TEQC: the multi-purpose toolkit for GPS/GLONASS data. GPS Solutions, 3(1): 42–49.

FARRELL WE. 1972. Deformation of the Earth by surface loads. Reviews of Geophysics, 10(3): 761–797.

HARTMANN T & WENZEL HG. 1995. The HW95 tidal potential catalogue. Geophysical Research Letters, 22(24): 3553–3556.

ITO T, OKUBO M & SAGIYA T. 2009. High resolution mapping of Earth tide response based on GPS data in Japan. Journal of Geodynamics, 48(3-5): 253–259.

JEKELI J. 2012. Geometric reference systems in geodesy. Division of Geodetic Science School of Earth Sciences. Ohio State University, 209 pp.

KANG K, LI H, PENG P, HAO H & JIN W. 2011. Seasonal variations in hydrological influences on gravity measurements using gPhones. TAO: Terrestrial, Atmospheric and Oceanic Sciences, 22(2): 157–168. doi: 10.3319/TAO.2010.08.02.01.

KASAHARA J. 2002. Tides, earthquakes, and volcanoes. Science, 297(5580): 348–349.

KRÁSNÁ H, BÖHM J, BÖHM S & SCHUH H. 2012. Solid Earth Tide Parameters from VLBI Measurements and FCN Analysis. In: BEHREND D & BAVER KD (Eds.). Seventh General Meeting (GM2012) of the International VLBI Service for Geodesy and Astrometry (IVS). Madrid, Spain, 2012, National Aeronautics and Space Administration, p. 405–409.

LACOSTE MG. 2018. gPhone Gravity Meter. gPhone Brochure. Available on: <http://www.microglacoste.com/pdf/Brochure-gPhone.pdf>. Access on: September 10, 2018.

MELCHIOR P. 1983. The tides of the planet Earth. Oxford: Pergamon Press. 2nd ed., 653 pp.

MELCHIOR P. 2008. Gravimetric measuring techniques. Physical Methods, Instruments and Measurements. EOLSS, 2: 259–290.

MIDDLEMISS RP, SAMARELLI A, PAUL DJ, HOUGH J, ROWAN S & HAMMOND GD. 2016. Measurement of the Earth tides with a MEMS gravimeter. Nature, 531(7596): 614–617. doi: 10.1038/nature17397.

MIRANDA SA, ORTIZ C, HERRADA AH & PACINO MC. 2015. Análisis de la marea terrestre gravimétrica en la estación San Juan (Argentina). Boletim de Ciências Geodésicas, 21(4): 721-729. doi: 10.1590/S1982-21702015000400042.

MONICO JFG. 2007. Posicionamento pelo GNSS: descrição, fundamentos e aplicações. São Paulo, Brazil: Editora Unesp. 2nd ed., 476 pp.

PETIT G & LUZUM B. 2010. IERS Conventions. IERS Technical Note n. 36. Frankfurt am Main: Verlag des Bundesamts für Kartographie und Geodäsie. 179 pp.

VAN CAMP M & VAUTERIN P. 2005. Tsoft: graphical and interactive software for the analysis of time series and Earth tides. Computers & Geosciences, 31(5): 631–640.

VARGA P & GRAFAREND E. 2019. Influence of tidal forces on the triggering of seismic events. In: BRAITENBERG C & ROSSI G (Eds.). Geodynamics and Earth Tides Observations from Global to Micro Scale, Springer. p. 55–63.

WARBURTON RJ & GOODKIND JM. 1977. The influence of barometric-pressure variations on gravity. Geophysical Journal International, 48(3): 281–292.

WATSON C, TREGONING P & COLEMAN R. 2006. Impact of solid Earth tide models on GPS coordinate and tropospheric time series. Geophysical Research Letters, 33(8): 1-4. doi: 10.1029/2005GL025538.

YUAN L. 2009. Determination of tidal displacements using the Global Positioning System. Ph.D. thesis. The Hong Kong Polytechnic University. 203 pp.

YUAN L, CHAO BF, DING X & ZHONG P. 2013. The tidal displacement field at Earth's surface determined using global GPS observations. Journal of Geophysical Research: Solid Earth, 118(5): 2618–2632.

ZUMBERGE JF, HEFLIN MB, JEFFERSON DC, WATKINS MM & WEBB FH. 1997. Precise point positioning for the efficient and robust analysis of GPS data from large networks. Journal of Geophysical Research: Solid Earth, 102(B3): 5005–5017.

LOCAL ANISOTROPY ESTIMATION FROM *qP*-WAVE VSP DATA: ANALYSIS OF 3D SURVEY DESIGN

Bruno dos Santos Silva[1] and Ellen de Nazaré Souza Gomes[1,2]

ABSTRACT. In the world, several unconventional hydrocarbon reservoirs have been found. This type of reservoir generally has anisotropic properties. The estimation of the anisotropy of the medium can give useful information about the reservoir, for example, one can obtain the information on the direction of fractures that are related to the preferential flow. This information is important in deciding which direction to drill the well. Measurements of slowness and polarization of *qP*-wave obtained from VSP (vertical seismic profile) experiments allow estimating the anisotropy in the vicinity of a geophone inside the borehole. Using the perturbation theory, a weakly anisotropic medium can be modeled by first-order perturbation around a reference isotropic medium. This approach allows to obtain a linear approximation which expresses the slowness and polarization in terms of WA (weak anisotropy) parameters. These parameters characterize the deviations of the anisotropic medium from a reference isotropic medium. In presented inversion scheme, we use the three components of the polarization, since we consider 3C (three-components) geophones, and only one of the slowness components, the one along the borehole direction, in which the receiver array is located. In this work, the inversion scheme using VSP data of slowness and polarization from direct *qP*-wave for the estimation of the parameters of weak anisotropy is analyzed considering the orientation of the horizontal borehole. Three different configurations for the sources are analyzed. The results are compared with results from vertical borehole. It has been found that only a group of components of the tensor of the WA parameters is well estimated and this group depend on the orientation of the borehole. On the other hand, the phase velocity determined from the WA parameter tensor is always well estimated in a 30° cone around the borehole, regardless of the borehole orientation.

Keywords: local anisotropy, VSP multiazimuthal, linear inversion, survey design.

RESUMO. Muitos reservatórios de hidrocarbonetos não convencionais têm sido encontrados. Esse tipo de reservatório geralmente tem propriedades anisotrópicas. A estimativa da anisotropia do meio pode fornecer informações úteis sobre o reservatório como, por exemplo, a direção das fraturas, as quais estão relacionadas à direção de fluxo preferencial. Logo, esta informação é importante para decidir a direção de perfuração de um poço. Medidas de vagarosidade e polarização de ondas *qP* obtidas em levantamentos de VSP (*vertical seismic profile*) permitem estimar a anisotropia na vizinhança de um geofone dentro do poço. Usando a teoria da perturbação, um meio fracamente anisotrópico pode ser modelado como uma perturbação de primeira ordem em relação a um meio isotrópico de referência. Esta abordagem possibilita a obtenção de uma aproximação linear que expressa a vagarosidade e polarização em termos de parâmetros WA (fraca anisotropia). Esses parâmetros caracterizam o desvio do meio anisotrópico em relação a um meio isotrópico de referência. No esquema de inversão são usadas as três componentes do vetor de polarização, pois considera-se geofones 3C (três componentes), e apenas uma componente do vetor de vagarosidade, a componente ao longo da direção de orientação do poço, no qual estão localizados os receptores. Neste trabalho é analisado um esquema de inversão para a estimativa de parâmetros anisotrópicos, são usados dados de vagarosidade e polarização de ondas *qP* diretas em experimentos de VSP considerando a orientação do poço horizontal. Três diferentes configurações para as fontes são estudadas. Os resultados foram comparados com os resultados obtidos considerando o poço vertical. Verificou-se que apenas um grupo de componentes do tensor dos parâmetros elásticos WA é bem estimado. Este grupo depende da orientação do poço. Por outro lado, a velocidade de fase determinada a partir dos parâmetros WA é sempre bem estimada em um cone de 30° entorno do poço, independentemente de sua orientação.

Palavras-chave: anisotropia local, VSP multiazimutal, inversão linear, desenho de experimento.

---

[1]Universidade Federal do Pará, Programa de Pós-Graduação em Geofísica, Rua Augusto Corrêa, 01, 66075-1100 Belém, PA, Brazil – E-mails: brunossgf@gmail.com, ellensgufpa@gmail.com

[2]Instituto Nacional de Ciência e Tecnologia – Criosfera, Brazil.

INTRODUCTION

The anisotropy of a geological formation can be related to natural or induced factors. Among all the causes, we can highlight: natural fracturing induced by stress imbalance (tectonic effect) or artificial fractures (near to borehole) induced by hydraulic fracturing, compliant sediments (near to subsurface), layering (layers with width much smaller than the dominant wavelenght) and intrinsic (case of shales). The methodology presented here, can be useful to achieve the anisotropy degree introduced by any type of anisotropy. However, we are mainly interested in anisotropy induced by fractures (both natural and induced). Because by knowing the maximum degree of anisotropy, it possible to relate this magnitude with preferential direction of fractures and understand the three permeabilities in the fractured reservoir (Ehlig-Economides et al., 1990).

The understanding of the anisotropic reservoirs have play an important role on the Enhanced Oil Recovery (EOR) for this type of reservoir. For a 3D medium, the vertical seismic profiling (VSP) has been established as a technique for measuring in-situ anisotropy in hydrocarbon reservoir (Grechka et al., 2006; Tsvankin & Grechka, 2011). From determination of anisotropic parameters that can be estimated from VSP data set, it is possible to enhance the resolution of seismic imaging, rock elastic property models and characterizing physical features of fractures or cracks (density, orientation, aspect ratio, etc).

Several techniques for estimation of anisotropy parameters from VSP data are found in the literature. In general terms, they can be categorized into two groups: methods that use only slownesses (Gaiser, 1990; Miller & Spencer, 1994; Jílek et al., 2003) and methods that use polarization and slowness (Parscau, 1991; Horne & Leaney, 2000; Dewangan & Grechka, 2003; Grechka & Mateeva, 2007). The application of each method depends primarily on the structural complexities in the overburden (Asgharzadeh et al., 2013).

Using first-order perturbation theory, Zheng & Pšencík (2002) proposed a linearized model that relates perturbations of slowness and polarization of qP-wave to anisotropy parameters in weakly anisotropic media. This method does not depend of structural complexities in the overburden. Gomes et al. (2004) applied this approach to real VSP data collected in the Java Sea region.

The anisotropy estimation from VSP data are limited somehow by factors such as the survey geometry, noise level, data apertures or the wave types. Some recent studies have been concerned with analyzing and investigating the effect of these factors (Rusmanugroho & McMechan, 2012; Barreto et al., 2013; Macambira et al., 2014; Ruzek & Pšencík, 2016).

The design of VSP survey will define the illumination of the medium, hence, the information content in the data. Barreto et al. (2013), using the method of Zheng & Pšencík (2002), investigated the design of multiazimuth walkaway surveys with vertical borehole and showed that at least five source profiles are required so that all anisotropy parameters related to qP-wave are independent in the inversion scheme. Recently, Ruzek & Pšencík (2016), using a method that estimates the anisotropic parameters from P-wave traveltimes, showed that for this approach the use of sources distributed randomly on the surface improves substantially the parameter estimation.

In this work, we present a formulation for horizontal borehole which is an alternative form for vertical borehole formulation presented in Zheng & Pšencík (2002). In this sense, this work is an extension of Barreto et al. (2013), the WA parameters are estimated from direct qP-wave data obtained in 3D VSP experiment where the receivers are distributed in a horizontal borehole and three distribution of sources on the surface are considered: along five radial profiles, randomly distributed (Ruzek & Pšencík, 2016) and in spiral pattern (Blackburn et al., 2007). For comparison, the results obtained here, for the horizontal borehole, were compared with the results obtained for vertical borehole (Barreto et al., 2013).

As horizontal borehole are commonly drilled in unconventional reservoirs, this work can be useful in studies for this kind of reservoirs such as characterization of fracture and fluid content evaluation. For example: if we consider the anisotropic medium of the TI (Transverse Isotropy) type, through the anisotropy parameters we can determine the axis of symmetry of this medium and thus the direction of induced fracturing. The fracture direction is known to be the preferred direction of flow.

METHODOLOGY

The weak anisotropy medium is modeled by first-order perturbations around an isotropic reference medium. In the following, the Cartesian coordinate system (x, y, z) is used for description of the model. The z-axis is chosen positive downwards and the positive x- and y-axes are chosen so that the coordinate system is right-handed.

Let us consider a weakly anisotropic medium and take an isotropic medium as a reference one. The slowness vector p_i of the qP-wave in a weakly anisotropic medium can be expressed as

$$p_i = p_i^0 + \Delta p_i, \tag{1}$$

or

$$p_i = p_i^0 + \Delta\xi\,\vec{i} + \Delta\zeta\,\vec{j} + \Delta\eta\,\vec{k}$$
$$= (\xi + \Delta\xi)\,\vec{i} + (\zeta + \Delta\zeta)\,\vec{j} + (\eta + \Delta\eta)\,\vec{k}, \quad (2)$$

where p_i^0 is a slowness vector in the reference isotropic medium and Δp_i is its perturbation. $\vec{i}$, $\vec{j}$, $\vec{k}$ are unit vectors along the axes x, y and z, respectively. ξ, ζ and η denote projection of the slowness vector p_i^0 onto $\vec{i}$, $\vec{j}$, $\vec{k}$, respectively. $\Delta\xi$, $\Delta\zeta$ and $\Delta\eta$ denote perturbations of p_i^0. The vector p_i^0 is given by

$$p_i^0 = \alpha^{-1} n_i, \quad (3)$$

and its components has the form

$$\xi = \frac{n_1}{\alpha}, \quad \zeta = \frac{n_2}{\alpha}, \quad \eta = \frac{n_3}{\alpha}, \quad (4)$$

where α is the P-wave velocity and the vector $n_i = (n_1, n_2, n_3)$ represents the wave normal, both in the isotropic reference medium.

The wave normal and polarization vector of the P-wave are identical in an isotropic medium. Thus the polarization vector, g_i, of qP-wave in a weakly anisotropic can be written as:

$$g_i = n_i + \Delta g, \quad (5)$$

where Δg is the deviation from the orientation of the polarization vector in a reference isotropic medium.

Let us introduce in the reference isotropic medium three mutually perpendicular unit vectors $e_i^{(1)}$, $e_i^{(2)}$ and $e_i^{(3)}$ so that the vector $e_i^{(3)}$ is identical with the wave normal of the P-wave n_i. A practical choice of vectors $e_i^{(1)}$ and $e_i^{(2)}$ expressed in terms of components of the vector $e_i^{(3)}$ is as follows (Pšencík & Gajewski, 1998):

$$e^{(1)} = D^{-1}(n_1 n_3, n_2 n_3, n_3^2 - 1),$$
$$e^{(2)} = D^{-1}(-n_2, n_1, 0),$$
$$e^{(3)} = n = (n_1, n_2, n_3), \quad (6)$$

where

$$D = \sqrt{n_1^2 + n_2^2}, \quad n_1^2 + n_2^2 + n_3^2 = 1. \quad (7)$$

Using the vectors $e_i^{(k)}$, Pšencík & Gajewski (1998) defined the weak anisotropy matrix:

$$B_{mn} = a_{ijkl} e_i^{(m)} e_j^{(3)} e_l^{(3)} e_k^{(n)} - c_0^2 \delta_{mn}, \quad (8)$$

where a_{ijkl} denotes the tensor of density-normalized elastic parameters, c_0 stands for the phase velocity of the reference

isotropic medium, specified by the P- and S-wave velocities α and β. For $m = n = 3$, $c_0 = \alpha$; for $m = n = 1$ or 2, $c_0 = \beta$. The elements of the matrix B_{mn} are linear function of weak anisotropy (WA) parameters. The WA parameters represent a generalization of Thomsen's parameters to anisotropic media of arbitrary symmetry and orientation (Pšencík & Gajewski, 1998; Farra & Pšencík, 2003). Propagation of qP-wave in weakly anisotropic medium is specified by 15 WA parameters, which are related to density-normalized elastic parameters in the Voigt notation $A_{\alpha\beta}$ in the following way:

$$
\begin{aligned}
\varepsilon_x &= \frac{A_{11} - \alpha^2}{2\alpha^2}, & \varepsilon_y &= \frac{A_{22} - \alpha^2}{2\alpha^2}, \\
\varepsilon_z &= \frac{A_{33} - \alpha^2}{2\alpha^2}, & \delta_x &= \frac{A_{13} + 2A_{55} - \alpha^2}{\alpha^2}, \\
\delta_y &= \frac{A_{23} + 2A_{44} - \alpha^2}{\alpha^2}, & \delta_z &= \frac{A_{12} + 2A_{66} - \alpha^2}{\alpha^2}, \\
\chi_x &= \frac{A_{14} + 2A_{56}}{\alpha^2}, & \chi_y &= \frac{A_{25} + 2A_{46}}{\alpha^2}, \\
\chi_z &= \frac{A_{36} + 2A_{45}}{\alpha^2}, & \varepsilon_{15} &= \frac{A_{15}}{\alpha^2}, \\
\varepsilon_{16} &= \frac{A_{16}}{\alpha^2}, & \varepsilon_{24} &= \frac{A_{24}}{\alpha^2}, \\
\varepsilon_{26} &= \frac{A_{26}}{\alpha^2}, & \varepsilon_{34} &= \frac{A_{34}}{\alpha^2}, \\
\varepsilon_{35} &= \frac{A_{35}}{\alpha^2}.
\end{aligned}
\quad (9)
$$

The slowness and polarization vectors of a qP-wave propagating in an arbitrary anisotropic medium are linearly related to the WA parameters of this medium through the equations (Zheng & Pšencík, 2002):

$$
\begin{aligned}
B_{K3} = (\alpha^2 - \beta^2)(g_i e_i^{(K)} - \alpha\Delta\xi e_1^{(K)} \\
- \alpha\Delta\zeta e_2^{(K)} - \alpha\Delta\eta e_3^{(K)}), K = 1, 2
\end{aligned}
\quad (10)
$$

$$B_{33} = -2\alpha^4 \xi\Delta\xi - 2\alpha^4 \zeta\Delta\zeta - 2\alpha^4 \eta\Delta\eta. \quad (11)$$

The symbols B_{13}, B_{23} and B_{33} are elements of the weak anisotropy matrix B_{mn}, which depend on 15 qP-wave WA

parameters. These elements are written in the following form (Pšencík & Gajewski, 1998):

$$
\begin{aligned}
B_{13} = \alpha^2 D^{-1} \Big\{ & 2\varepsilon_z n_3^5 + n_3^4 (\varepsilon_{34} n_2 + \varepsilon_{35} n_1) \\
& + n_3^3 (\delta_x n_1^2 + \delta_y n_2^2 + 2\chi_z n_1 n_2 - 2\varepsilon_z) \\
& + n_3^2 \big[(4\chi_x - 3\varepsilon_{34}) n_1^2 n_2 \\
& + (4\chi_y - 3\varepsilon_{35}) n_1 n_2^2 + (4\varepsilon_{15} - 3\varepsilon_{35}) n_1^3 \\
& + (4\varepsilon_{24} - 3\varepsilon_{34}) n_2^3 \big] + n_3 \big[(2\delta_z - \delta_x - \delta_y) n_1^2 n_2^2 \\
& + 2(2\varepsilon_{16} - \chi_z) n_1^3 n_2 \\
& + (2\varepsilon_{26} - \chi_z) n_1 n_2^3 + (2\varepsilon_x - \delta_x) n_1^4 + (2\varepsilon_y - \delta_y) n_2^4 \big] \\
& - \chi_x n_1^2 n_2 - \chi_y n_1 n_2^2 - \varepsilon_{15} n_1^3 - \varepsilon_{24} n_2^3 \Big\},
\end{aligned}
$$
(12)

$$
\begin{aligned}
B_{23} = \alpha^2 D^{-1} \Big\{ & n_3^3 (\varepsilon_{34} n_1 - \varepsilon_{35} n_2) \\
& + n_3^2 \big[(\delta_x + \delta_y) n_1 n_2 + \chi_z n_1^2 - \chi_z n_2^2 \big] \\
& + n_3^2 \big[(2\chi_y - 3\varepsilon_{15}) n_1^2 n_2 - (2\chi_x - 3\varepsilon_{24}) n_1 n_2^2 \\
& + \chi_x n_1^3 - \chi_y n_2^3 \big] + (\delta_z - 2\varepsilon_x) n_1^3 n_2 \\
& + (2\varepsilon_y - 2\delta_z) n_1 n_2^3 \\
& + 3(\varepsilon_{26} - \varepsilon_{16}) n_1^2 n_2^2 + \varepsilon_{16} n_1^4 - \varepsilon_{26} n_2^4 \Big\},
\end{aligned}
$$
(13)

$$
\begin{aligned}
B_{33} = 2\alpha^2 \Big\{ & \varepsilon_z n_3^4 + 2 n_3^3 (\varepsilon_{34} n_2 + \varepsilon_{35} n_1) \\
& + n_3^2 (\delta_x n_1^2 + \delta_y n_2^2 + 2\chi_z n_1 n_2) \\
& + 2 n_3 (\chi_x n_1^2 n_2 + \chi_y n_1 n_2^2 + \varepsilon_{15} n_1^3 + \varepsilon_{24} n_2^3) + \varepsilon_x n_1^4 \\
& + \delta_z n_1^2 n_2^2 + \varepsilon_y n_2^4 \\
& + 2\varepsilon_{16} n_1^3 n_2 + 2\varepsilon_{26} n_1 n_2^3 \Big\}.
\end{aligned}
$$
(14)

Eqs. (10) and (11) state a linear relation between the WA parameters of the medium and the polarization and slowness vector. Thus this set of equations can be used for inversion of three-component (3C) data recorded in a receiver inside the borehole.

Let us consider a VSP experiment with receivers in a horizontal borehole along x-axis direction. In this case we have available only the x-component of the slowness vector, which is represented by $p_1 = \xi + \Delta\xi$. If none of the perturbations $\Delta\eta$ and $\Delta\zeta$ is known we can obtain the equation for inversion by eliminating these perturbations from Eqs. (10) and (11). Eliminating firstly $\Delta\eta$ we obtain the set of equations:

$$
\begin{aligned}
& \eta \, (\alpha^2 - \beta^2)^{-1} B_{K3} - \frac{1}{2}\alpha^{-3} B_{33} e_3^{(K)} = \\
& \eta \, g_i e_i^{(K)} - \alpha\Delta\xi (\eta \, e_1^{(K)} - \xi \, e_3^{(K)}) - \alpha\Delta\zeta X^{(K)}, \\
& \qquad\qquad K = 1, 2,
\end{aligned}
$$
(15)

where

$$
X^{(K)} = \eta e_2^{(K)} - \zeta e_3^{(K)},
$$
(16)

then we eliminate $\Delta\zeta$ from Eq. (15) and rearrange it in such way that we find the following form:

$$
\begin{aligned}
& (\alpha^2 - \beta^2)^{-1} (B_{13} e_1^{(1)} + B_{23} e_1^{(2)}) + \frac{1}{2}\alpha^{-1} B_{33}\xi = \\
& g_i (e_i^{(1)} e_1^{(1)} + e_i^{(2)} e_1^{(2)}) - \alpha\Delta\xi.
\end{aligned}
$$
(17)

This proposed equation corresponds an alternative version of the approach of Zheng & Pšencík (2002), but here we assume that the borehole is horizontal.

Determination of the reference medium parameters

Inversion Eq. (17) depend on isotropic reference parameters. The P-wave velocity, α, of reference medium can be obtained from least-squares inversion of the following expression (Barreto et al., 2013):

$$
p_i = \alpha^{-1} g_i.
$$
(18)

Where p_i and g_i corresponds to slowness component observed (z-component for vertical borehole and x-component for horizontal borehole) and polarization vector, respectively. The S-wave velocity, β, is determined by assuming that the reference medium is a Poisson solid, defined as:

$$
\beta = \frac{\alpha}{\sqrt{3}}.
$$
(19)

The wave normal vector n_i is considered parallel to the polarization vector observed, so $n \parallel g$. This approximation is valid for weakly anisotropic medium.

Inversion scheme

WA parameters of the medium in the vicinity of borehole receivers can be estimated by inverting the appropriate equation for borehole orientation. For inversion procedure the suitable equation can be represented in matrix form:

$$
\mathbf{G}\,\mathbf{m} = \mathbf{d}.
$$
(20)

The symbol $\mathbf{d}$ represents a vector which is related to the observations, this vector is given by right side of used equation for each source-receiver pair and has dimension equal to the number of observations (N_{obs}). Symbol $\mathbf{m}$ denotes the vector of model parameters, hence it consists of 15 WA parameters and has the form:

$$
\mathbf{m} = [\varepsilon_x, \varepsilon_y, \varepsilon_z, \delta_x, \delta_y, \delta_z, \chi_x, \chi_y, \chi_z, \varepsilon_{15}, \varepsilon_{16}, \varepsilon_{24}, \varepsilon_{26}, \varepsilon_{34}, \varepsilon_{35}]^T. \quad (21)
$$

Finally, **G** represents a linear operator, called sensitivity matrix, which depends on the parameters of reference medium and the design of VSP experiment. The matrix **G** has dimension N_{obs} x 15 and its elements are obtained from left side of used equation.

Eq. (20) is solved by generalized inverse (Aster et al., 2019). The singular value decomposition (SVD) is used to compute the generalized inverse. Therefore, the solution can be written as

$$\mathbf{m}^{\text{est}} = \mathbf{G}^{\dagger}\,\mathbf{d} \qquad (22)$$

or

$$\mathbf{m}^{\text{est}} = \mathbf{V}\,\mathbf{S}^{-1}\,\mathbf{U}^{T}\,\mathbf{d}, \qquad (23)$$

where $\mathbf{m}^{\text{est}}$ is the vector of estimated parameters, $\mathbf{G}^{\dagger}$ is the generalized inverse of **G**. **U** and **V** are orthogonal matrices of eigenvectors that span the data space and model parameters space, respectively. **S** is the diagonal matrix whose diagonal elements are the singular values $\lambda_1, \lambda_2, \ldots, \lambda_{15}$.

EXPERIMENTAL DESIGN

For vertical borehole in multiazimuth walkaway VSP surveys, as shown by Barreto et al. (2013), at least five radial profiles are necessary so that all 15 WA parameters can be independently retrieved. Here we extend the analysis. For horizontal borehole three distribution of sources on the surface are considered: along five radial profiles, randomly distributed and in spiral pattern.

In the numerical experiments conducted in this work, the data are generated using the program package ANRAY (Gajewski & Pšencik, 1990).
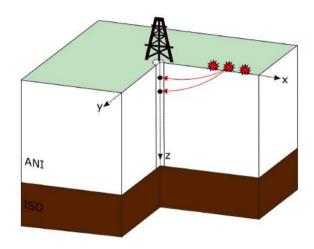
Model and configuration of experiments

The model consists of two layers confined in a box with dimensions 10 km x 10 km x 7 km. The origin of cartesian coordinate system (x, y, z) is situated in the center of the model. The interface between layers is located at a depth of 5 km and has a flat horizontal geometry (Fig. 1).

The first layer is heterogeneous anisotropic with anisotropy degree about 8%. The elastic parameters at the top of the layer corresponds to VTI (transversely isotropy with a vertical symmetry axis) medium with symmetry axis rotated by 80° around the y-axis and then 25° around the z-axis. The elements of non-rotated matrix of the density-normalized elastic moduli in (km/s)^2 of initial VTI medium is: $A_{11} = 15.71$, $A_{13} = 4.46$, $A_{33} = 13.39$, $A_{44} = 4.98$ and $A_{66} = 5.33$ (Thomsen, 1986). The elastic parameters at the bottom corresponds to VTI medium with symmetry axis rotated by 90° around the y-axis. The

elements of non-rotated matrix of the density-normalized elastic moduli in (km/s)^2 of VTI medium is: $A_{11} = 35.35$, $A_{13} = 10.04$, $A_{33} = 30.13$, $A_{44} = 11.21$ and $A_{66} = 11.99$ (Thomsen, 1986).
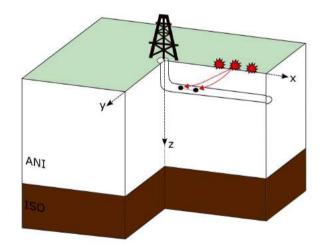
(a)

(b)

Figure 1 – Schematic illustration of model with receiver in vertical and horizontal borehole. The first layer (ANI) is heterogeneous anisotropic and the second one (ISO) is homogeneous isotropic. (a) Vertical borehole with receivers in the z-axis direction. (b) Horizontal borehole with receivers parallel to the x-axis direction.

The distribution of elastic parameters (21 density-normalized elastic parameters) within this layer is given by linear interpolation between the values specified at the top ($z = 0$ km) and at the bottom ($z = 5$ km) surfaces. The second layer is a homogeneous isotropic medium, which is characterized by density-normalized P- and S-wave velocities of 4.77 km/s and 2.76 km/s, respectively.

At the comparison the estimates of the anisotropy obtained in a horizontal borehole will be presented together with the

anisotropy estimates obtained in a vertical borehole. Information on the methodology and estimation of anisotropy for a vertical borehole applied here can be seen in Zheng & Pšencík (2002); Gomes et al. (2004); Barreto et al. (2013) and Macambira et al. (2014).

In the vertical borehole configuration, the receivers array is in the z-axis direction (see Fig. 1a). In the horizontal borehole configuration, the receivers array is located at a depth of 0.5 km and parallel to x-axis direction (see Fig. 1b). The wellhead is situated in the origin of coordinate system.

The Figure 2 shows the three types of source distributions considered in the tests. In each experiment are used 180 sources. Sources close to the wellhead generate slowness vector that reach the well almost vertically, while sources farther from the wellhead generate slowness vector that reached the well almost horizontally. This may compromise the estimation of the anisotropy parameters, since in the inversion scheme the projection of the vector of slowness in the direction of the well is used.

Due to this, the distribution of the sources on the surface was made differently depending on the orientation of the borehole. For the horizontal borehole the sources were distributed in an area whose radius is the twice area where the sources were distributed for the vertical borehole.

In the first geometry (Fig. 2a), the sources are distributed along five radial profiles with angular steps of 72°, each profile contains 36 sources regularly spaced by 0.05 km for vertical borehole configuration or by 0.1 km for horizontal borehole. The second one consists of randomly distribution of sources (see Fig. 2b). In the third distribution type is used a spiral pattern with dual sources array (see Fig. 2c).

The observed data comprises the three components of polarization and x-component of slowness (horizontal borehole) or z-component of slowness (vertical borehole) for each source-receiver pair. We use only direct qP-wave measurements.

Sensitivity study

A sensitivity analysis of WA parameters with respect to acquisition geometry is carried out by using the model resolution matrix. This tool determines whether model parameters can be independently predicted or calculated. The resolution matrix $\mathbf{R}$ can be calculated from singular value decomposition (SVD) of $\mathbf{G}$ in the following way (Menke, 2012):

$$\mathbf{R} = \mathbf{V}_r \mathbf{V}_r^T, \qquad (24)$$

where $\mathbf{V}_r$ is a submatrix of $\mathbf{V}$, that has dimension equal to the number of WA parameters. The matrix $\mathbf{V}_r$ is formed by the r columns of $\mathbf{V}$ that are associated with the acceptable singular values, i.e., those greater than a specified cutoff value. This value is chosen by prescribing an acceptable condition number, defined as the ratio of the largest to smallest singular value. The analysis based on resolution matrix is conducted for receivers at depth of 0.5 km.

Figure 3 shows the singular values computed for the three acquisition geometries in VSP experiment with horizontal borehole. It observed that for the three geometries none of singular values are smaller than 0.01 (cutoff value used). Since all the singular values are considered nonzero, the computation of the model resolution matrices yields identity matrices which means that each of 15 WA parameter can be uniquely determined for the three distributions. This result is similar to that found in the analysis for the vertical borehole.
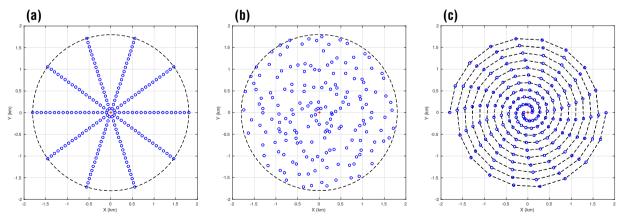

Figure 2 – Plan view of three types of source distribution considered. For each geometry 180 sources are used. The blue markers represent the source positions and the red marker the wellhead position. (a) sources along 5 profiles with angular steps of 72°. (b) sources randomly distributed. (c) sources in spiral pattern.
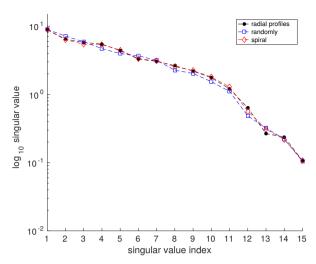
Figure 3 – Singular values for the three acquisition geometries (see Fig. 2) of VSP experiments with horizontal borehole. The black markers are values computed for the sources along five radial profiles. Blue markers are the results for sources randomly distributed. Red markers correspond the result for sources in spiral pattern. The similar result we have for vertical borehole.

The above analysis is a means to assessing which of sought parameters can be uniquely estimated using the acquisition geometries studied. Nonetheless, the resolution of estimates is affected by noise in data, hence it is necessary to investigate how errors in the data project errors in the estimated model. For this purpose, the model covariance matrix is computed in the inversion test.

INVERSION TESTS

The inversion scheme is apply for synthetic data contaminated with random Gaussian noise. The added noise has standard deviations of 1° for polarization vector and 5% for slowness data (z-component for vertical borehole configuration and x-component for horizontal configuration).

Tests are performed for data generated by the three types of source distribution (see Fig. 2) with each borehole configuration. For each data set, the inversion is carried out 500 times for different realizations of noise. The quality of WA parameters recovered from inversion is analyzed by computation of the first-order approximation of the phase velocity (Pšencík & Gajewski, 1998) and comparing maps of phase velocity obtained with exact and inverted parameters. The first-order approximation of phase velocity is given by

$$c\left(n_i, m_j\right) = \sqrt{\alpha^2 + B_{33}}, \qquad (25)$$

where B_{33} is given by Eq. (14) and α stands for the P-wave velocity of the reference isotropic medium. This expression for

phase velocity $c(n_i, m_j)$ depends on the wave normal vector n_i and the model parameters vector m_j, see Eq. (21).

For presentation of inversion results, four types of stereographic projection maps are shown: (a) the phase velocity calculated from the "exact" WA parameters, using Eq. (25); (b) the phase velocity calculated from the expected WA parameters of 500 inversion trials; (c) the relative error expressed as a percent between (b) and (a); and (d) the percentage variation of the phase velocity. The latter map is obtained from the phase velocity calculated from estimates of the 500 inversions.

The stability of the WA parameter estimates is analyzed in two ways. In the first way, the analysis is done indirectly, through the variation of the phase velocities. In the second way, through the numerical computation of the model covariance matrix (Aster et al., 2019) by the following formula:

$$\mathbf{C}_{ij} = \frac{1}{N} \sum_{k=1}^{N} \left(\mathbf{m}_i^{\text{est}(k)} - \overline{\mathbf{m}}_i\right)\left(\mathbf{m}_j^{\text{est}(k)} - \overline{\mathbf{m}}_j\right), \qquad (26)$$

where $\mathbf{C}_{ij}$ denotes the elements of covariance matrix, with $i, j = 1, 2, ..., 15$. N stands for the number of different solutions $\mathbf{m}^{\text{est}}$ obtained from inversion trials. Finally, the symbol $\overline{\mathbf{m}}$ corresponds to the vector of mean (expected) solution, which is obtained from the average of the $N = 500$ solutions $\mathbf{m}^{\text{est}}$.

The diagonal entries of the model covariance matrix are the variances of estimated parameters and the off-diagonal elements describe the correlation between pairs of parameters. Since the noise in the data will cause errors in the model parameter estimates, the covariance values characterize the uncertainty in the recovered parameter.

For data set measured within the horizontal borehole, the inversion is performed using Eq. (17). In the tests it is considered the receiver located at 0.5 km depth, in the same direction of the positive x-axis and 0.4 km away from z-axis.

Before inversion procedure it is necessary to determine the velocities of the isotropic reference medium. The P-wave velocity are obtained from least-squares fitting of polarization and slowness components in the well direction, Eq. (18). The fitting procedure is carried out to data sets generated by the three source distributions. For each data set, the results corresponds to the mean of estimates for 500 realizations of random noise.

The velocities of the reference isotropic medium obtained from data sets generated by the three types of sources distribution are approximately 3.87 km/s for P-wave and 2.23 km/s for S-wave.

Figure 4 shows the stereographic maps of phase velocity computed using exact WA parameters (Fig. 4a), using
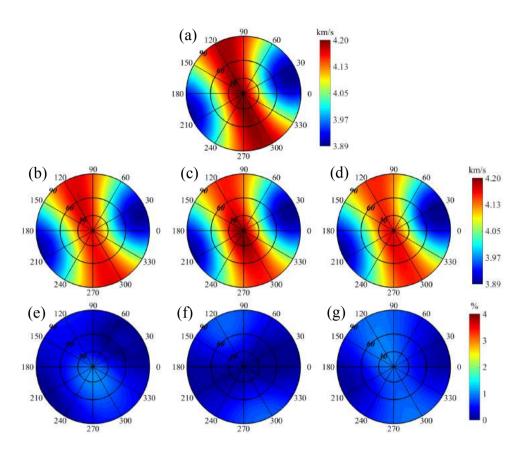
Figure 4 – Stereographic maps to the receiver in the horizontal borehole. (a) Phase velocity computed using exact WA parameters. (b) Phase velocity computed using estimated WA parameter for experiment with sources distributed along 5 profiles. (c) Phase velocity computed using estimated WA parameter for experiment with sources distributed randomly. (d) Phase velocity computed using estimated WA parameter for experiment with sources distributed in spiral pattern. (e) Percentage error between (a) and (b). (f) Percentage error between (a) and (c). (g) Percentage error between (a) and (d).

estimated parameters from data generated by sources along five profiles, randomly distributed and in spiral pattern (Figs. 4b-d, respectively), and the stereographic projection of percentage error between estimated maps and the exact one (Figs. 4e-g). Comparing the results, it is observed that estimated phase velocities and percentage error are similar for the three source distributions. Note that error does not exceed 1.5%.

Figure 5 shows percentage variation maps of phase velocity. The results for sources distributed along five profiles, randomly and in spiral pattern are shown in Figures 5a, 5b and 5c, respectively. According to these figures, it is observed that the phase velocity suffers less variation around the x-axis. As elevation angle increases the velocity variation also increases. Thus, the best estimates are obtained within the region delimited by a 30° cone around the borehole direction. Note that the variation is similar for the three experiments.

The covariance matrices calculated for experiments with the three sources geometries are shown in Figure 6. We note that general patterns in the three matrices are similar. Furthermore, it is observed that there is higher uncertainty in the determination of parameters ε_y, ε_z, δ_x, δ_y, δ_z and moderate to χ_y, ε_{24}, ε_{34}. For the remaining parameters ε_x, χ_y, χ_z, ε_{15}, ε_{16}, ε_{26} and ε_{35} the variances are approximately zero. Therefore these seven parameters are accurately estimated for horizontal borehole configuration.

These results were compared with the results for a vertical borehole. Using $D(\alpha^2 - \beta^2)^{-1}B_{13} - \frac{1}{2}\alpha^{-1}B_{33}\,\eta = Dg_i e_i^{(1)} + \alpha\Delta\eta$, Eq.(1) of Barreto et al. (2013). For receiver at 0.5 km of the vertical borehole, the Figure 7 shows the stereographic maps of phase velocity computed using exact WA parameters (Fig. 7a), using estimated parameters from data generated by sources along five profiles, randomly distributed and in spiral
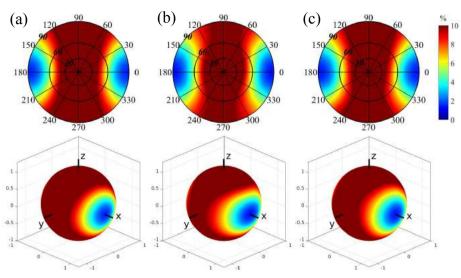
Figure 5 – Percentage variation maps (stereographic projections and its corresponding spherical surfaces) of phase velocity to the receiver in the horizontal borehole. (a) Results for sources along 5 profiles. (b) Results for sources distributed randomly. (c) Results for sources distributed in spiral pattern.
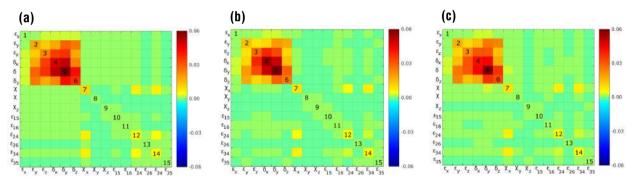

Figure 6 – Model covariance matrices computed for experiments using the three acquisition geometries to the receiver in the horizontal borehole. (a) For sources along 5 profiles. (b) For random sources. (c) For spiral sources pattern.

pattern (Figs. 7b-d, respectively) and the stereographic projection of percentage error (Figs. 7e-g) between estimated maps and the exact one. It can be seen that estimated phase velocities and percentage error are similar for the three source distributions. Note that error does not exceed 2.5%.

Figure 8 shows percentage variation maps of phase velocity. The results for sources distributed along five profiles, randomly and in spiral pattern are shown in Figures 8a-c, respectively. The phase velocity suffers less variation around the vertical axis and best estimates are found within the region delimited by a 30° cone. Comparing the results, it is observed that the variation is similar for the three experiments.

Figure 9 shows the computed covariance matrices for the three acquisition geometries. For the three experiments, we

observe that there is greater uncertainty in the determination of parameters ε_x, ε_y, δ_x, δ_y, δ_z, χ_z, ε_{16}, while for the remaining parameters ε_z, χ_x, χ_y, ε_{15}, ε_{24}, ε_{34} and ε_{35} the variances are approximately zero. Therefore these seven parameters are accurately estimated for vertical borehole configuration.

DISCUSSION

The limited illumination of the medium together with the presence of noise in the data reduce the number of resolvable WA parameters.

For the inversion considering horizontal borehole, according to the Eq. (17), the data that effectively contribute in the inversion scheme, $\alpha \Delta \xi$, are the projection of slowness vector towards the borehole, in x direction. The well
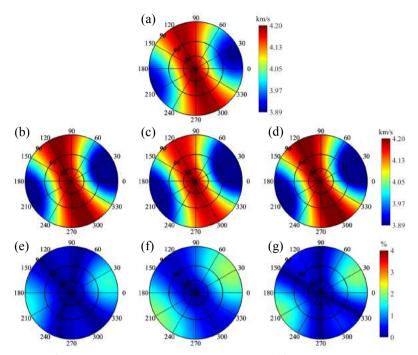
Figure 7 – Stereographic maps to the receiver of the vertical borehole. (a) Phase velocity computed using exact WA parameters. (b) Phase velocity computed using estimated WA parameter for experiment with sources distributed along 5 profiles. (c) Phase velocity computed using estimated WA parameter for experiment with sources distributed randomly. (d) Phase velocity computed using estimated WA parameter for experiment with sources distributed in spiral pattern. (e) Percentage error between (a) and (b). (f) Percentage error between (a) and (c). (g) Percentage error between (a) and (d). The P-wave velocities of the isotropic reference obtained for the three geometries are very close, around 4.22 km/s for P-wave and 2.44 km/s for S-wave.
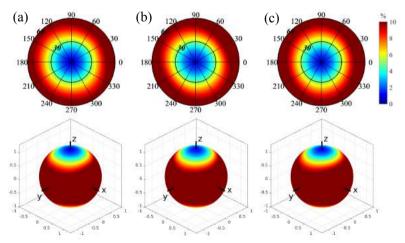

Figure 8 – Percentage variation maps (stereographic projections and its corresponding spherical surfaces) of phase velocity to the receiver of the vertical borehole. (a) Results for sources along 5 profiles. (b) Results for sources distributed randomly. (c) Results for sources distributed in spiral pattern.
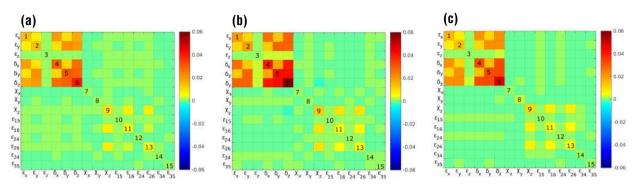
Figure 9 – Model covariance matrices computed for experiments using the three acquisition geometries to the receiver of the vertical borehole. (a) For sources along 5 profiles. (b) For random sources. (c) For spiral sources pattern.

estimated parameters for the horizontal borehole are related to the following elastic parameters of the medium, Eq. (9): $A_{11} = a_{1111}, A_{25} = a_{2213}, A_{46} = a_{2312}, A_{36} = a_{3312}, A_{45} = a_{3213}, A_{15} = a_{1113}, A_{16} = a_{1112}, A_{26} = a_{2212}$ and $A_{35} = a_{3331}$. Considering an infinitesimal volume (Helbig, 1994), these indexes are related to the tension and strain tensors and the directions of application of these tensors. It is found that these parameters present at least one of the indexes in the direction '1' associated with x.

For the inversion considering the vertical borehole, according to Eq.(1) of Barreto et al. (2013), the data that effectively contribute to the inversion scheme, $\Delta\eta$, are to the projection of slowness vector toward the borehole, in the z direction. The well estimated parameters for the vertical borehole are related to the following elastic parameters of the medium, Eq.(9): $A_{33} = a_{3333}, A_{14} = a_{1123}, A_{56} = a_{1312}, A_{25} = a_{2231}, A_{46} = a_{3212}, A_{15} = a_{1113}, A_{24} = a_{2223}, A_{34} = a_{3332}$ and $A_{35} = a_{3331}$. It is found that these parameters present at least one of the indexes in the direction '3' associated with z.

Thus we conclude the well estimated parameters are related to borehole orientation. These conclusions are corroborated, since the parameters: $A_{25} = A_{2231}$, $A_{46} = A_{3212}$, $A_{15} = A_{1113}$ and $A_{35} = A_{3331}$, which have indexes associated with the vertical and horizontal directions are well estimated for both vertical and horizontal boreholes.

The phase velocity is well estimated for angles within about 30° regardless of borehole direction, Figures 4 and 5 for horizontal borehole and Figures 7 and 8 for vertical borehole. The percentage variation of this portion of phase velocity are around 5%, which we considered acceptable for this problem.

In contrast to study of Ruzek & Pšencík (2016), here no advantages were observed in the use of randomly distributed sources on the surface.

CONCLUSION

Most of fractured hydrocarbon reservoir has a background anisotropy either by layering or by fractures with a given directional alignment. In case of horizontal borehole in a medium with fractures aligned vertically, a induced multistage fracturing can be introduced by stress shadows near to the wellbore. For this situation an enhancement on anisotropy can be observed (Murtaza et al., 2013). Our method can support a degree of weak anisotropy, i.e., our method can be efficient for total anisotropy (background + induced) until 10% (in Thomsen's parameters).

In this work, the inversion scheme using VSP data from direct qP-wave for the estimation of the parameters of weak anisotropy WA is analyzed considering the orientation of the horizontal borehole.

The inversion procedure is based on a linearized model that relates weak anisotropy (WA) parameters of the medium around a borehole receiver to measurements of polarization and slowness of qP-wave recorded in the receiver.

We investigated the use of different types of source distribution on the surface for horizontal borehole configuration. Numerical experiments showed that, in general, the use of any the three source distributions investigated will yield similar results. Numerical tests were performed for TI medium and the synthetic data recorded in horizontal borehole. For comparison results in vertical borehole were showed, the results show that the estimation of the anisotropic parameters depends on the orientation of the borehole, however, regardless of the orientation of the borehole, the phase velocity is always well estimated in a cone of 30° around the borehole.

The analysis showed that seven WA parameters can accurately estimated for both borehole configuration. By means of the estimation of these parameters one can determine the orientation of the axis of symmetry of the medium TI and thus

the direction of fracture. The fracture direction is known to be the preferred direction of flow.

Beyond that, we believe that the methodology present in this work can be very useful for characterization of unconventional hydrocarbon reservoir for arbitrary anisotropic symmetry. For further work, we propose apply this methodology in a real anisotropic data set.

ACKNOWLEDGMENTS

REFERENCES

ASGHARZADEH M, BÓNA A, PEVZNER R, UROSEVIC M & GUREVICH B. 2013. Reliability of the slowness and slowness-polarization methods for anisotropy estimation in VTI media from 3C walkaway VSP data. Geophysics., 78(5): WC93–WC102. doi: 10.1190/geo2012-0409.1.

ASTER RC, BORCHERS B & THURBER CH. 2019. Parameter Estimation and Inverse Problems. Volume 90. Elsevier. 3rd ed., 404 pp.

BARRETO A, GOMES EN, MACAMBIRA RN & COSTA JC. 2013. Improvement of local anisotropy estimation from VSP data through experimental design. Journal of Geophysics and Engineering, 10(4): 1-12. doi: 10.1088/1742-2132/10/4/045008.

BLACKBURN J, DANIELS J, DINGWALL S, HAMPDEN-SMITH G, LEANEY S, LE CALVEZ J, NUTT L, MENKITI H, SANCHEZ A & SCHINELLI M. 2007. Borehole seismic surveys: Beyond the vertical profile. Oilfield Review, 19: 20-35.

DEWANGAN P & GRECHKA V. 2003. Inversion of multicomponent, multiazimuth, walkaway VSP data for the stiffness tensor. Geophysics, 68(3): 1022–1031.

EHLIG-ECONOMIDES C, EBBS D & MEEHAN DN. 1990. Factoring Anisotropy into Well Design. Oilfield Review, 2(4): 24-33.

FARRA V & PŠENCÍK I. 2003. Properties of the zeroth-, first-, and higher-order approximations of attributes of elastic waves in weakly anisotropic media. The Journal of the Acoustical Society of America, 114(3): 1366–1378.

GAISER J. 1990. Transversely isotropic phase velocity analysis from slowness estimates. Journal of Geophysical Research: Solid Earth, 95(B7): 11241–11254.

GAJEWSKI D & PŠENCIK I. 1990. Vertical seismic profile synthetics by dynamic ray tracing in laterally varying layered anisotropic structures. Journal of Geophysical Research: Solid Earth, 95(B7): 11301–11315.

GOMES E, ZHENG X, PŠENCÍK I, HORNE S & LEANEY S. 2004. Local Determination of Weak Anisotropy Parameters from Walkaway VSP qP-wave data in the Java Sea Region. Studia Geophysica et Geodaetica, 48(1): 215–231. doi: 10.1023/B:SGEG.0000015593.29477.88.

GRECHKA V, JORGENSEN P & LOPEZ JL. 2006. Anisotropy Estimation from Marine 3D VSP data. In: Offshore Technology Conference, Houston, Texas, U.S.A., OTC 17866, p. 1-4.

GRECHKA V & MATEEVA A. 2007. Inversion of P-wave VSP data for local anisotropy: Theory and case study. Geophysics, 72(4): D69–D79. doi: 10.1190/1.2742970.

HELBIG K. 1994. Foundations of Anisotropy for Exploration Seismics. Handbook of Geophysical Exploration. Volume 22. Oxford: Pergamon. 486 pp.

HORNE S & LEANEY S. 2000. Short note: Polarization and slowness component inversion for TI anisotropy. Geophysical Prospecting, 48(4): 779–788. doi: 10.1046/j.1365-2478.2000.00205.x.

JÍLEK P, HORNBY B & RAY A. 2003. Inversion of 3D VSP P-wave data for local anisotropy: A case study. In: SEG Technical Program Expanded Abstracts 2003. p. 1322–1325. Society of Exploration Geophysicists.

MACAMBIRA RNA, GOMES ENS & BARRETO ACR. 2014. Analysis of a linear scheme for estimation of local anisotropy from P-wave data in multi-azimuth VSP surveys. Brazilian Journal of Geophysics, 32(4): 707–720.

MENKE W. 2012. Geophysical data analysis: discrete inverse theory. MATLAB edition. Volume 45. Academic Press. 330 pp.

MILLER DE & SPENCER C. 1994. An exact inversion for anisotropic moduli from phase slowness data. Journal of Geophysical Research: Solid Earth, 99(B11): 21651–21657.

MURTAZA M, AL NAEIM S & WALEED A. 2013. Design and Evaluation of Hydraulic Fracturing in Tight Gas Reservoirs. OnePetro, p. 1-10. doi: 10.2118/168100-MS.

PARSCAU J. 1991. P- and SV-wave transversely isotropic phase velocities analysis from VSP data. Geophysical Journal International, 107(3): 629–638.

PŠENCÍK I & GAJEWSKI D. 1998. Polarization, phase velocity, and NMO velocity of qP-waves in arbitrary weakly anisotropic media. Geophysics, 63(5): 1754–1766.

RUSMANUGROHO H & McMECHAN G. 2012. Sensitivity of estimated elastic moduli to completeness of wave type, measurement type, and illumination apertures at a receiver in multicomponent VSP data. Geophysics, 77(1): R1–R18. doi: 10.1190/geo2010-0410.1.

RUZEK B & PŠENCÍK I. 2016. P-wave VSP traveltime inversion in weakly and moderately anisotropic media. Seismic Waves in Complex 3-D Structures, 26: 17–59. Available on: <http://sw3d.mff.cuni.cz/papers/r26ip1.htm>. Access on: March 27, 2018.

THOMSEN L. 1986. Weak elastic anisotropy. Geophysics, 51(10): 1954–1966.

TSVANKIN I & GRECHKA V. 2011. Seismology of azimuthally anisotropic media and seismic fracture characterization. Society of Exploration Geophysicists. 511 pp.

ZHENG X & PŠENCÍK I. 2002. Local Determination of Weak Anisotropy Parameters from qP-wave Slowness and Particle Motion Measurements. Pure and Applied Geophysics, 159(7-8): 1881–1905.

ANALYSIS OF SEISMIC ATTRIBUTES TO RECOGNIZE BOTTOM SIMULATING REFLECTORS IN THE FOZ DO AMAZONAS BASIN, NORTHERN BRAZIL

Laisa da Fonseca Aguiar, Antonio Fernando Menezes Freire, Luiz Alberto Santos,
Ana Carolina Ferreira Dominguez, Eloíse Helena Policarpo Neves,
Cleverson Guizan Silva and Marco Antonio Cetale Santos

ABSTRACT. Foz do Amazonas Basin is located at the northern portion of the Brazilian Equatorial Margin, along the coastal zone of Amapá and Pará states. This basin has been subjected to several studies, and the presence of gas hydrates has been demonstrated locally through sampling, and over broader areas using seismic reflection data. Seismic reflection is one method to identify the occurrence of gas hydrates, as they give rise to well-marked reflectors that simulate the seafloor, known as Bottom Simulating Reflectors (BSR). This study aims to investigate BSRs associated with the presence of methane hydrates in the Foz do Amazonas Basin through the application of seismic attributes. It was compared seismic amplitudes from the seafloor and the BSR to validate the inferred seismic feature. Then, Envelope and Second Derivative were chosen for highlighting the BSR in seismic section. The results showed an inversion of polarities in the signal between the seafloor (positive polarity) and the BSR (negative polarity). The integrated use of these approaches allowed validating the level of the BSR in line 0239-0035 and inferring the presence of gas hydrates, revealing to be a useful tool for interpreting the distribution of the gas hydrates in the Foz do Amazonas Basin.

Keywords: gas hydrates, Envelope, Second Derivative of Envelope, Brazilian Equatorial Margin.

RESUMO. A Bacia da Foz do Amazonas é localizada na porção norte da Margem Equatorial Brasileira, ao longo da zona de costa dos estados do Amapá e do Pará. A presença de hidratos de gás é comprovada localmente através de amostragem, e em áreas mais distantes através de dados de sísmica de reflexão. A sísmica de reflexão é eficaz para identificar hidratos de gás, pois refletores que simulam o fundo do mar, *Bottom Simulating Reflectors* (BSR), são utilizados para inferir a presença dos hidratos de metano. Este estudo pretende identificar feições sísmicas associadas aos hidratos de metano na Bacia da Foz do Amazonas através da aplicação de atributos sísmicos. Foram comparadas as amplitudes sísmicas do fundo do mar e do BSR para validar a feição sísmica inferida. Então, os atributos Envelope e Segunda Derivada do Envelope foram escolhidos por destacarem o BSR. Os resultados mostraram uma inversão das polaridades no sinal entre o fundo do mar (positivo) e o BSR (negativo). O uso integrado dessas abordagens valida a localização do BSR na linha 0239-0035 e infere a ocorrência de hidratos de gás, revelando ser uma ferramenta útil para a interpretação da distribuição de hidratos de gás na Bacia da Foz do Amazonas.

Palavras-chave: hidratos de metano, Envelope, Segunda Derivada do Envelope, Margem Equatorial Brasileira.

Universidade Federal Fluminense, Instituto de Geociências, Departamento de Geologia e Geofísica. Av Gen. Milton Tavares de Souza, s/n, 24210-346, Boa Viagem, Niterói, RJ, Brazil,Phone: +55 21 2629-5955 – E-mails: laisafonseca@id.uff.br, fernando_freire@id.uff.br, luizalb1@gmail.com, anadominguez@id.uff.br, eloisehpn@id.uff.br, cguizan@id.uff.br, marcocetale@id.uff.br

INTRODUCTION

The occurrence of natural gas hydrates on continental margins worldwide, including the Foz do Amazonas Basin, is of growing interest due to its energy potential (Kvendolven, 1993; Sloan Jr, 2003; Joshi et al., 2017). Also noteworthy are the environmental aspects related to methane hydrates: their consequences on the planet's climate, as an enhancer of the greenhouse effect, and in the context of instability of the seafloor (Kvendolven, 1993), which according to several authors can trigger mass movements (Flood & Piper, 1997; Maslin & Mikkelsen, 1997; Piper et al., 1997; Maslin et al., 2005). These aspects stimulate new research strategies in this scientific area.

The presence of methane hydrates can be inferred from Bottom Simulating Reflectors (BSRs) on seismic reflection data. A BSR is a seismic reflector parallel to the seafloor that coincides with the base of the Gas Hydrate Stability Zone (GHSZ), characterized by a negative reflectivity, i.e. polarity opposite to the seafloor (Hyndman & Spence, 1992; Kvendolven, 1993). The BSR is inferred to coincide with the phase boundary, and separate solid hydrates above from free gas below (Kvendolven, 1993). Thus, these well-marked reflection works as a seismic signature to identify and map gas hydrates (Joshi et al., 2017).

Seismic attributes are excellent tools for seismic interpretation and are increasingly important for the exploration of hydrocarbons (Taner et al., 1994). The development of seismic attributes is linked to advances in computational and processors. According to Taner et al. (1994) and Taner (2001), attributes were introduced in the early 1970s, where they were initially used only as a visualization tool. This perspective quickly evolved to their use in the qualitative interpretation of geometry and physical subsurface parameters. More recently, with the calibration of seismic data with well data, the use of attributes has sought a more quantitative approach in order to infer seismic characteristics.

The use of seismic attributes allows the extraction of information concerning subsurface geometry and physical parameters to obtain detailed knowledge about the geological context of a prospect (Taner et al., 1979). The choice of an attribute depends on the specific reservoir environments, the mathematical foundation of the attribute and what is this attribute sensitive to (Chen & Sidney, 1997).

There are several studies that uses the application of seismic attributes in order to examine and investigate the presence of gas hydrates in different regions around the world (Coren et al., 2001; Satyavani et al., 2008; Ojha & Sain, 2009). The use of attributes can allow the identification of BSR and its continuity (Coren et al., 2001), and help inferring patterns related to the occurrence of gas hydrates and free gas below the Gas Hydrate Stability Zone (Satyavani et al., 2008).

The Foz do Amazonas Basin has been the object of studies concerning its tectono-sedimentary evolution, gravitational tectonics, hydrates mapping and distribution, and the occurrence of hydrocarbons (oil and gas). The evolution of the basin is related to the formation of the North Atlantic Ocean and its sedimentation extends from the continental margin to the deep-sea fan of the Amazonas River (Soares Jr. et al., 2008).

The Foz do Amazonas Basin is located on the Brazilian Equatorial Margin and includes the submarine deposits of the Amazonas River (Soares Jr. et al., 2008), one of the world's largest deep-sea fans (Damuth & Kumar, 1975). The presence of gas hydrates within the Amazon deep-sea fan has been inferred from BSRs (Sad et al., 1998), and recently confirmed by seafloor sampling of fluid seeps (Ketzer et al., 2018).

This study aims to identify which seismic attributes are more effective to identify the presence of BSRs related to methane hydrates in the Foz do Amazonas Basin. In this work, the software Petrel was used for the interpretation of 2D reflection seismic data obtained from the Exploration and Production Database (BDEP) of the Brazilian National Agency of Petroleum, Natural Gas and Biofuels (ANP – Agência Nacional do Petróleo, Gás Natural e Biocombustíveis).

GEOLOGIC SETTING

The Foz do Amazonas Basin is in the northern portion of the Brazilian Equatorial Margin and occupies a total area of approximately 268,000 km^2, as shown in Figure 1. It includes the continental shelf, the slope and the deep-water region, also known as the Amazon River Cone (Brandão & Feijó, 1994; Figueiredo et al., 2007).

The tectonic evolution of the Foz do Amazonas Basin is associated with the rupture of the supercontinent Gondwana, during the Aptian, that caused the separation of South American and African tectonic plates and the consequent formation of the Atlantic Ocean (Carvalho, 2008).

The structural framework of the Foz do Amazonas Basin can be explained through three tectonic events: the first event occurred in the Late Triassic and was associated with the formation of the Central Atlantic Ocean; the second tectonic event was in the Early Cretaceous and formed an elongated graben. Finally, the third tectonic event began in the Albian and is linked to the final process of separation of the African and South American

Figure 1 – Location map of the seismic survey provided by the Exploration and Production Database (BDEP) for the Foz do Amazonas Basin (Survey 0239_CONE_AMAZONICO_2A_STK_FIN). Seismic line 0239-0035 is highlighted. Source: http://webmaps.anp.gov.br/mapas/Lists/DSPAppPages/MapasBrasil.aspx (access on: May 26, 2018).

plates, resulting in formation of the passive margin and the onset of transform faulting in an ENE-WSW direction that segmented the margin (Soares Jr. et al., 2008).

The Amazon River Cone (or Submarine Fan of the Amazon River) is the morphological feature of greatest expression in the Foz do Amazonas Basin (Araújo et al., 2009), whose formation is associated to a high rate of siliciclastic sedimentation input to the Atlantic Ocean, since the middle Miocene, as a result of the uplift of the Andes Chain (Pasley et al., 2004; Figueiredo et al., 2007).

The Amazon Fan range extends about 700 km from the continental shelf break (Rimington et al., 2000) and reaches bathymetric depths up to 4800 m, with a gradient of 0.4°(Rimington et al., 2000; Da Silva, 2008; Araújo et al., 2009). Cobbold et al. (2004) estimated that the cone has a thickness of approximately 10 km, with an average sedimentation rate of $1\frac{m}{ka}$. (Damuth & Kumar, 1975) delimited the Amazon Cone in three compartments according to changes in its gradient: upper (up to -3000 m of bathymetric level), middle (up to -4200 m) and lower (up to -4800 m). The upper slope concentrates enormous mass-transport deposits (MTDs) that represent the Neogene stratigraphic succession of the fan (Reis et al., 2010, 2016; Silva et al., 2016; Ketzer et al., 2018). Therefore, the focus of this study is concentrated on the Neogene where it hosts the upper slope gas hydrate system.

The Amazon fan is a depocenter in which its loading drives gravitational collapses (Reis et al., 2010, 2016; Ketzer et al., 2018). Several authors point to the existence of MTDs linked to gravitational landslides, and the dissociation of methane hydrates could be a possible trigger for these landslides (Piper et al., 1997; Araújo et al., 2009).

The recent study published by Ketzer et al. (2018) investigates gas seepage from the Gas Hydrate Stability Zone (GHSZ) on the Amazon Fan. They gathered evidence that about 60% of gas vents are located along seafloor faults that register undergoing gravitational collapse of the fan, while 40% are located in water depths of 650–715 m within the upper edge of the GHSZ. This could indicate the role of fluid migration along pathways created by faulting (Ketzer et al., 2018).

RECOGNITION OF GAS HYDRATES

The identification and characterization of methane hydrates can be done through geochemical studies, direct methods (cores and dredges) or indirect (seismic, echosounder, well logs and geoelectric methods) (Freire, 2010; Miller et al., 2015). Other indirect ways of identifying gas hydrates, associated with natural gas seeps or mud volcanoes, are realized through high-resolution imaging of the seafloor using Remoted Operated Vehicle (ROV) (Freire, 2010).

In general, the seismic reflection method is the most indirect method used to infer the presence of methane hydrates, through the identification of BSRs that may be associated with blanking (reduction in reflection amplitude), as well as seafloor mounds or pockmarks (Shipley et al, 1979; Katzman et al., 1994; Gehrmann et al., 2009 apud Miller et al., 2015; Freire et al., 2011).

The presence of gas hydrates is often detected from Bottom Simulating Reflectors, which delineate the maximum depth of the gas hydrate stability zone (Kvendolven, 1993; Lorenson & Kvendolven, 2001). These anomalous reflectors are characterized by reflection polarity opposite to the seafloor (Kvendolven, 1993; Hyndman & Spence, 1992).

SEISMIC ATTRIBUTES DEFINITION

Taner (2001) and Taner et al. (1994) defined seismic attributes as information that can be acquired from seismic data, either by direct/statistical measurements or by the interpreters' experience. By applying these attributes, it is possible to obtain new notions and a more detailed and precise knowledge of the structural, stratigraphic and lithological characteristics of a given seismic prospect (Taner et al., 1979). The choice of attributes depends on the nature of each and the circumstances in which they may be useful, so that a given attribute may be more sensitive to certain reservoir environments, while some are better at revealing underground anomalies or as indicators of hydrocarbons (Chen & Sidney, 1997).

Taner et al. (1979) have developed a mathematical foundation for attribute computing, where the amplitude of the seismic trait is treated as the real part of a complex analytic signal, while the imaginary part is extracted through the Hilbert Transform (Chopra & Marfurt, 2005). Combination of the incoming seismic trait with the Hilbert Transform results in the so-called Instant Attributes, which are computed sample by sample and represent the instantaneous variation of several parameters. They are: Envelope, instantaneous phase, instantaneous frequency, Envelope derivatives, among others (Taner et al., 1979; Taner, 2001; Russel, 2004).

Taner et al. (1979) observed that, from the analysis of the seismic signal as an analytical signal (i.e, analysis of the complex seismic trace), it is possible to separate the two components of the seismic trace, amplitude and phase. The amplitude of the seismic data is considered as the main factor for the determination of physical parameters, such as acoustic impedance, reflection coefficients, velocities and absorption. The phase component is the main factor in determining the shapes of the reflectors and their geometric configurations (Taner, 2001).

Seismic attributes classification

Several authors have contributed to the classification of seismic attributes in different groups. This work will follow the classification proposed by Taner in the official publication of the 2001 Canadian Society of Exploration Geophysics (CSEG), the attributes are classified as Pre-Stack or Post-Stack, based on the characteristic domain of each attribute. They can also be classified according to their computational characteristics. In the following topics, there is a briefly explanation of the main attributes classification used in this study.

Post-Stack attributes

During the stacking process, azimuth and offset information are lost. The input data is stacked or migrated CDPs. Migration in time maintains the relations of time and temporal variables as the frequency has its dimension preserved. For sections migrated in depth, the frequency is replaced by the wave number. This type of attribute is best suited for analyzing large volumes of data in initial studies (Taner, 2001).

Attributes related to geology

In this context, attributes can be divided into physical and geometric categories. Physical attributes are commonly used for lithologic classification and reservoir characterization, relating subsurface parameters to lithological characteristics (Taner, 2001), whereas geometric attributes are used for stratigraphic and structural interpretation.

In this work, after several attempts to select the best attributes to emphasize the BSR of the analyzed seismic section, two physical attributes present best results: the Envelope and the Second Derivative of the Envelope. The next topic describes these attributes and their main characteristics.

Envelope and the Second Derivative of the Envelope

The Envelope attribute is also known as "instantaneous amplitude", "Envelope amplitude" or "reflection strength" (Taner et al., 1979; Chen & Sidney, 1997). The theoretical basis of the instantaneous attributes was developed by (Taner et al., 1979) and it is based on the analysis of the complex seismic trace:

$$C(t) = s(t) + ih(t) \qquad (1)$$

where $s(t)$ corresponds to the real part of the complex seismic trace; $h(t)$ is the Hilbert Transform of the seismic trace, the imaginary part of the trace (also known as quadrature - Russel, 2004). The imaginary component $h(t)$ is obtained by applying the Hilbert Transform in the seismic trace $s(t)$, under the following conditions for $h(t)$:

1. It is determined from $s(t)$ by a linear convolution operation;

2. Reduce to the phasor representation (in complex numbers) if $s(t)$ is a sinusoid.

If these conditions are met it is possible to determine $h(t)$ for any $s(t)$ that can be represented by a Fourier series or integral

(Taner et al., 1979). The use of the complex seismic trace allows computing instantaneous amplitude, instantaneous phase and instantaneous frequency in simple harmonic oscillation logic extensions. Therefore, the complex seismic trace can be rewritten in polar form:

$$C(t) = A(t)e^{i\theta(t)} \tag{2}$$

where $A(t)$ is the envelope of the seismic trace (or amplitude/instantaneous energy) and corresponds to the complex function module $C(t)$:

$$A(t) = \sqrt{s(t)^2 + h(t)^2} \tag{3}$$

The Envelope is phase independent and is sensitive to changes in acoustic impedance, emphasizing changes in amplitude of the original seismic section. This attribute is related to reflectivity because it is proportional to the acoustic impedance contrast. In addition, it can be a good discriminant of numerous geological features, such as bright spots, possible gas accumulations, unconformities, changes in lithology and deposition environments, sequence limits, among others (Taner, 1992, 2001).

The Second Derivative of the Envelope is a seismic attribute that provides a measure of sharpness of the envelope peak. It shows all the peaks of the envelope, thus allowing a good representation of the subsurface, identifying all reflection interfaces, visible within the seismic bandwidth. This attribute also shows sudden changes in lithology and the depositional environment, even when the corresponding Envelope is low (SEG Wiki, accessed October 16, 2017).

METHODS

Seismic data input and quality control

The first step in this work was the loading of seismic data, provided by the National Agency of Petroleum (ANP) - Exploration and Production Database (BDEP), into the software Petrel. Initially, the coordinates of the study region for the creation of the "Foz do Amazonas" project were defined. After the establishment area covered by the seismic survey, 74 seismic lines of 2D reflection were imported.

Due to the large number of seismic lines and the time required to map the horizons (seafloor and BSR), a sorting was carried out to choose the most appropriate seismic profile for the execution of this study. Seismic profiles were previously interpreted by the authors to analyze their quality and to extract preliminary knowledge about the main seismic reflectors. Thus, line 0239-0035 (Fig. 2) was selected because it presents interesting features, possibly related to gas hydrates.

Comparing amplitudes and applying seismic attributes

In this step, two spreadsheets were created to analyze the behavior of the possible BSR in comparison to the seafloor, in two distinct sections, in order to assure the BSR sectors location in the seismic.
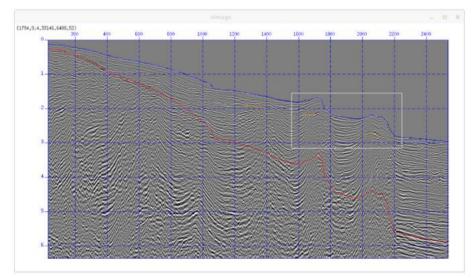

Figure 2 – Seismic line 0239-0035. The highlighted area in white represents the region of interest for this project. The blue line corresponds to the seafloor, the red line represents the seismic multiple and the yellow lines refer to possible BSRs.
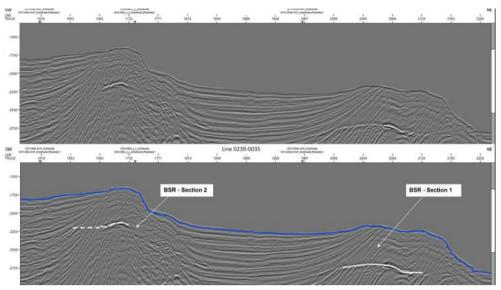
Figure 3 – Seismic line 0239-0035 with no interpretation (top) and with the two sections of BSR (white lines).

Afterwards, several seismic attributes were used to highlight the identified BSR in line 0239-0035 and, consequently, to infer the lower boundary of the gas hydrate stability zone. Two attributes were chosen that best highlighted the BSR: Envelope and Second Derivative of the Envelope.

RESULTS

Seismic interpretation

Through the methodology described above, it was possible to interpret line 0239-0035 and to identify negative amplitude reflections interpreted as BSRs, an indicative of the existence of methane hydrates in the Foz do Amazonas Basin (Fig. 3). When a BSR cross-cuts stratal reflections that are not parallel to the seafloor, it is sharp and easily identified. In sections where the stratification is parallel to the seafloor, BSRs can be harder to identify (Holbrook et al., 2002). The analysis of seismic amplitude and the use of seismic attributes can mitigate these uncertainties in order to infer the presence of gas hydrates. For this project, line 0239-0035 was analyzed in two sections, where possible BSRs are observed to cross-cut strata that are not parallel to the seafloor.

Comparison of seismic amplitudes of the seafloor and the BSR

According to Kvendolven (1993), the seismic reflector that coincides with the lower limit of the gas hydrate stability zone can be defined by reversed polarity, in comparison to the seafloor coefficients. Theoretically, the amplitudes of well-marked BSRs are expected to be negative and large (Dillon et al., 1996).

In order to validate the location of the BSRs in seismic and infer the presence of methane hydrates associated to these features, it is compared the seismic amplitudes for the two sections of line 0239-0035, in which these seismic reflectors are observed (Tables 1 and 2).

The amplitude data are plotted in Figures 4 and 5 and the inversion in polarity between the seafloor (positive) and the BSR (negative) is easily recognized. Even if the reversed polarity is not in terms of absolute values, there is clearly an approximation between the values of these amplitudes (except for a few points), which validates the identification and level of the BSR in both sections 1 and 2. BSR amplitude is extremely sensitive to small gas concentrations located below the hydrate stability zone (Holbrook et al., 2002), and some authors suggest that BSRs appear discontinuous at higher frequencies, forming a series of strong reflections that are parallel to the seafloor but laterally discontinuous (Dillon et al., 1996). This could be an explanation for the small intervals in which the absolute values of seismic amplitudes between the seafloor and the BSR are dissimilar. The concentration of gas hydrates, above the BSR, and of free gas below it, vary and cause the intensity of the reflector to vary locally. Thus, the BSR will be stronger the greater the saturations of gas hydrates and free gas, which increases the impedance contrast.

Table 1 – Seismic amplitudes of the seafloor and the BSR on section 1.

Trace Number	Seafloor	BSR - Section 1	Trace Number	Seafloor	BSR - Section 1
2112	12808.56	-10656.72	2064	6168.75	-4498.05
2110	9941.59	-16342.33	2062	6052.86	-13192.13
2108	9742.86	-7887.07	2060	7234.50	-11795.37
2106	6571.67	-3447.43	2058	3621.08	-4828.11
2104	10053.42	-13246.86	2056	6595.07	-8324.93
2102	12520.13	-10762.92	2054	8689.13	-7888.82
2100	12471.26	-12270.68	2052	1334.79	-1557.25
2098	10451.69	-17781.45	2050	10097.24	-12217.66
2096	3333.18	-3199.85	2048	7923.26	-7923.26
2094	11625.40	-17576.50	2046	9508.13	-7253.63
2092	10089.71	-16173.21	2044	7316.68	-11405.42
2090	9656.11	-6025.84	2042	6146.11	-10243.50
2088	10560.94	-11979.57	2040	7663.14	-6583.83
2086	11739.30	-20389.32	2038	7079.82	-14687.98
2084	10566.54	-18044.40	2036	8147.05	-6449.75
2082	11348.44	-15924.43	2034	6858.00	-464.95
2080	10307.38	-18287.28	2032	5955.43	-5382.79
2078	9845.25	-17753.72	2030	4629.75	-3105.90
2076	9757.63	-19876.65	2028	4401.63	-2475.91
2074	6618.80	-16901.58	2026	4463.05	-1580.67
2072	4437.52	-3138.74	2024	5638.22	-7301.96
2070	6857.89	-12423.72	2022	8304.45	-7932.61
2068	4503.11	-4102.83	2020	8357.59	-10103.95
2066	3450.30	-6325.55			

Figure 4 – Seismic amplitudes of line 0239-0035 on the seafloor and the BSR - section 1.

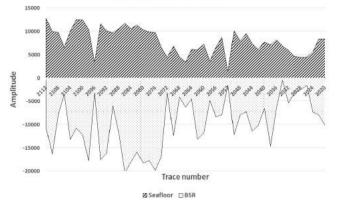**Table 2** – Seismic amplitudes of the seafloor and the BSR on section 2.

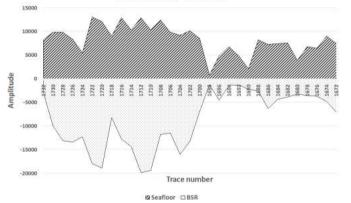| Trace Number	Seafloor	BSR - Section 2	Trace Number	Seafloor	BSR - Section 2
1732	8220.20	-2901.25	1700	8542.56	-6930.76
1730	9832.01	-9993.19	1698	805.90	-1289.44
1728	9832.01	-13055.61	1696	4835.41	-4513.05
1726	8381.38	-13377.98	1694	6769.58	-1450.62
1724	5480.13	-12249.71	1692	4835.41	-1289.44
1722	13055.61	-17891.03	1690	2095.35	-2256.53
1720	12088.53	-18858.11	1688	8220.20	-2578.89
1718	9026.10	-8220.20	1686	7253.12	-6286.04
1716	12894.43	-12733.25	1684	7414.30	-4351.87
1714	10315.55	-14345.06	1682	7575.48	-3868.33
1712	12894.43	-19825.19	1680	3868.33	-3223.61
1710	10315.55	-19341.65	1678	6769.58	-3545.97
1708	12410.89	-11766.17	1676	6447.22	-3707.15
1706	9832.01	-11443.81	1674	9026.10	-4835.41
1704	9187.28	-15956.86	1672	7414.30	-7091.94
1702	10154.37	-13216.79			

Figure 5 – Seismic amplitudes of line 0239-0035 on the seafloor and the BSR – section 2.

Application of seismic attributes

The first seismic attribute applied to the line was the Envelope (or instantaneous amplitude). As this attribute is directly related to the acoustic impedance contrast, its application is significant for the characterization of methane hydrates. Figure 6 shows line 0239-0035 with the Envelope attribute applied. The use of the Envelope attribute enhances the visualization and identification of BSR, especially in the interval between the numbers of traces 2112-2022 for section 1 and 1732-1676 for section 2, since this attribute works as a good discriminator for lithological and stratigraphic changes in reservoirs and accumulations of gas and fluids (Taner, 1992; Chen & Sidney, 1997), therefore it highlights the presence of free gas trapped beneath the BSR.

The second seismic attribute used to infer the presence of methane hydrates was the Second Derivative of the Envelope.
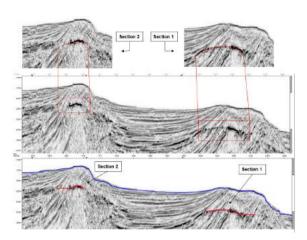
Figure 6 – Seismic line 0239-0035 with Envelope attribute applied. The two sections of BSR are highlighted in red.
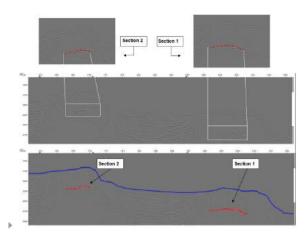

Figure 7 – Seismic line 0239-0035 with the Second Derivative of Envelope attribute applied. The two sections of BSR are highlighted in red.

Figure 7 illustrates line 0239-0035 with the Second Derivative of the Envelope applied and possible portions of the BSR not interpreted and interpreted, respectively. Like the Envelope, the use of the Second Derivative of Envelope enhances the visualization of the BSR of both passages in the seismic section. According to Taner (1992), this attribute provides a good subsurface representation and highlights less smooth lithology changes.

DISCUSSION

As Satyavani et al. (2008) pointed out, mapping a BSR in a seismic section is an effective approach in order to find the occurrence of methane hydrates. There are some studies around the world in which the BSRs are not identified, however gas hydrates have been confirmed by drilling (Satyavani et al., 2008). This suggests the importance of looking for other indirect methods to ascertain the presence of gas hydrates and free gas.

Therefore, using seismic attributes as a tool for seismic interpretation of methane hydrates is valid and legitimate. Each seismic attribute has its own advantages, disadvantages and limitations. It is worth noting the importance of applying more than one attribute for reducing uncertainties and avoiding biased interpretations. For instance, Coren et al. (2001) suggested a multi-attribute analysis with well logs correlation that supported delineate some of the characterizing physical properties of the BSR. As Satyavani et al. (2008) indicate, the application of AVO (amplitude versus offset) can also provide information about the presence of free gas beneath the BSR. Besides, in other studies, it was observed that seismic attribute analysis allowed instantaneous amplitude (or Envelope) and

instantaneous frequency sections to validate the level of the BSR and hence infer the presence of gas hydrate layer and free gas (Satyavani et al., 2008; Joshi et al., 2017), which corroborates with what has been proposed in this study.

CONCLUSIONS

The integration of geophysical methods is valuable for a more accurate characterization of the subsurface. In this study, two approaches were proposed: a comparison of seismic amplitudes and the application of seismic attributes, which together addressed the identification of BSRs. These approaches reveal to be a useful tool for interpreting the distribution of the gas hydrates in the Foz do Amazonas Basin.

The results showed that there is an inversion of polarities in the signal between the seafloor (positive polarity) and the BSR (negative polarity), although this inversion is not always in absolute values. In addition, the attributes chosen for this study - Envelope and Second Envelope Derivative – were able to enhance the visualization of BSR. The integrated use of these methods allowed validating the identification of the BSR in line 0239-0035 and inferring the presence of gas hydrates.

REFERENCES

ARAÚJO EFS, SILVA CG, REIS ATD, PEROVANO R, GORINI C, VENDEVILLE BC & ALBUQUERQUE NCD. 2009. Movimentos de massa multiescala na bacia da Foz do Amazonas-Margem Equatorial Brasileira. Brazilian Journal of Geophysics, 27(3): 485–508.

BRANDÃO JAS & FEIJÓ FJ. 1994. Bacia da Foz do Amazonas. Boletim de Geociências da Petrobras, 8(1): 91–99.

CARVALHO GCRD. 2008. Interpretação sísmica e modelagem física do cone do Amazonas, Bacia da Foz do Amazonas, margem equatorial brasileira. Master's dissertation. Departamento de Geologia, Escola de Minas, Universidade Federal de Ouro Preto, MG, Brazil. 119 pp.

CHEN Q & SIDNEY S. 1997. Seismic attribute technology for reservoir forecasting and monitoring. The Leading Edge, 16(5): 445–448.

CHOPRA S & MARFURT KJ. 2005. Seismic attributes - A historical perspective. Geophysics, 70(5): 3SO–28SO.

COBBOLD PR, MOURGUES R & BOYD K. 2004. Mechanism of thin-skinned detachment in the Amazon Fan: assessing the importance of fluid overpressure and hydrocarbon generation. Marine and Petroleum Geology, 21(8): 1013–1025.

COREN F, VOLPI V & TINIVELLA U. 2001. Gas hydrate physical properties imaging by multi-attribute analysis – Blake Ridge BSR case history. Marine Geology, 178(1-4): 197–210.

DA SILVA RJP. 2008. Colapso gravitacional e estruturação da seção marinha da bacia da Foz do Amazonas no contexto de múltiplos níveis de destacamento. Master's dissertation. Departamento de Geologia, Universidade Federal Fluminense, Niterói, RJ, Brazil. 101 pp.

DAMUTH JE & KUMAR N. 1975. Amazon cone: morphology, sediments, age, and growth pattern. Geological Society of America Bulletin, 86(6): 863–878.

DILLON WP, HUTCHINSON DR & DRURY RM. 1996. Seismic reflection profiles on the Blake Ridge near Sites 994, 995, and 997. In: Proceedings of the Ocean Drilling Program. Initial Reports, 164: 47-56.

FIGUEIREDO JJP, ZALÁN PV & SOARES EF. 2007. Bacia da Foz do Amazonas. Boletim de Geociências da Petrobras, 15(2): 299–309.

FLOOD RD & PIPER DJ. 1997. Amazon Fan sedimentation: the relationship to Equatorial climate change, continental denudation, and sea-level fluctuations. In: FLOOD RD, PIPER DJW, KLAUS A & PETERSON LC (Eds.). Proceedings of the Ocean Drilling Program. Scientific Results, 155: 653–675.

FREIRE AFM. 2010. An integrated study on the gas hydrate area of Joetsu Basin, eastern margin of Japan Sea, using geophysical, geological and geochemical data. Ph.D. thesis. Graduate School of Frontier Sciences. The University of Tokyo, Japan. 247 pp.

FREIRE AFM, MATSUMOTO R & SANTOS LA. 2011. Structural-stratigraphic control on the Umitaka Spur gas hydrates of Joetsu Basin in the eastern margin of Japan Sea. Marine and Petroleum Geology, 28: 1967–1978.

GEHRMANN R, MÜLLER C, SCHIKOWSKY P, HENKE T, SCHNABEL M & BÖNNEMANN C. 2009. Model-based Identification of the Base of the Gas Hydrate Stability Zone in Multichannel Reflection Seismic Data, Offshore Costa Rica. International Journal of Geophysics, 2009: ID 812713, 12 pp.

HOLBROOK WS, GORMAN AR, HOMBACH M, HACKWITH KL, NEALON J, LIZARRALDE D & PECHER IA. 2002. Seismic detection of marine methane hydrate. The Leading Edge, 21(7): 686–689.

HYNDMAN RD & SPENCE GD. 1992. A seismic study of methane hydrate marine bottom simulating reflectors. Journal of Geophysical Research: Solid Earth, 97(B5): 6683–6698.

JOSHI AK, PANDEY L & SAIN K. 2017. Identification of BSR and estimation of gas hydrate from well-log data at NGHP-01-04a and 11A in the Krishna-Godavari Basin, Eastern Indian Margin. In: SEG Technical Program Expanded Abstracts 2017. Society of Exploration Geophysicists. p. 3483–3487.

KATZMAN R, HOLBROOK WS & PAULL CK. 1994. Combined vertical-incidence and wide-angle seismic study of a gas hydrate zone, Blake Ridge. Journal of Geophysical Research: Solid Earth, 99(B9): 17975–17995.

KETZER JM, AUGUSTIN A, RODRIGUES LF, OLIVEIRA R, PRAEG D, PIVEL MAG, DOS REIS AT, SILVA C & LEONEL B. 2018. Gas seeps and gas hydrates in the Amazon deep-sea fan. Geo-Marine Letters, 38(5): 429–438.

KVENDOLVEN KA. 1993. Gas hydrates-geological perspective and global change. Reviews of Geophysics, 31(2): 173–187.

LORENSON TD & KVENDOLVEN KA. 2001. A worldwide Assessment of Coincidental gas hydrate and Petroleum Gas Occurrences. In: AAPG Annual Convention. Program with Abstracts, Tulsa, AAPG, v. 10, A120.

MASLIN M & MIKKELSEN N. 1997. Amazon Fan mass-transport deposits and underlying interglacial deposits: age estimates and Fan dynamics. In: FLOOD RD, PIPER DJW, KLAUS A & PETERSON LC (Eds.). Proceedings of the Ocean Drilling Program. Scientific Results, 155: 353–365.

MASLIN M, VILELA C, MIKKELSEN N & GROOTES P. 2005. Causes of catastrophic sediment failures of the Amazon Fan. Quaternary Science Reviews, 20: 2180–2193.

MILLER DJ, KETZER JM, VIANA AR, KOWSMANN RO, FREIRE AFM, OREIRO SG, AUGUSTIN AH, LOUREGA RV, RODRIGUES LF, HEEMAN R & PREISSLER AG. 2015. Natural gas hydrates in the Rio Grande Cone (Brazil): A new province in the western South Atlantic. Marine and Petroleum Geology, 67: 187–196.

OJHA M & SAIN K. 2009. Seismic attributes for identifying gas-hydrates and free-gas zones: application to the Makran accretionary prism. Episodes, 32(4): 264–270.

PASLEY MA, SHEPHERD DB, POCKNALL DT, BOYD KP, ANDRADE V & FIGUEIREDO JP. 2004. Sequence stratigraphy and basin evolution of the Foz do Amazonas Basin, Brazil. In: AAPG International Conference & Exhibition. Cancun, Mexico: American Association of Petroleum Geologists, 10082.

PIPER DJW, PIRMEZ C, MANLEY PL, LONG D, FLOOD RD, NORMARK WR & SHOWERS W. 1997. Mass-transport deposits of the Amazon Fan. In: FLOOD RD, PIPER DJW, KLAUS A & PETERSON LC (Eds.). Proceedings of the Ocean Drilling Program. Scientific Results, 155: 109–146.

REIS AT, ARAÚJO E, SILVA CG, CRUZ AM, GORINI C, DROZ L, MIGEON S, PEROVANO R, KING I & BACHE F. 2016. Effects of a regional décollement level for gravity tectonics on late Neogene to recent large-scale slope instabilities in the Foz do Amazonas Basin, Brazil. Marine and Petroleum Geology, 75: 29–52.

REIS AT, PEROVANO R, SILVA CG, VENDEVILLE BC, ARAÚJO E, GORINI C & OLIVEIRA V. 2010. Two-scale gravitational collapse in the Amazon Fan: a coupled system of gravity tectonics and mass-transport processes. Journal of the Geological Society, 167(3): 593–604.

RIMINGTON N, CRAMP A & MORTON A. 2000. Amazon Fan sands: implications for provenance. Marine and Petroleum Geology, 17(2): 267–284.

RUSSEL BH. 2004. The application of multivariate statistics and neural networks to the prediction of reservoir parameters using seismic attributes. Ph.D. thesis. University of Calgary, Canada. 392 pp.

SAD ARE, SILVEIRA DP, MACHADO MAP, SILVA SRP & MACIEL RR (Eds.). 1998. Marine gas hydrates evidence along the Brazilian Coast. In: AAPG International Conference and Exhibition. Rio de Janeiro, Brazil: American Association of Petroleum Geologists.

SATYAVANI N, SAIN K, LALL M & KUMAR BJP. 2008. Seismic attribute study for gas hydrates in the Andaman Offshore India. Marine Geophysical Researches, 29(3): 167–175.

SHIPLEY TH, HOUSTON MH, BUFFLER RT, SHAUB FJ, McMILLEN KJ, LADD JW & WORZEL JL. 1979. Seismic reflection evidence for widespread occurrence of possible gas-hydrate horizons on continental slopes and rises. American Association of Petroleum Geologists Bulletin, 63: 2204–2213.

SILVA CC, DOS REIS AT, PEROVANO RJ, GORINI MA, DOS SANTOS MV, JECK IK, TAVARES AAA & GORINI C. 2016. Multiple megaslide complexes and their significance for the Miocene stratigraphic evolution of the offshore Amazon Basin. In: LAMARCHE G, MOUNTJOY J, BULL S, HUBBLE T, KRASTEL S, LANE E, MICALLEF A, MOSCARDELLI L, MUELLER C, PECHER I & WOELZ S (Eds.). Submarine Mass Movements and their Consequences. Springer, 41: 49–60.

SLOAN Jr ED. 2003. Fundamental principles and applications of natural gas hydrates. Nature, 426(6964): 353.

SOARES Jr AV, COSTA JBS & HASUI Y. 2008. Evolução da Margem Atlântica Equatorial do Brasil: Três Fases Distensivas. Geociências (São Paulo), 27: 427–437.

TANER MT. 1992. Attributes Revisited - Rock Solid Images. Houston, Texas. RSI. (Revised Sep. 2000), p. 3-27.

TANER MT. 2001. Seismic Attributes. CSEG Recorder, 26(7): 49–56.

TANER MT, KOEHLER F & SHERIFF RE. 1979. Complex seismic trace analysis. Geophysics, 44(6): 1041–1063.

TANER MT, O'DOHERTY R, SCHUELKE JS & BAYSAL E (Eds.). 1994. Seismic attributes revisited. In: 64th SEG Annual Meeting. Expanded Abstracts. Los Angeles, US, Society of Exploration Geophysicists.

ADDITIONAL REFERENCES

BDEP WebMaps – Banco de Dados de Exploração e Produção, ANP. Available on: <http://webmaps.anp.gov.br/mapas/Lists/DSPAppPages/MapasBrasil.aspx.>. Access on: May 26, 2018.

SEG Wiki – Dictionary: Second Time Derivative of the trace Envelope. Available on: <http://wiki.seg.org/wiki/Dictionary:Second_time_derivative_of_the_trace_Envelope>. Access on: October 16, 2017.

GEOLOGICAL CHARACTERIZATION OF EVAPORITIC SECTIONS AND ITS IMPACTS ON SEISMIC IMAGES: SANTOS BASIN, OFFSHORE BRAZIL

Alexandre Rodrigo Maul[1,2], Marco Antonio Cetale Santos[2], Cleverson Guizan Silva[2], Josué Sá da Fonseca[1], María de Los Ángeles González Farias[3], Leonardo Márcio Teixeira da Silva[1,2], Thiago Martins Yamamoto[1,2], Filipe Augusto de Souto Borges[1] and Rodrigo Leandro Bastos Pontes[1,2]

ABSTRACT. The pre-salt reservoirs in the Santos Basin are known for being overlaid by thick evaporitic layers, which degrade the quality of seismic imaging and, hence, impacts reservoir studies. Better seismic characterization of this section can then improve decision making in E&P (Exploration and Production) projects. Seismic inversion – particularly with adequate low-frequency initial models – is currently the best approach to build good velocity models, leading to increased seismic resolution, more reliable amplitude response, and to attributes that can be quantitatively connected to well data. We discuss here a few considerations about inverting seismic data for the evaporitic section, and address procedures to improve reservoir characterization when using this methodology. The results show that we can obtain more realistic seismic images, better predicting both the reservoir positioning and its amplitude.

Keywords: evaporitic section, seismic imaging, seismic inversion, reservoir characterization, seismic resolution.

RESUMO. Os reservatórios do pré-sal da Bacia de Santos são conhecidos por estarem abaixo de uma espessa camada de evaporitos, que degradam a qualidade das imagens sísmicas e impactam os estudos de reservatórios. Melhores caracterizações desta seção podem, então, melhorar o processo de tomada de decisão em projetos de E&P (Exploração e Produção). Inversão sísmica –- particularmente com modelos de baixa frequência inicialmente adequados -– é atualmente a melhor abordagem para se construir modelos de velocidades, auxiliando no aumento de resolução sísmica, obtendo-se respostas de amplitude mais coerentes, e tendo seus atributos quantitativamente conectados com as informações de dados de poços. Aqui discutiremos algumas considerações sobre inversões sísmicas para seção evaporítica, e indicaremos procedimentos para melhorar a caracterização de reservatórios quando utilizada esta metodologia. Os resultados mostram que podemos obter imagens sísmicas mais realistas, com melhores predições tanto em termos de posicionamento quanto de amplitude.

Palavras-chave: seção evaporítica, imagem sísmica, inversão sísmica, caracterização de reservatórios, resolução sísmica.

---

[1]Petrobras – Reservoir Geophysics, Avenida República do Chile, 330, 9º andar, 20031-170 Rio de Janeiro, RJ, Brazil – E-mails: alexandre.maul@petrobras.com.br, josuefonseca@petrobras.com.br, lmtsilva@petrobras.com.br, thiagomyamamoto@petrobras.com.br, filipeborges@petrobras.com.br, rpontes@petrobras.com.br

[2]Universidade Federal Fluminense – UFF, Geology and Geophysics, Av. Milton Tavares de Souza, s/nº - Gragoatá, 24210-340 Niterói, RJ, Brazil – E-mails: marcocetale@id.uff.br, cguizan@id.uff.br

[2]Emerson Automation Solutions, Av. Rio Branco, 138, sala 1702, 20040-002 Rio de Janeiro, RJ, Brazil – E-mail: maria.g.gonzalez@emerson.com

INTRODUCTION

The proper study of thick evaporitic deposits is quite challenging – they are usually buried, which imposes difficulties to access the intrasalt facies (Stefano et al., 2010). Most of the current knowledge about ancient saline giants[1]/salt giants[2] are built upon outcrop data, seismic reflection surveys, and boreholes that penetrate salt sequences (Rodriguez et al. 2018). According to the last authors, these deposits can easily cover more than 100,000 km[2], varying in thickness from a few hundred to thousands of meters, and are usually deposited in restricted marine basins. They present a diverse mineralogical composition, mainly controlled by the solubility of different minerals. A standard depositional sequence will starts with carbonates, followed by gypsum (or anhydrite), then halite, and finally end with the bittern salts, such as potassium- and magnesium-rich minerals (Schreiber et al., 2007).

The evaporitic section in the Santos Basin (offshore Brazil) was regarded as fairly homogeneous in terms of interval velocity – around 4,500 m/s – until early 2000s. This assumption was considered as valid for processing, as the standard workflow included Pre-Stack Time Migration (PSTM). Following the discovery of oil in the pre-salt section in the Santos and Campos Basins, as well as the increase in computational power, Pre-Stack Depth Migration (PSDM) became the industry standard. Inside the PSDM's border-limit, a myriad of methods is available, ranging from Kirchhoff PSDM to Reverse-Time Migration (RTM). Completing the toolbox of state-of-the-art processing techniques are also Full-Waveform Inversion (FWI) (Ben-Hadj-Ali et al. 2008; Barnes & Charara (2009); Operto et al., 2013; Vigh et al., 2014) and Least-Squares Migration (LSM) as per discussed in (Nemeth et al., 1999; Hu et al., 2001; Dias et al., 2017; Wang et al., 2017; Dias et al., 2018).

To get more benefits from these improved processing techniques, models that assume a homogeneous salt layer are not an option, as they fail to reproduce the spatial variability of velocity. It is then mandatory to build more geologically-constrained velocity models. Without a good initial model, not even tomographic inversion is able to correctly update the velocities, due to the complex geological environment (e.g. strong contrasts, steep dips).

Some authors have explored the use of inhomogeneous/heterogeneous evaporitic sections for enhancing migration output (Gobatto et al., 2016; Fonseca et al., 2017; Fonseca et al., 2018; Maul et al., 2018b, 2018c, based on the statements of Maul

et al., 2015). Tarantola (1984) and Zhang & Wang (2009), among other authors, strongly indicate FWI and intrasalt tomography to update salt velocity models. Still, both methods need a good starting velocity model that, to some degree, represents the local geology. Huang et al. (2010) published results for velocity correction using tomographic inversion in the Santos Basin, considering the presence of layered evaporites. For these last authors, intrasalt travel times based on tomography yield good results because layered evaporites create strong reflections, ensuring the correct update. Ji et al. (2011) developed a method to update the salt velocity inserting a random velocity variation (called a *dirty salt velocity*) in a reflectivity-based inversion.

Following these considerations, Meneguim et al. (2015) demonstrated that the inversion study is more likely to deliver good salt velocity models than the simple amplitude approach firstly presented by Maul et al. (2015). Several other authors have explored the adaptive inversion concepts from the reservoir scale to the salt section scale (Gobatto et al., 2016; Toríbio et al., 2017; Teixeira et al., 2018; Fonseca et al., 2018). Barros et al. (2017) introduced the idea of generating pseudo-logs to fill log gaps, using the approach stablished by Amaral et al. (2015), who relied on cutting samples (mud-logs) collected during the well drilling phase. The use of mud-logs was also demonstrated to be useful in the work published by Cornelius & Castagna (2018).

In building the initial velocity model, well-logs are used to provide the missing bandwidth (lower frequencies) of seismic data. Careful pre-conditioning of velocity and density logs plays a crucial role in this step. These data are loaded into a stratigraphic grid (created from any previous seismic interpretation of top and base of the salt body) and interpolated. Seismic-well ties are used to estimate the best local wavelet, and a multi-well wavelet is selected as representative of the whole seismic data. The algorithm employed for inversion is sparse spike algorithm (Simm & Bacon, 2014). Data are then inverted for acoustic impedance, and comparison between the result and the well-logs is the most critical quality control. The inversion outcome is the base to obtain the seismic-derived properties of the salt layer.

In this paper, we propose a comparison among the several approaches for velocity model building in the salt section, such as constant value, tomographic update over constant velocity, insertion of stratification via instantaneous amplitude attributes, and insertion of stratification via acoustic inversion. A tomographic update over the inverted stratified model was

---

[1]Saline giants (*sensu*): Hsü (1972).
[2]Salt giants (*sensu*): Hübscher et al. (2007).

also performed, and the results were compared. We discuss some pitfalls, warnings and particularities which we consider as paramount when performing seismic inversion for the evaporitic section. All the consulted references regarding seismic inversion for the evaporitic section are summarized in Maul et al. (2018b, 2018c), and the methodology must follows important aspects. One of them is related to data quality to invert to rock property (e.g.: interval velocity, density), mainly because its the low-frequency contents and high noise-to-signal relation. As that matter is also a topic we will not explore in this article we will consider the data with enough quality for our study and tests.

STUDY AREA AND AVAILABLE DATA

The study area is inserted in the pre-salt province in the Santos and Campos Basins (Fig. 1). A pre-stack depth-migrated volume covering an area of approximately 200 km² is available, together with 14 wells with a broad suite of logs. The Agência Nacional do Petróleo, Gás Natural e Biocombustíveis (ANP) has provided the data we used in this research. Wells were labeled with capital letters from A to N, and the original names can be found in Table 1.

Table 1 – Correspondence between the well symbols for this study and the official names from ANP (National Agency of Petroleum – Brazil).

This Study	ANP
A	3-BRSA-788-SPS
B	9-BRSA-1037-SPS
C	8-SPH-23-SPS
D	8-SPH-13-SPS
E	7-SPH-14D-SPS
F	7-SPH-8-SPS
G	7-SPH-4D-SPS
H	9-BRSA-928-SPS
I	7-SPH-5-SPS
J	9-BRSA-1043-SPS
K	1-BRSA-594-SPS
L	7-SPH-1-SPS
M	7-SPH-2D-SPS
N	3-BRSA-923A-SPS

THE IMPORTANCE OF CHARACTERIZATION OF THE EVAPORITIC SECTION

Evaporites are minerals or rocks formed in a restricted saline environment, submitted to high evaporation rates. The great percentage of halite seems to be the main reason to consider the salt section as almost homogenous, with interval velocity Vp close to the halite's velocity (4,500 m/s), as this is the most frequent mineral within the salt section. However, a look at velocity models obtained by tomographic inversion reveals several inconsistencies, visible in the forms of large spots/marks of different velocities. These marks reflect the necessity to alter the almost constant initial velocity models.

Ji et al. (2011) presented enhanced results of depth positioning in PSDM data when considering seismic amplitudes as the guide for the existing heterogeneity inside the salt section. This improvement alone would be enough to justify the effort of using amplitudes for the velocity modelling. On top of that, it was also noticed that signal quality is improved when using this approach. Gobatto et al. (2016), Fonseca et al. (2018), and Maul et al. (2018a) presented processing results showing that use of salt stratification as input for velocity tomography leads to more realistic seismic images, and to more precise depth positioning and signal quality.

Maul et al. (2015) described how to incorporate salt stratifications using seismic attributes, assigning constant velocity values for those layers. Seismic amplitude is a response of contrasts of elastic properties between rocks. The estimation of layer properties from seismic data is an ill-posed problem (Tarantola, 1984), which bears a set of uncertainties. Seismic inversion is a widely applied technique to combine seismic amplitude, seismic interpretation and well-log information to obtain elastic properties from seismic amplitude (Latimer, 2011). The combination of information from several sources contributes to mitigate the ambiguity of the seismic signal, helping to solve part of the non-uniqueness of the solutions, as observed by Maul et al. (2015).

So far, about 200 wells were drilled to access the pre-salt reservoir in the Santos Basin (Maul et al., 2018b). These wells showed that the evaporites are, in fact, heterogeneous, with halite being the major fraction (between 80 and 90%). A division in three mineral groups was proposed: Low-Velocity Salts (LVS), or the bittern salts, composed basically by sylvite, carnallite and tachyhydrite; Halite (or background); and High-Velocity Salts (HVS), which are basically anhydrite and, in lower proportion, gypsum. The LVS group represents something between 5-10%
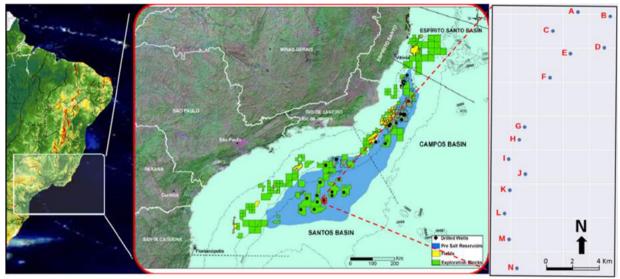
Figure 1 – Location of study area (regional) and details of available data. Blue polygon delineates the area of the hydrocarbon occurrences identified in the pre-salt province for both Santos and Campos Basins, totaling an area of approximately 350,000 km², and water column varying from 2,000 to 3,000 m. Rightmost panel shows in detail the well locations (A to N) inside the 3D seismic volume zone (rectangle). Adapted from https://diariodopresal.files.wordpress.com/2010/.

of occurrence, and the HVS group, 10-20%. These groups were considered enough to represent the different observed seismic signatures (Maul et al., 2015; Gobatto et al., 2016; Fonseca et al., 2018; Maul et al., 2018a).

Well-log analysis indicates an inverse relationship between thickness and velocity of the salt section. In areas where the evaporite sequence is thicker, velocity is slower. The Rayleigh-Taylor instability, as described by Lachmann (1910), Arrhenius (1913) and Dooley et al. (2015), can be a physical explanation: it states that under the intense overload pressure caused by the upper sediments, the more mobile salts (LVS) move to high-wall portions. The movement of the low-velocity salts towards the high-wall portions implies in a decrease of velocity in the thicker salt sections, caused by an increase in the fraction of low-velocity salts. This observation is consonant with the one made by Oliveira et al. (2015). The overload pressure moving the mobile salt to the "pillowed" portions is also mentioned by other authors, such as Ge et al. (1997) and Guerra & Underhill (2012).

METHODOLOGY

The proposed methodology in this work consists of:

A. Analysis of the available logs inside the evaporitic section. In this case we observe the presence/absence of data, as well as the property values registered;

B. Precautions regarding the use of samples collected during well drilling, and their associated uncertainties;

C. Interpretation of lithology in the wells, investigating the coupling degree, absence of logs, their description, and their correct positioning;

D. Investigating the property behaviors related to both, their measurement ways as well as considering about anomalous values, their own variability, inferring few commentaries regarding possible compaction effect by each mineral type;

E. Predict properties to insert in log gaps, or where only cuttings description are available. Particularly important for elastic logs;

F. Generation of any other important property for the seismic inversion approach (such as density) using log correlation;

G. Choice of a single and representative wavelet for the whole seismic inversion (in this case, it is important to think about section thickness variation, which could vary from few hundreds of meters to around 3 kilometers);

H. Performing a seismic inversion that reproduces the stratification observed in the well data, for the whole evaporitic section;

I. Obtaining internal stratification for the evaporitic section using other approaches, such as amplitude response, instantaneous seismic attributes, etc.;

J. Comparing the results.

CONSIDERATIONS, ASSUMPTIONS AND DEVELOPMENTS

A frequent challenge when modelling the salt section is the lack of log data at top and bottom of the evaporitic section, which is caused by operational constraints: these two places are usually selected for changing of casing diameter, making it difficult to acquire data from high-resolution acoustic logging. This argument is presented by Amaral et al. (2015), who argues in favor of using sample cuttings to fill this gap in information.

Figure 2 shows information on logs and cutting samples for the 14 studied wells. Notice that well D, for example, does not contain any LVS interpreted in neither approach.

Barros et al. (2017) proposed to use constant values (average logged values) for each of the mineral groups, in order to fill the gaps in the logs – i.e., assuming generated pseudo-logs as hard information. To do so, we will use the following average values: LVS = 4,188 m/s; Halite = 4,548 m/s; and HVS = 5,281. Those values were obtained from the PDF (probability density function) presented in Figure 3.

On the group of wells available for this study, about 10% of the section is not logged – in some cases, log absence is over 20%. Table 2 illustrates the data inventory for the studied wells, as well as some considerations about filling the log gap with the cutting samples description and the average velocity, following Barros et al. (2017).

After complementing the missing log information with the described cuttings, Barros et al. (2017) calculated the average occurrence per proposed group as following: LVS ~ 3.0%, Halite ~ 90.5%, and HVS ~ 6.5%. These percentages are in good agreement with values presented by Jackson et al. (2015) and Maul et al. (2018b), having the latter provided these percentages based on a database of 182 wells in the Santos Basin (Table 3). It is important to point out that the values obtained from this dataset should not be used as reference for any other study.

To generate the density logs – another input for the seismic inversion, we employed statistical regressions based on the registered logs (density X sonic), as can be seen in Figure 4.

As previously mentioned, the thickness of the evaporitic section in the Santos Basin varies from few hundreds of meters to about 3 kilometers. This variation imposes challenges when

deciding the single wavelet to perform the seismic inversion process. In this project, the thickness ranges from 1,200 to 2,400 meters, which is enough to produce too different wavelets to be represented for a single average one (Fig. 5). This can compromise the inversion, delivering results that would perhaps be deemed not suitable for reservoir characterization purposes, but still useful for our goals.

RESULTS

The results here presented cover two main aspects: the geological model building, by using the inversion methodology to build the evaporitic section (compared to other methods in literature), and how the use of this approach can influence the generation of new seismic images, depth positioning, migration, and focusing of events.

Figure 6A shows a seismic section, illustrating the amplitude responses inside the evaporitic section – the so-called stratifications. Figure 6B shows a velocity model with constant velocity for the evaporitic section (4,500 m/s), which was used as input for tomography, yielding the velocity presented in Figure 6C. If we use the amplitude response (Fig. 6A) to add stratification to the tomography output, we get a more geological look in our model, as can be seen in Figure 6D. Figure 6E shows the velocity obtained with the seismic inversion methodology.

The seismic inversion result is an impedance cube, and we are looking for an interval velocity cube. Following the idea showed in Figure 4, we can compute the correlation between impedance and interval velocity in well data. This was done independently for each of the three salt groups, using linear regressions, and the resulting equations were applied to the acoustic impedance obtained from inversion, yielding the desired 3D interval velocity.

The results show the inverse correlation between average interval velocity and section thickness (Fig. 7), for 10 of the 14 wells. This behavior was not observed in the remaining 4 wells. We believe this can be caused by problems in log data from these wells – the inverse relation is also described by Oliveira et al. (2015) after studying only three wells in another portion of in the Santos Basin, and by Maul et al. (2018b), in a study of 182 wells. It is in fact possible to use the impedance results to verify the same behavior spatially, as in Figure 8. This subject is currently in discussion and will likely be the scope of future work.

In another way, using Table 3 it is also possible to observe different behaviors when analyzing separately each mineral grouping per well. It allows us to infer when staying in thin
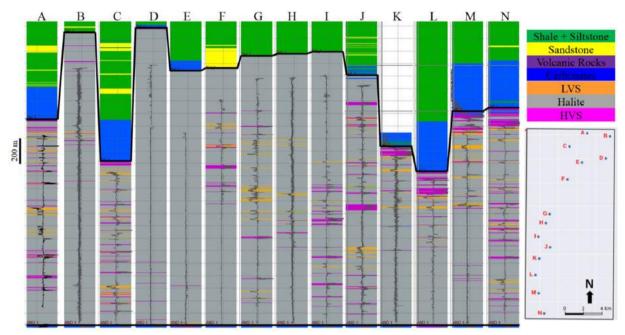
Figure 2 – Well section illustrating the registered logs and drill cuttings interpretation. Observe the absence of log information in almost all 14 wells.
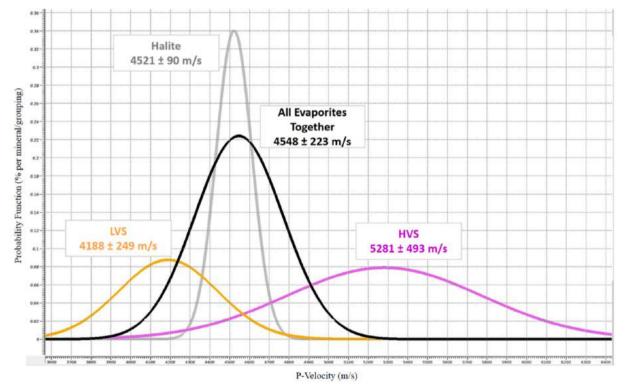

Figure 3 – Interval velocity behavior for each mineral/group, considering the 14 studied wells.

Table 2 – Well data inventory.

Well	EKB (m)	Basal Anhy-drite (m)	Water Column TVDSS (m)	Top of Salt TVDSS (m)	Salt Isopach (m)	Acquired Log (%)	Log Gap (%)	LVS Log & C.S. (%)	Halite Log & C.S. (%)	HVS Log & C.S. (%)	AIV Velocity (m/s)
A	25.00	12.90	-2125.00	-3264.81	1673.49	91.90	8.10	5.45	86.20	8.35	4589.59
B	24.00	13.80	-2122.00	-2734.32	2369.39	87.60	12.40	0.50	98.90	0.60	4550.39
C	24.00	12.90	-2146.00	-3722.50	1334.06	91.10	8.90	6.90	82.70	10.40	4599.39
D	24.00	11.50	-2119.00	-2717.34	2400.94	87.30	12.70	0.00	91.60	8.40	4609.57
E	24.00	11.14	-2179.00	-2885.90	2063.00	77.90	22.10	0.30	95.40	4.30	4578.44
F	24.00	17.50	-2182.00	-2876.91	2081.76	87.20	12.80	1.45	95.40	3.15	4565.87
G	24.00	13.57	-2129.00	-2804.89	2180.45	92.00	8.00	4.80	92.90	2.30	4547.58
H	24.00	11.50	-2120.00	-2798.11	2191.82	91.80	8.20	1.20	98.10	0.70	4548.81
I	26.00	13.80	-2126.00	-2809.53	2206.90	91.40	8.60	1.10	88.80	10.10	4618.07
J	26.00	13.40	-2140.00	-3088.84	2024.65	96.00	4.00	5.10	83.80	11.10	4611.00
K	32.00	11.50	-2140.00	-3553.21	1450.89	98.40	1.60	2.12	93.10	4.78	4575.41
L	26.00	29.40	-2143.00	-3717.59	1279.96	95.60	4.40	3.60	87.20	9.20	4602.48
M	26.00	11.65	-2143.00	-3256.49	1701.27	94.30	5.70	4.10	89.80	6.10	4577.95
N	26.00	13.30	-2157.00	-3340.66	1717.34	94.00	6.00	4.60	83.20	12.20	4620.87
AVG	**25.36**	**14.13**	**-2140.79**	**-3112.22**	**1905.42**	**91.18**	**8.82**	**2.94**	**90.51**	**6.55**	**4585.39**

EKB: Elevation Kelly-Bushing; TVDSS: True Vertical Depth Sub-Sea; LVS: Low-Velocity Salts; HVS: High-Velocity Salts; C.S.: Cutting Samples;

AVG: Average; AIV: Average Interval Velocity.

Table 3 – Salt proportions and interval velocities (m/s) for nine fields inside Santos Basin.

Field	# Wells	LVS (%)	LVS AIV	Halite (%)	Halite AIV	HVS (%)	HVS AIV	WIV
1	20	8	4018.56	83	4480.88	8	5210.27	4462.56
2	29	9	4218.47	82	4563.69	9	4975.84	4567.53
3	17	12	4054.42	77	4498.25	12	4989.92	4505.66
4	3	13	3971.00	71	4507.09	16	4927.59	4505.04
5	5	3	4167.00	84	4538.00	13	5123.33	4576.00
6	7	3	4264.19	80	4509.87	17	5061.36	4596.05
7	72	8	4122.33	81	4526.47	11	5105.84	4560.03
8	25	4	4182.53	88	4533.59	8	5003.35	4547.16
9	4	6	4055.63	81	4486.58	13	5077.49	4535.67
TNW	182							
AVG		**7**	**4117.13**	**81**	**4516.05**	**12**	**5052.78**	**4539.52**

LVS: Low-Velocity Salts; HVS: High-Velocity Salts; AIV: Average Interval Velocity; WIV: Weighted Interval Velocity;

TNW: Total Number of Wells; Interval Velocity (m/s); AVG: Average. Modified from Maul et al. (2018b).
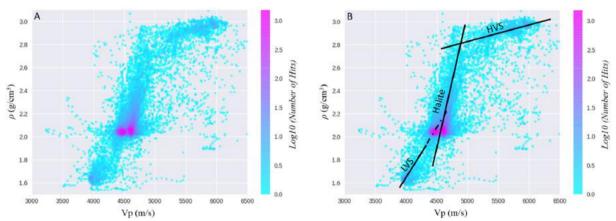
Figure 4 – Relation between density and instantaneous velocity (Vp). (A) Density X Interval Velocity; (B) Trend line for each proposed group (LVS, Halite and HVS). Notice that the Halite trend is more stable than the others. This is not surprising, since the other groups are in fact a mixing of minerals, while Halite – despite any mixing – has a monomineralic behavior.
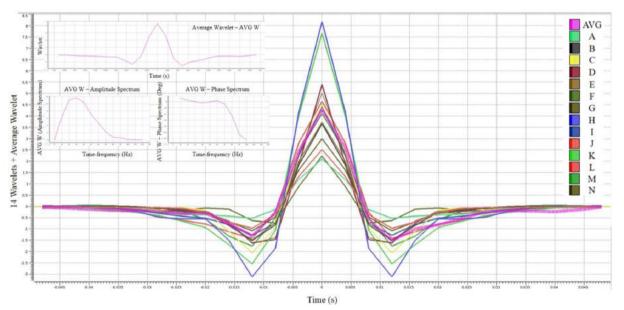

Figure 5 – Best wavelets for each of the 14 wells, and the average among them (purple). Observe the low representation of the average wavelet compared with the individual ones.

section we preferably have an increase in the HVS content or proportions which is reflected in the interval velocity increasing in these portions (Fig. 9). A feasible explanation is the fact during the period of more mobility observed for the Halite and the LVS, these salts under any overpressure condition tend to move to a any low-pressure portion such as the walls, pillows increasing their amounts in those places which consequently decreasing their velocity content. Another important aspect is the mineral mixing promotion during this moving which as per Justen et al. (2013)

statement helps to explain why the halite velocity is commonly measured below the value of 4,500 m/s, once the measurement reflects also the LVS content.

With the velocity models in hands, we can compare the output of processing workflows under different inputs. In this project, tomography and Kirchhoff PSDM were tested, using both the constant velocity model (Fig. 6B) and the impedance-derived one (Fig. 6E) as initial models. Results can be checked in Figure 10.
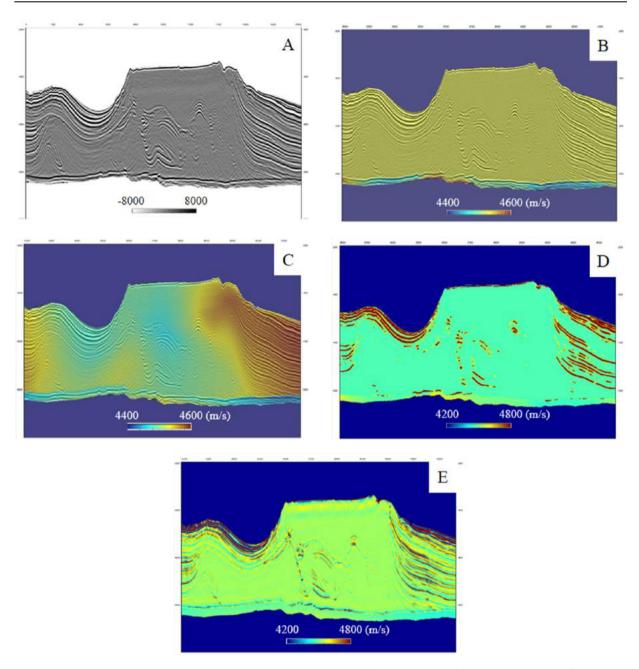
Figure 6 – The evaporitic section and the velocity behaviors in terms of geological features. (A) amplitude response; (B) constant interval velocity; (C) tomographic update in terms of velocity applied over "4B", which generated "4A"; (D) stratification insertion using the amplitude "4A" as the guide for this insertion; (E) stratification insertion using the seismic inversion methodology.

DISCUSSION

One hypothesis investigated during this research was that evaporitic sections show higher velocities in thin sections than in thicker sections. Results obtained from seismic inversion – even with a challenging wavelet estimation – are in agreement

with this. This assumption could also be inferred by observing the local geology, particularly the mini-basins under carbonate rafts: the heavy sediments in those mini-basins force the LVS to move to other positions, forming domes and walls. Therefore, the thin sections are left with a higher fraction of HVS, explaining their higher velocity.

Wells A, B, C, E, F, G, H, K, L and M

$$y = -0.0458x + 4657.4$$
$$R^2 = 0.7915$$

Figure 7 – Correlation between average interval velocity and salt thickness for the evaporitic section (10 of 14 wells displayed).

Figure 8 – Comparison between average interval velocity and thickness for the evaporitic section. (a) map of average interval velocity for the evaporitic section, with location of available wells (velocities were calculated from impedance volume); (b) map of thickness. Notice the same trend found in the cross-plot in Figure 7: thicker layers have slower interval velocity.

Figure 9 – Thickness section variation and the impact it may cause for each mineral/grouping. (A) thickness variation from the thinner section to the thicker; (B) average interval velocity per mineral/grouping per well. Note the influence the thickness appears to have of the HVS.

Figure 10 – Comparison between Kirchhoff migration with the tomographic updated for a constant initial model (Vp = 4,500 m/s) and for model with stratification. (A) migrated Kirchhoff crossline using the traditional tomographic updating for the velocity model (starting model Vp = 4,500 m/s); (B) the same crossline migrated using the Kirchhoff algorithm, now using the tomographic updating over the stratified model; (C) migrated Kirchhoff inline using the traditional tomographic updating for the velocity model (starting model Vp = 4,500 m/s); (D) the same inline migrated using the Kirchhoff algorithm, now using the tomographic updating over the stratified model. Orange arrows indicate positions where we observed imaging enhancement. Adapted from Maul et al. (2018a).

This is a point of attention for imaging and depth positioning under thick salt layers. Looking at the Figure 6, it is possible to notice many differences among the presented models. Although the tomographic update adds a flavor of geology even for constant-velocity starting models (Fig. 6C), the result is noticeably different from the one obtained from inversion results (Fig. 6E). Hence, tomographic update models with distinct initial conditions can lead to significant differences in depth positioning. Previous work regarding this theme (Meneguim et al., 2015) shows variations of +/- 3% in terms of gross rock volume above the oil-water contact.

Imaging enhancement has been reported in recent literature when accounting for stratification prior to tomography (Gobatto et al., 2016; Fonseca et al., 2017; Fonseca et al., 2018; Maul et al. 2018b). Besides better depth positioning and uncertainty reduction, event focusing is also improved. On this particular subject, there is plenty of room for development – the use of Least-Squares Migration (LSM), for example. These are the next steps in our research.

CONCLUSION

Seismic inversion for the evaporitic section is a suitable approach to start building reliable velocity models, even when the inversion output is not up to the standards of reservoir characterization. Using a stratified velocity as initial model for tomography update delivers clear benefits for the processing workflow, by reducing the computational time necessary for this intensive step. This is mostly due to incorporation of geology into the model, which brings it closer to the optimal solution and trims the number of necessary iterations.

The inverse relation between the evaporitic section thickness and its average interval velocities reinforces the mobile salts (LVS and Halite) expulsion hypothesis. Therefore, the HVS proportion is higher in thin sections. This is sometimes observed in thinner salt sections from tomographic updates of constant initial models, even without any geological input.

Both imaging and depth positioning are improved by using the stratified velocity model for tomography. These improvements can be carried even further by the use of migration algorithms that make better use of detailed velocity models, like Least-Squares Migration. Also, several other tasks can take advantage of better salt characterization, such as illumination studies, geomechanical simulations, and HSE during drilling operations.

REFERENCES

AMARAL PJ, MAUL A, FALCÃO L, GONZÁLEZ M & GONZÁLEZ G. 2015. Estudo Estatístico da Velocidade dos Sais na Camada Evaporítica na Bacia de Santos. In: 14th International Congress of the Brazilian Geophysical Society. Rio de Janeiro, RJ, Brazil. doi: 10.1190/sbgf2015-131.

ARRHENIUS S. 1913. Zur Physik der Salzlagerstätten. Medd. Vetensskapsakademiens Nobelinst, 2(20): 1-25.

BARNES C & CHARARA M. 2009. The Domain of Applicability of Acoustic Full-Waveform Inversion for Marine Seismic Data. Geophysics, 74(6): WCC91–WCC103. doi: 10.1190/1.3250269.

BARROS P, FONSECA J, TEIXEIRA L, MAUL A, YAMAMOTO T, MENEGUIM T, QUEIROZ LE, TORÍBIO T, MARTINI A, GOBATTO F & GONZÁLEZ M. 2017. Salt Heterogeneities Characterization in Pre-Salt Santos Basin Fields. In: OTC Brasil, Offshore Technology Conference. Rio de Janeiro, RJ, Brazil: IBP. doi: 10.4043/28147-MS.

BEN-HADJ-ALI H, OPERTO S & VIRIEUX J. 2008. Velocity Model Building by 3D Frequency-Domain, Full-Waveform Inversion of Wide-Aperture Seismic Data. Geophysics, 73(5): VE101-VE117. doi: 10.1190/1.2957948.

CORNELIUS S & CASTAGNA JP. 2018. Variation in Salt-Body Interval Velocities in the Deepwater Gulf of Mexico: Keathley Canyon and Walker Ridge Areas. Interpretation, 6(1): T15-T27. doi: 10.1190/INT-2017-0069.1.

DIAS BP, BULCÃO A, SOARES FILHO DM, SANTOS LA, DIAS RM, LOUREIRO FP & DUARTE FS. 2017. Least-Squares Migration in the Image Domain with Sparsity Constraints: an Approach for Super-Resolution in Depth Imaging. In: 15th International Congress of the Brazilian Geophysical Society. Expanded Abstracts. Rio de Janeiro, RJ, Brazil. doi: 10.1190/sbgf2017-236.

DIAS BP, GUERRA C, BULCÃO A & DIAS RM. 2018. Exploring Inversion Strategies in Image Domain Least Squares Migration. In: First EAGE/SBGf Workshop on Least Squares Migration. LMSTU01. Rio de Janeiro, RJ. Brazil. doi: 10.3997/2214-4609.201803060.

DOOLEY TP, JACKSON MPA, JACKSON CA-L, HUDEC MR & RODRIGUEZ CR. 2015. Enigmatic Structures within Salt Walls of Santos Basin – Part 2: Mechanical Explanation from Physical Modeling. Journal of Structural Geology, 75: 163-187. doi: 10.1016/j.jsg.2015.01.009.

FONSECA J, GOBATTO F, BOECHAT J, MAUL A, YAMAMOTO T, BORN E, TEIXEIRA L & GONZÁLEZ M. 2017. Dealing with Evaporitic Salts Section in Santos Basin during Geological Seismic Velocity Construction. In: 15th International Congress of the Brazilian Geophysical Society. Expanded Abstracts. Rio de Janeiro, RJ, Brazil. doi: 10.1190/sbgf2017-350.

FONSECA J, TEIXEIRA L, MAUL A, BARROS P, BOECHAT J & GONZÁLEZ M. 2018. Modelling Geological Layers into new Velocity Models for Seismic Migration Process: A Brazilian pre-salt Case. In: First EAGE/PESGB Workshop on Velocities. London, United Kingdom. doi: 10.3997/2214-4609.201800010.

GE H, JACKSON MPA & VENDERVILLE BC. 1997. Kinematics and Dynamics of Salt Tectonics Driven by Propagation. American Association of Petroleum Geologists Bulletin, Tulsa, Oklahoma, 81: 398-423.

GOBATTO F, MAUL A, FALCÃO L, TEIXEIRA L, BOECHAT JB, GONZÁLEZ M & GONZÁLEZ G. 2016. Refining Velocity Model within the Salt Section in Santos Basin: an Innovative Workflow to include the Existing Stratification and its Considerations. In: 86th Annual Meeting. SEG – Society of Exploration Geophysicist. Dallas, TX, USA. doi: 10.1190/segam2016-13685489.1.

GUERRA MCM & UNDERHILL JR. 2012. Role of Halokinesis in Controlling Structural Styles and Sediment Dispersal in the Santos Basin, Offshore Brazil. In: ALSOP GI, ARCHER SG, HARTLEY AJ, GRANT NT & HODGKINSON R (Eds.). Salt Tectonics, Sediments and Prospectivity. Geol. Soc. London, Special Public., 363: 175-206. doi: 10.1144/SP363.9.

HSÜ K. 1972. Origin of Saline Giants: A Critical Review after the Discovery of the Mediterranean Evaporite. Earth-Science Reviews, 8: 371–396. doi: 10.1016/0012-8252(72)90062-1.

HU J, SCHUSTER GT & VALASEK PA. 2001. Post-Stack Migration Deconvolution. Geophysics, 66: 939-952. doi: 10.1190/1.1444984.

HUANG Y, LIN D, BAI B, ROBY S & RICARDEZ C. 2010. Challenges in Pre-Salt Depth Imaging of the Deepwater Santos Basin, Brazil. The Leading Edge, 29(7): 820–825. doi: 10.1190/1.3462785.

HÜBSCHER C, CARTWRIGHT J, CYPIONKA H, DE LANGE GJ, ROBERTSON A, SUC J-P & URAI JL. 2007. Global Look at Salt Giants: Eos (Transactions, American Geophysical Union), 88: 177–182. doi: 10.1029/2007EO160002.

JACKSON CA-L, JACKSON MPA, HUDEC MR & RODRIGUEZ CR. 2015. Enigmatic Structures within Salt Walls of Santos Basin – Part 1: Geometry and Kinematics from 3D Seismic Reflection

and Well Data. Journal of Structural Geology, 75: 135-162. doi: 10.1016/j.jsg.2015.01.010.

JI S, HUANG T, FU K & LI Z. 2011. Dirty Salt Velocity Inversion: The Road to a Clearer Subsalt Image. Geophysics, 76(5): WB169–WB174. doi: 10.1190/GEO2010-0392.1.

JUSTEN JCR, VARGAS Jr EA, ALVES I & SOUZA ALS. 2013. Análise das Propriedades Elásticas de Rochas e Minerais Evaporíticos. In: 13th International Congress of Brazilian Geophysical Society. Rio de Janeiro, RJ, Brazil. doi: 10.1190/sbgf2013-237.

LACHMANN R. 1910. Über Autoplaste (Nichttektonische) Formelemente im Bau der Salzlagerstätten Norddeutschlands. Z. Dtsch. Geol. Ges., 62: 113-116.

LATIMER RB. 2011. Inversion and Interpretation of Impedance Data. In: BROWN AR. Interpretation of Three-Dimensional Seismic Data. Society of Exploration Geophysicists and American Association of Petroleum Geologists, Tulsa, Oklahoma, USA. p. 309–350. doi: 10.1190/1.9781560802884.ch9.

MAUL A, JARDIM F, FALCÃO L & GONZÁLEZ G. 2015. Observing Amplitude Uncertainties for a pre-salt Reservoir using Illumination Study (Hit-Maps). In: 77th EAGE Conference & Exhibition. Madrid, Spain. doi: 10.3997/2214-4609.201412921.

MAUL A, FONSECA J, TEIXEIRA L, BARROS P, BOECHAT JB, NUNES JP, YAMAMOTO T, GONZÁLEZ M & GONZÁLEZ G. 2018a. Modelling Intra-Salt Layers when Building Velocity Models for Depth Migration. Examples of the Santos Basins, Brazilian Offshore. In: 88th Annual Meeting. SEG – Society of Exploration Geophysicist. Anaheim, CA, USA. doi: 10.1190/segam2018-2996209.1.

MAUL A, SANTOS MAC & SILVA CG. 2018b. Evaporitic Section Characterization and its Impact over the pre-salt Reservoirs, Examples in Santos Basin, Offshore. In: Rio Oil & Gas Expo & Conference 2018. Rio de Janeiro, RJ, Brazil. IBP.

MAUL AR, SANTOS MAC & SILVA CG. 2018c. Few Considerations, Warnings and Benefits for the E&P Industry when Incorporating Stratifications inside Salt Sections. Brazilian Journal of Geophysics, 36(4): 461-477. doi: 10.22564/rbgf.v36i4.1981.

MENEGUIM T, MENDES SC, MAUL A, FALCÃO L, GONZÁLEZ M & GONZÁLEZ G. 2015. Combining Seismic Facies Analysis and Well Information to Guide new Interval Velocity Models for a pre-salt Study, Santos Basin, Brazil. In: 14th International Congress of the Brazilian Geophysical Society. Rio de Janeiro, RJ, Brazil. doi: 10.1190/sbgf2015-271.

NEMETH T, WU C & SCHUSTER GT. 1999. Least-Squares Migration of Incomplete Reflection Data. Geophysics, 64: 208–221. doi: 10.1190/1.1444517.

OLIVEIRA LC, FALCÃO L, MAUL A, ROSSETO JA, GONZÁLEZ M & GONZÁLEZ G. 2015. Geological Velocity Approach in order to obtain a detailed Velocity Model for the Evaporitic Section, Santos Basin. In: 14th International Congress of the Brazilian Geophysical Society. Rio de Janeiro, RJ, Brazil. doi: 10.1190/sbgf2015-273.

OPERTO S, GHOLAMI Y, PRIEUX V, RIBODETTI A, BROSSIER R, METIVIER L & VIRIEUX J. 2013. A Guided Tour of Multiparameter Full-Waveform Inversion with Multicomponent Data: from Theory to Practice. The Leading Edge, 32: 1040–1054. doi: 10.1190/tle32091040.1.

RODRIGUEZ CR, JACKSON CA-L, ROTEVATN A, BELL RE & FRANCIS M. 2018. Dual Tectonic-Climatic Controls on Salt Giant Deposition in the Santos Basin, Offshore Brazil. Geosphere, 14(1): 215-242. doi: 10.1130/GES01434.1.

SCHREIBER BC, BABEL M & LUGLI S. 2007. An Overview of Evaporite Puzzles. In: SCHREIBER BC, LUGLI S & BABEL M (Eds.). Evaporites through Space and Time. Geological Society, London, Special Publication, 285. doi: 10.1144/SP285.2.

SIMM R & BACON M. 2014. Seismic Amplitude: An Interpreter's Handbook. Cambridge Press. 271 pp.

STEFANO L, MANZI V, ROVERI M & SCHREIBER BC. 2010. The Primary Lower Gypsum in the Mediterranean: A new Facies Interpretation for the First Stage of the Messinian Salinity Crisis. Palaeogeography, Palaeoclimatology, Palaeoecology, 297: 83–99. doi: 10.1016/j.palaeo.2010.07.017.

TARANTOLA A. 1984. Inversion of Seismic Reflection Data in the Acoustic Approximation. Geophysics, 49: 1259–1266. doi: 10.1190/1.1441754.

TEIXEIRA L, NUNES JP, FONSECA J, MAUL A, BARROS P & BORGES F. 2018. Seismic-Based Salt Characterization for Geomechanical Modelling of a pre-salt Reservoir. In: 80th EAGE Conference & Exhibition. Copenhagen, Denmark. doi: 10.3997/2214-4609.201801331.

TORÍBIO T, QUEIROZ LE, TEIXEIRA L, YAMAMOTO T, MENEGUIM T, LEONARDI O, CORTEZ M, RELVAS MT, MOLITERNO AM, TARTARINI A, FONSECA J & MAUL A 2017. Characterizing Evaporitic Section and Geomechanical Properties using Seismic Inversion, a Case Study for Santos Basin. In: 15th International Congress of the Brazilian Geophysical Society. Rio de Janeiro, RJ, Brazil. doi: 10.1190/sbgf2017-226.

VIGH D, JIAO K, WATTS D & SUN D. 2014. Elastic Full-Waveform Inversion Application using Multicomponent Measurements of Seismic Data Collection. Geophysics, 79(2): R63–R77. doi: 10.1190/geo2013-0055.1.

WANG P, HUANG H & WANG M. 2017. Improved Subsalt Images with Least-Squares Reserve Time Migration. Interpretation, 5(3): SN25-SN32. doi: 10.1190/INT-2016-0203.1.

ZHANG Y & WANG D. 2009. Traveltime Information-Based Wave-Equation Inversion. Geophysics, 74(6): WCC27–WCC36. doi: 10.1190/1.3243073.

Brazilian Journal of Geophysics

RBGf

3D GRAVITY MODELING OF IMPACT STRUCTURES IN BASALTIC FORMATIONS IN BRAZIL: PART II – VISTA ALEGRE, PARANÁ

Júlio César Ferreira[1], Emilson Pereira Leite[2],
Marcos Alberto Rodrigues Vasconcelos[3] and Alvaro Penteado Crósta[2]

ABSTRACT. This study characterized the subsurface framework of the Vista Alegre impact structure in terms of a 3D mass density model obtained from forward gravity modeling, constrained by petrophysical and geological data from a previously published work. Like the nearby Vargeão impact structure, Vista Alegre is a complex impact structure formed in basaltic lava flows of the Serra Geral Formation with a central uplift exposing sandstones of Piramboia/Botucatu Formations and impact breccias. A 3D mass density model is proposed, consisting of five subsurface layers: polymictic breccias, shocked/fractured basalts, basalts (Serra Geral), shocked sandstones (Piramboia/Botucatu) and a lower layer of pre-Triassic sedimentary rocks. The central region containing the fractured polymictic breccias and shocked target rocks (basalt and sandstone) is ∼100 m thick. The target rocks are deformed at depths of up to ∼1 km, which represents the basal contact of the sandstones of the Piramboia/Botucatu Formations with pre-Triassic strata. Values of structural uplift (∼650 m), central uplift diameter (∼3.5 km) and depth of excavation (∼400 m) inferred from our model are fairly consistent with theoretical values, thus supporting a meteoritic impact nature. The Vista Alegre model is in agreement with the density model for the nearby Vargeão impact crater and provides new insights into the formation of impact structures in basaltic targets, with potential implications for the study of other planetary surfaces.

Keywords: density modeling, impact crater, central uplift, Serra Geral Formation.

RESUMO. Este estudo apresenta uma caracterização em subsuperfície da estrutura de impacto Vista Alegre em termos de um modelo 3D de densidade de massa obtido a partir de uma modelagem direta de dados gravimétricos, vinculada a dados petrofísicos e dados de mapeamento geológico previamente publicados. Assim como a cratera de Vargeão, Vista Alegre é uma estrutura de impacto complexa, formada em fluxos de lava da Formação Serra Geral, com elevação central expondo arenitos das Formações Piramboia/Botucatu e brechas de impacto. Foi proposto um modelo constituído por cinco camadas em subsuperfície: brechas polimíticas, basaltos fraturados, basaltos (Serra Geral), arenitos (Piramboia/Botucatu) e uma camada inferior de rochas pré-Triássicas. A região central contendo as brechas polimíticas e as rochas-alvo fraturadas (basaltos e arenitos) tem ∼100 m de espessura. As rochas da região do impacto estão modificadas até profundidades de ∼1 km, onde ocorre o contato entre as camadas pré-Triássicas e os arenitos das Formações Piramboia/Botucatu. Valores de soerguimento estrutural (∼650 m), diâmetro do núcleo central soerguido (∼3,5 km) e profundidade de escavação (∼400 m) são consistentes com valores teóricos que podem ser inferidos do nosso modelo, reforçando a origem por impacto meteorítico. Em geral, o modelo de Vista Alegre está de acordo com o modelo de densidades da cratera de impacto de Vargeão e fornece novos conhecimentos sobre a formação de estruturas de impacto em alvos basálticos e para estudos de geologia planetária.

Palavras-chave: modelo de densidades, cratera de impacto, núcleo soerguido, Formação Serra Geral.

[1]Refinaria de Paulínia (Replan). Rodovia SP 332 – Km 130 13147-900 Paulínia, SP, Brazil – E-mail: juliocferr@petrobras.com

[2]Universidade Estadual de Campinas, Instituto de Geociências, Departamento de Geologia e Recursos Naturais, Rua João Pandiá Calógeras, 51 - Cidade Universitária 13083-970 Campinas, SP, Brazil – E-mails: emilson@ige.unicamp.br, alvaro@ige.unicamp.br

[3]Universidade Federal da Bahia, Instituto de Geociências, Departamento de Geofísica, Rua Barão de Jeremoabo, S/N, Campus Universitário de Ondina 40170-290 Salvador, BA, Brazil – E-mail: marcos.vasconcelos@ufba.br

INTRODUCTION

As mentioned in Part I (Ferreira et al., 2015), our work consisted in a detailed ground gravimetric survey of Vargeão and Vista Alegre impact structures, distant around 100 km apart in a similar geological context (Fig. 1). Therefore, we divided this work into two parts: Part I presents the results obtained from gravity data acquired at Vargeão impact structure (Ferreira et al., 2015); Part II brings the results obtained for the Vista Alegre impact structure. A general introduction about impact craters, basaltic targets and the application of gravity data for studying them is presented by Ferreira et al. (2015).

Similar to the slightly larger Vargeão impact structure, the Vista Alegre structure is a relatively eroded impact crater, which hampers the direct investigation of its morpho-structural features. In such cases, the application of geophysical methods becomes important to map the distribution of physical properties that can be associated with geological features and structures in subsurface (Pilkington & Grieve, 1992).

The Vista Alegre structure was the subject of a ground gravimetric survey aiming to generate a subsurface model that delimits the different geological layers and identifies post-impact stratigraphic changes.

In particular, we present a 3D subsurface mass density model of the Vista Alegre impact structure obtained from modeling gravity data. This model was geologically interpreted, depicting basement depth, layers thicknesses and geometrical characteristics of the central uplift.

The Vista Alegre gravity model is compared to that obtained for Vargeão to respond to the specific questions formulated in Part I (Ferreira et al., 2015): "(i) Even though the two structures are relatively close to each other, are they similar in terms of subsurface geology? (ii) Have one of the two impacts affected the subsurface more than the other? (iii) Are the volume and shape of possible uplifted sandstone similar?". It is rather important to notice that the elevation of the center of the Vista Alegre structure is relatively inconspicuous; therefore subsurface models such as the one presented here can disclose the framework of the central uplift.

The Vista Alegre impact structure

Centered at 25°57'S and 52°41'W, the Vista Alegre structure is located in the county of Coronel Vivida-PR (Fig. 2). The structure was named after the Vista Alegre village, located in the northwestern portion of the structure, in between the center and the rim. It was first described in 2004, with the aid of satellite

images, as a circular depression with morphology, structures and deformation that could be the result of a meteorite impact, similar to that of Vargeão impact structure (Crósta et al., 2004). Later studies have found and described the impact evidence necessary to prove the structure as being of impact origin and provided details of its morphology (Crósta et al., 2010).
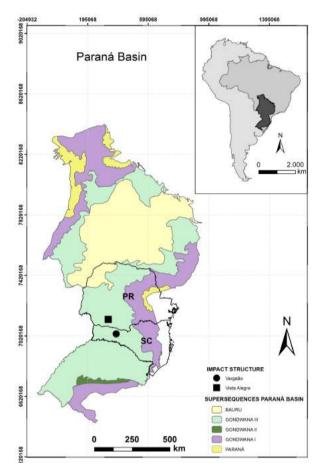

Figure 1 – Geological map of the Paraná Basin (adapted from Milani et al., 1998). Vargeão and Vista Alegre impact structures are located in the states of Santa Catarina and Paraná, respectively. A summary of the regional geology is presented in Part I (Ferreira et al., 2015).

With a diameter of ∼9.5 km, it has also been described as a complex impact structure. The presence of subtle topographic elevations (Crósta et al., 2010) and the anomalous presence of sandstones in the central portion of the Piramboia/Botucatu Formations, within a circle of 3 km diameter, indicate the presence of a central uplift (Crósta, 2012).

Having a circular rim in the form of a ring of escarpments and an internal depression, the structure's boundaries are well delimited with the exception of its south and southwestern edges, which were removed by the erosive action of the Chopin River.
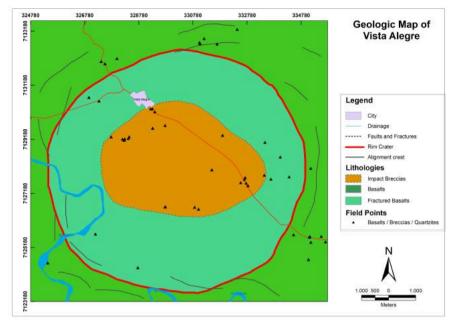
Figure 2 – Generalized geological map of the Vista Alegre impact structure (Furuie, 2006).

An unconstrained maximum age of 125 Ma for the Vista Alegre impact structure can be drawn from the age of the Serra Geral volcanism (Crósta et al., 2013), as the structure was formed on basaltic flows with a Cretaceous age range between 139 and 125 Ma (Turner et al., 1994). Crósta et al. (2010) provided a geological characterization and complete description of Vista Alegre as an impact structure. That study was based on geomorphological analyses conducted on the SRTM digital elevation model and on field geological observations that led to the identification of impact evidence, such as the occurrence of shatter cones and planar deformation features in quartz grains from polymict breccias.

Local Geology

Crósta et al. (2010) describe the area of the impact crates with basalts and shocked/fractured basalts of the Serra Geral Formation, polymictic impact breccias and sedimentary layers underlying the Serra Geral Formation (Fig. 2). The Serra Geral Formation corresponds to tholeiitic basalts. Fractured basalts are found in an annular area between the rim and the center of the structure. This fracturing is relatively strong and attributed to effects of the impact and later deformation processes of the modification stage of the crater formation (Crósta et al., 2013). The polymictic lithic breccias formed directly by the impact process as a mixture of the target rocks. They occur in

a circular area of approximately 20 km^2 in the central portion of the structure, forming a continuous layer underlying the soil, with thicknesses ranging from 8 to 12 m, according to inferences based on observations of breccia outcrops presented in Furuie (2006) and Crósta et al. (2013). The sedimentary layers underlying the Serra Geral Formation were not represented because in-situ sandstone outcrops are rarely found. Those rocks are normally located between 700 to 900 m deep in the region outside the Vista Alegre structure (Furuie, 2006). However, there are small sandstone occurrences around the center of the structure, as lose blocks found mixed with red soils which are a typical product of weathering of the rocks of the Serra Geral Formation. These quartzose rocks were interpreted as being brought to the near surface as a result of uplift of the sedimentary rocks of the Piramboia or Botucatu Formations (Crósta et al., 2013)

METHODOLOGY

Vista Alegre ground gravimetric data were acquired during a field campaign in 2013 using a CG-5 Scintrex gravimeter along with a Trimble ProXT DGPS for geometrical height measurements. The reader is referred to Part I for details about the resolution and accuracies of those instruments (Ferreira et al., 2015). The survey was carried out mainly along roads covering the entire area of the structure (Fig. 3). Gravity data were collected at 343 locations,
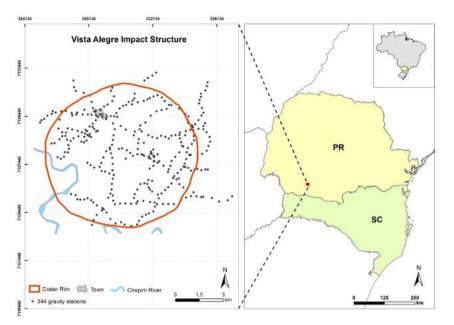
Figure 3 – Spatial distribution of the ground gravimetric stations within and around the Vista Alegre impact structure.

most of them spaced from 200 to 500 m apart. All data were georeferenced to the WGS 84 Datum and UTM projection in zone 22S was applied. A minimum curvature algorithm was used to interpolate the observed data into a regular grid with cells of 50 m x 50 m (Ferreira et al., 2015). Data were not collected in the southwestern limit of the structure, due the presence of the Rio Chopim (Fig. 3) that prevented access to this region.

Data processing

We performed a regional-residual separation by fitting a second-degree polynomial surface to the total Bouguer anomaly and subtracting this surface from the total Bouguer anomaly, resulting in the residual Bouguer anomaly. The subsequent modeling was then performed using the residual Bouguer anomaly as observed data. The relevant equations are found in Ferreira et al. (2015).

3D gravity forward modeling

Forward modeling was carried out using GMSYS-3D software, available in Geosoft Oasis Montaj® (Popowski et al., 2006), in the same way as that described in Ferreira et al. (2015). Based on the available geological map, we used the following set of rock layers in our model, from the deepest to the shallowest: (1) Pre-Triassic units; (2) Sandstones of the Piramboia and Botucatu Formations; (3) Basalt; (4) Shocked/fractured basalt; (5) Impact breccias. We used absolute density values measured from rock

samples representing each layers to constrain our model. The modeling algorithm discretizes the entire interpretative volume into a mesh with a constant density assigned to each cell. Our model has 217 x 193 x 56 cells along the EW, NS and vertical directions, respectively, each measuring 50 x 50 x 20 m.

RESULTS AND DISCUSSIONS

Total, regional and residual Bouguer anomalies of the Vista Alegre impact structure are depicted in Figure 4. A nearly circular negative anomaly is associated with the center of the structure. That gravity signature can be related to the higher degree of deformation expected to occur at the center of an impact structure (Grieve, 1987). For Vista Alegre, the residual Bouguer anomaly has a minimum value of -2.5 mGal in its central region (Fig. 4C). Surrounding the center of the crater, the data depict a ring of highly variable amplitudes (from 0.5 to 1.1 mGal). The Vargeão structure exhibits a similar ring, but completely closed and showing lower values (Ferreira et al., 2015), although not so well defined as in Vista Alegre. Additionally, the Vista Alegre anomaly decreases outwards, so that the crater rim does not show any typical signature.

3D density model

The 3D model (Fig. 5) includes, from bottom to top: a base layer of pre-Triassic rocks, followed by a sandstone layer and a basalt layer. Layers of shocked/fractured basalts and impact breccias
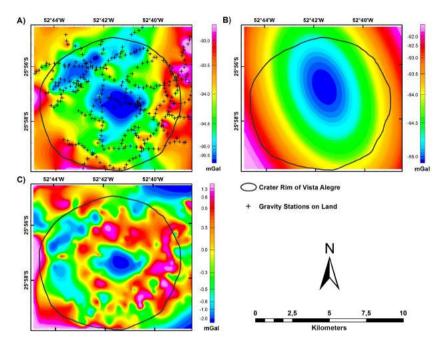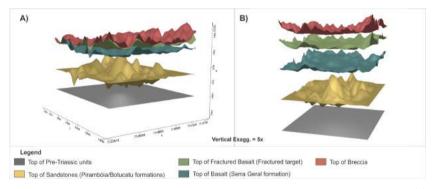
Figure 4 – Bouguer anomalies of the Vista Alegre impact structure. (A) Total gravity anomaly; (B) Regional anomaly; (C) Residual anomaly comprised by the difference between grids of total gravity anomaly and regional anomaly.
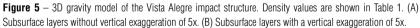

Figure 5 – 3D gravity model of the Vista Alegre impact structure. Density values are shown in Table 1. (A) Subsurface layers without vertical exaggeration of 5x. (B) Subsurface layers with a vertical exaggeration of 5x.

Table 1 – Densities of rock samples extracted from Vista Alegre.

Lithology	Densities (g/cm³)			
	min	max	average	SD
Sandstones Piramboia / Botucatu	2.41	2.44	2.43	0.01
Alto Uruguai Basalt	2.84	2.95	2.88	0.04
Fractured Basalt	2.66	2.82	2.74	0.06
Impact Breccia	2.27	2.48	2.39	0.05

are also represented in the upper part of the model, both of them filling the annular cavity of the impact structure. Similarly to the procedure used for Vargeão (Ferreira et al., 2015), the density values shown in Table 1 were defined based on densities measured from real samples by Yokoyama (2013), except for the layer of more acidic volcanic rocks (the Acidic Chapecó unit). These densities were measured using a precision balance and applying the methodology described in Ferreira (2017). The crater rim and the layer thicknesses were defined based on Furuie (2006) and Milani et al., (1998), respectively.

Figure 6 shows the fitting between calculated (forward modeling) and observed anomalies, as well as their histograms. Comparison of the Bouguer residual anomaly map (Fig. 6A) with the modeled field (Fig. 6B) displays consistent spatial distribution and values, which is also reinforced by the information shown in the histograms. As observed in Figure 6C, the mean error is -0.07 mGal and the standard deviation is 0.42 mGal. However, because of interpolation artefacts, higher amplitude errors occur particularly at the edges of the map and in some areas where there are no observation points.

To better interpret the subsurface of the impact structure and the distribution of rock densities, four vertical sections were extracted from the 3D model. The profiles A-A' and B-B' (Fig. 7), and C-C' and D-D' (Fig. 8) were extracted along the N-S, W-E, NW-SE and NE-SW directions. A layer of varying from 500 to

800 m thick of Serra Geral basalt is observed superposing rocks of the 300 to 400 m thick Piramboia/Botucatu Formations. The model depicts a classic shape of a complex impact structure with a ~300m uplift of the less dense Piramboia/Botucatu Formation. This uplift is surrounded by two types of rock that are related to the impact: shocked/fractured basalts and polymictic breccias. The top of the pre-Triassic units, at ~700 m depth, is a good inference of the maximum depth that the impact-related deformation have reached, as the residual field was reduced to satisfying amplitudes without deforming such horizons. Both B-B' and C-C' profiles in (Figs. 7 and 8) were used to estimate the crater rim and then to suggest a structure with a diameter of ~9.5 km, agreeing with the crater size defined by Crósta et al. (2004) and Crósta et al. (2010).

Each layer of the model (Fig. 5) was isolated in order to better interpret its 3D shape. The uppermost layers, corresponding to shocked/fractured basalts and impact breccias, have been estimated to be ~100 m thick (Fig. 9). We observe that breccias have a wide occurrence surrounding the center and in the eastern portion, reaching a maximum thickness of 30 m and an average of 8.5 m. The works of Furuie (2006) and Crósta et al. (2013) also inferred that the polymorphic breccias have thickness between 8 and 12 m around the center, which is in accordance with our model. Underneath the shocked/fractured basalt, there is a ~500 m thick layer of unfractured basalt of the Serra Geral Formation corresponding to the floor of the transient cavity. These
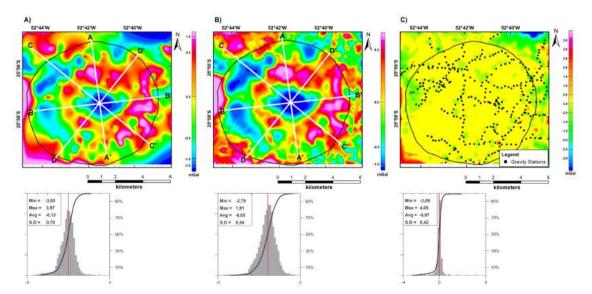

Figure 6 – Comparison among residual Bouguer anomalies. (A) Observed; (B) Calculated from the 3D mass density model; (C) Difference between grids in A and B. Data in the corresponding histograms are in mGal. White lines represent positions along which vertical sections were extracted from the model. Solid black lines represent the crater rim.
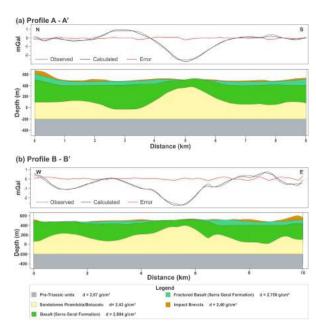
(a) Profile A - A'

(b) Profile B - B'

Legend

Pre-Triassic units   d = 2,67 g/cm³
Sandstones Pirambóia/Botucatu   d= 2,43 g/cm³
Basalt (Serra Geral Formation)   d = 2,684 g/cm³
Fractured Basalt (Serra Geral Formation)   d = 2,750 g/cm³
Impact Breccia   d = 2,40 g/cm³

Figure 7 – Vertical profiles extracted from the 3D gravity model of Figure 5 along (a) A-A' profile and (b) B-B' profile. Vertical exaggeration is 2x. The zero in the vertical scale corresponds to the EGM96 vertical datum that was used to calculate the SRTM model.

(a) Profile C - C'

(b) Profile D - D'

Legend

Pre-Triassic units   d = 2,67 g/cm³
Sandstone Pirambóia/Botucatu   d= 2,43 g/cm³
Basalt (Serra Geral Formation)   d = 2,684 g/cm³
Fractured Basalt (Serra Geral Formation)   d = 2,750 g/cm³
Impact Breccia   d = 2,40 g/cm³

Figure 8 – Vertical profiles extracted from the 3D gravity model of Figure 5 along (a) C-C' profile and (b) D-D' profile. Vertical exaggeration is 2x. The zero in the vertical scale corresponds to the EGM96 vertical datum that was used to calculate the SRTM model.

Vertical Exagg. = 3x

Fractured Basalt (Fractured target)
Impact Breccia

Figure 9 – Polymictic breccias (orange) and fractured basalts (green) isolated from the 3D model. Vertical exaggeration is 3x.

Vertical Exagg. = 3x

Basalt (Serra Geral Formation)

Figure 10 – Serra Geral basalts isolated from the 3D model. Vertical exaggeration is 3x.

unfractured basalts reach depths of $\sim$400 m (Fig. 10). Based on data acquired from 13 complex impact structures in igneous and sedimentary targets, Grieve et al. (1981) propose a model to estimate the depth of excavation (d_e) in complex structures. That value is calculated as $d_e = 0.09 - 0.12D_e$, where D_e is related to the final crater diameter D by $D_e = 0.5 - 0.65D$. This quantity defines a range between a minimum value (igneous targets) and a maximum value (sedimentary targets). After applying these values to Vista Alegre, we found that d_e could vary between 420 and 750
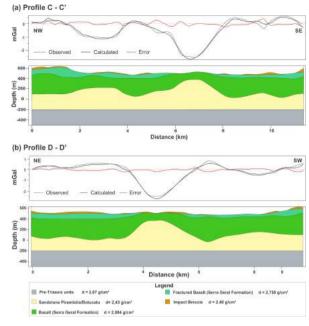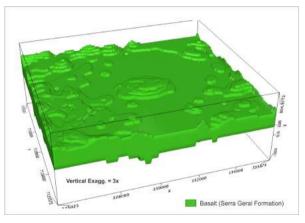
m. Because the impact has occurred on an igneous target, the minimum value of 420 m is consistent with the interpretation of our model.

The central uplift of Vista Alegre

Although there is no topographic relief that can be directly related to the presence of a central uplift, Furuie (2006) and Crósta et al. (2010) inferred it from the occurrence of sandstone clasts in the breccias and blocks of sandstones found at the
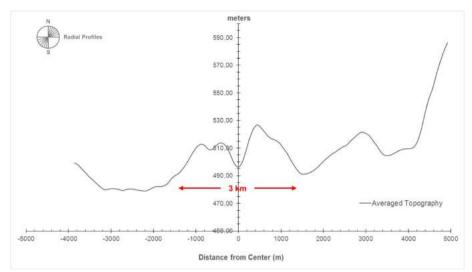
Figure 11 – Average elevation profile of the Vista Alegre impact structure. Values are based on 10 radial elevation profiles. The zero distance is at the center of the structure.
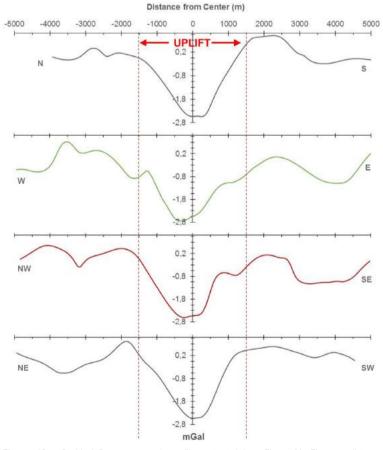

Figure 12 – Residual Bouguer anomaly profiles extracted from Figure 6A. The zero distance corresponds to the center of the central uplift.
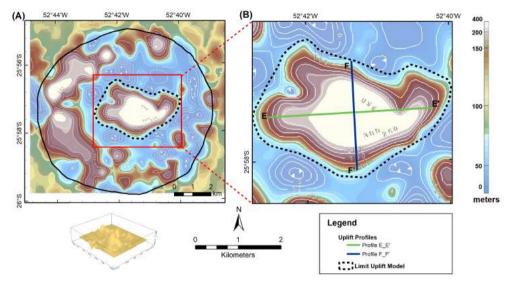
Figure 13 – (A) Depth to the top of the sandstone layer of the Vista Alegre impact structure. (B) Inset with two profiles along which residual anomalies were extracted to examine the central uplift in the model.

center of the crater. As there are no stratigraphic units with sandstones over the Serra Geral Formation in this part of the Paraná Basin, it is realistic to interpret those blocks as related to the underlying Piramboia/Botucatu sandstones. Our model depicts a stratigraphic uplift defined by the sandstone layer. Average elevations of 10 radial profiles from North to South crossing the center of the structure shows that such uplift is almost symmetric with respect to the central zero, having an elevation of ∼50 m and a diameter of ∼3 km (Fig. 11). Gravity profiles extracted from Figure 6A are quite similar and a central negative anomaly of ∼2.5 mGal stands out (Fig. 12). That central negative anomaly reflects a negative density contrast between sandstones and basalts. The red dashed line is symmetric with respect to the central point and represents the boundary of this ∼3 km diameter anomaly.

The uplifted block presents a nearly elliptical shape with an E-W major axis (∼3.5 km length) and a N-S minor axis (∼2 km length) (Figs. 13 and 14). Therriault et al. (1997) have established a linear fit between crater diameter (D) and central uplift diameter (D_{CU}), which reads as $D_{CU} = 0.31D^{1.02}$. Applying this equation to the Vista Alegre structure leads to a central uplift diameter of ∼3 km, which is roughly in agreement with a mean diameter inferred from the residual Bouguer anomaly and from the elevation profile.

As shown in Figure 14, the central uplift contains both the sandstone layer and the basalt layer. The basalt layer has its lower and upper limits at approximately -200 and 450 m, respectively,

leading to a total structural uplift (SU) of ∼650 m. This amount of uplift is somewhat in agreement with that estimated from a classic empirical linear model, $SU = 0.06D^{1.1}$ (Grieve et al., 1981), where D is the crater diameter, which would result in an uplift of ∼714 m.
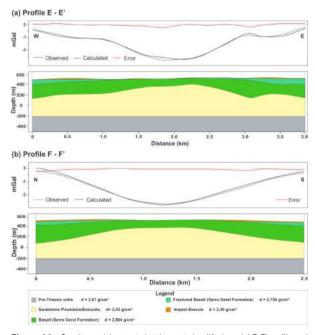

Figure 14 – Gravity model extracted at the central uplift along (a) E-E' profile and (b) F-F' profile shown in Figure 13. Vertical exaggeration is 2x. The zero in the vertical scale corresponds to the EGM96 vertical datum that was used to calculate the SRTM model.
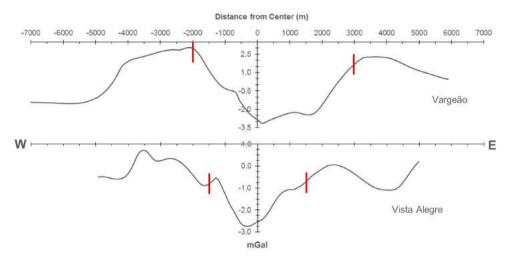
Figure 15 – Profile of the Bouguer anomaly along the E-W direction comparing both structures Vargeão (uppermost profile) and Vista Alegre (lowermost profile). Red lines point out the limits of the negative anomaly.
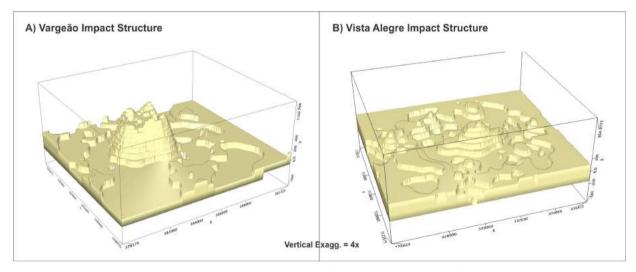

Figure 16 – 3D density models restricted to the Piramboia/Botucatu sandstones. (A) Vargeão (Ferreira et al., 2015); (B) Vista Alegre. Vertical exaggeration is 4x.

The uplifted basalt layer with an average thickness of 100 m above the uplifted sandstone layer (Fig. 10) explains why large outcrops of sandstones are not found in the central region of the Vista Alegre impact structure. However, a few sandstone lose blocks of the Piramboia/Botucatu Formations are exposed at the center of the crater, indicating erosion of the basaltic rocks.

Variations in elevation of the Serra Geral layer are in agreement with those expected for complex structures (Fig. 18). The only difference is that the central portion of the Vargeão model is open due the more prominent uplift of the underlying Botucatu/Piramboia sandstones.

Similarities and differences between Vargeão and Vista Alegre impact structures

Vargeão and Vista Alegre structures share some general characteristics, such as their morphology and types of rocks involved in the impact event. In both cases, sandstones of the Botucatu/Piramboia Formations were uplifted and exposed at the center, although the exposure has larger extents in Vargeão in comparison with Vista Alegre. Their central uplift diameters are different, with Vargeão structure ~2 km larger than Vista Alegre. Both density models obtained from gravity inversion were similar, except for the layer of acid volcanics that occurs in Vargeão
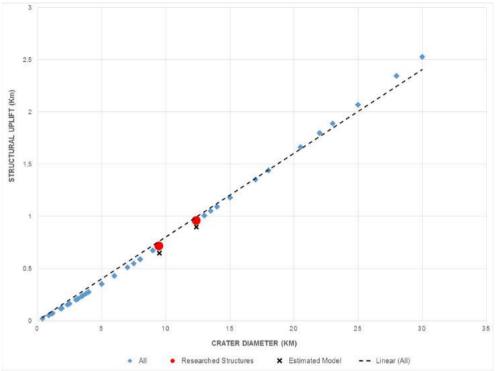
Figure 17 – Structural uplift (SU) vs. crater diameter of 49 impact structures extracted from Pilkington & Grieve (1992) and their fitted linear trend. Red dots indicate SU theoretical values for Vargeão and Vista Alegre impact structures. Black crosses represent SU values estimated from the 3D models for the same structures.

and not in Vista Alegre. This layer, known as Acidic Chapecó, comprises rhyodacite and rhyolite flows found at on top of the rim of Vargeão (Kazzuo-Vieira et al., 2009; Ferreira et al., 2015). The gravity signatures in both Vargeão and Vista Alegre structures show a negative anomaly in the innermost area surrounded by a ring-shaped positive anomaly. The amplitudes of the two positive anomalies are distinct and they can be directly associated with the respective diameters of the structures (Pilkington & Grieve, 1992). In Figure 15 we compare their E-W profiles with respect to the amplitude of their anomalies and their respective limits. The central uplift diameter of Vargeão is ∼5 km whereas that of Vista Alegre is ∼3.0 km, and the Vargeão anomaly is ∼0.5 mGal higher than that of Vista Alegre.

The central uplift regions of Vargeão and Vista Alegre were estimated from an extracted portion of the density model (Fig. 16). By comparing the two models, we noticed that the Botucatu/Piramboia Formations present two important differences, as follows: (1) The deformation caused by the impact in Vargeão astroblem reaches the pre-Triassic layers (Fig. 16A), whereas in Vista Alegre, it is limited by the Triassic (Botucatu/Piramboia) sandstone layer (Fig. 16B); (2)

Large sandstone outcrops occur from the Botucatu/Piramboia Formations on the surface of the central uplift of Vargeão. In Vista Alegre, the uplifting has exposed only the top of Triassic Sandstones of the Botucatu/Piramboia Formations, resulting in the exposure of small blocks of sandstones as floats immersed in basalt-derived red soils.

Figure 17 presents the structural uplift (SU) vs. crater diameter for the same 49 structures previously selected from the (Pilkington & Grieve, 1992) database, plus values for Vargeão and Vista Alegre. The estimated SU from our models are in agreement with the known empirical relation established in Grieve et al. (1981).

CONCLUSION

This work contributes to a better understanding of subsurface deformation undergone by target rocks due to meteoritic impacts that formed Vargeão and Vista Alegre structures. In this Part II, we propose a 3D density model for the Vista Alegre structure obtained from the inversion of Bouguer anomalies, which is consistent with the available geological and petrophysical information. The model depicts 3D geological structures and
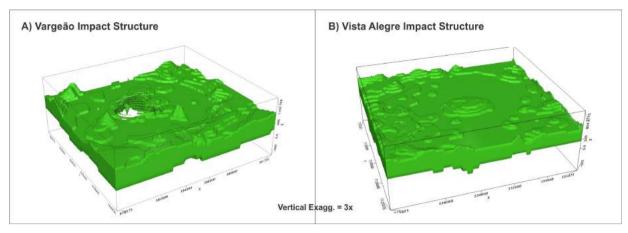
Figure 18 – 3D models of the Serra Geral Formation layer. (A) Vargeão; (B) Vista Alegre. Vertical exaggeration is 3x.

morphologies that would be expected for a complex impact structure. From 2D sections extracted from the model, a diameter of ∼9.5 km was inferred, which is consistent with a value calculated using a classical empirical model and to previous morpho-structural interpretations based on remote sensing data (Furuie, 2006). The model also indicates the presence of an uplifted sedimentary layer underneath the basalts, at the center of the structure, which we interpret as the sandstone strata of the Piramboia/Botucatu Formations. This uplift has the shape of an elliptic cone with axis lengths of 3.5 km and 2.5 km. The stratigraphic uplift was estimated to ∼650 m, a value that is near to the one calculated by the empirical model from Grieve et al. (1981). The similarity between Vargeão and Vista Alegre models can be explained by the occurrence of these two impact events on the same geological target along with the similar bolide diameters (∼1.25 km and ∼1 km for Vargeão and Vista Alegre, respectively). The fact that the Piramboia/Botucatu sandstones are better exposed in Vargeão when compared to Vista Alegre, despite the fact that the thickness of the Serra Geral volcanics is similar in both sites, can be explained by the larger diameter of Vargeão. The latter is seemingly the result of a larger impactor than the one that formed Vista Alegre.

REFERENCES

CRÓSTA A. 2012. Estruturas de impacto e astroblemas brasileiros. In: HASUI Y, CARNEIRO CDR, ALMEIDA FFM & BARTORELLI A (Eds.). Geologia do Brasil. São Paulo, Brazil: Ed. Beca-Ball, p. 673–708.

CRÓSTA A, KAZZUO CV & SCHRANK A. 2004. Vista Alegre: a newly discovered impact crater in Southern Brazil. Meteoritics & Planetary Science, 39(Suppl.). In: 67th Annual Meeting of the Meteoritical Society. Rio de Janeiro, Brazil. Abstract n. 5051.

CRÓSTA AP, KOEBERL C, FURUIE RA & KAZZUO CV. 2010. The first description and confirmation of the Vista Alegre impact structure in the Paraná flood basalts of southern Brazil. Meteoritics & Planetary Science, 45(2): 181–194.

CRÓSTA A, FURUIE R, SCHRANK A & VIEIRA CK. 2013. Astroblema de Vista Alegre, PR. Impacto meteorítico em derrames vulcânicos da Formação Serra Geral, Bacia do Paraná. In: WINGE M, SCHOBBENHAUS C, SOUZA CRG, FERNANDES ACS, BERBERT-BORN M, SALLUN FILHO W & QUEIROZ ET (Eds.). Sítios Geológicos e Paleontológicos do Brasil. SIGEP 044, Brasília. CPRM, 3: 23-36.

FERREIRA JC, LEITE EP, VASCONCELOS MAR & CRÓSTA AP. 2015. 3D Gravity Modeling of Impact Structures in Basaltic Formations in Brazil: Part I – Vargeão, Santa Catarina. Brazilian Journal of Geophysics, 33(2): 319–332.

FERREIRA JC. 2017. Modelagem gravimétrica 3D das estruturas de impacto de Vargeão-SC e Vista Alegre-PR. Master dissertation. Universidade Estadual de Campinas, SP, Brazil. 171 pp.

FURUIE RA. 2006. Aspectos Geológicos e Feições de Impacto da Cratera de Vista Alegre, PR. Undergraduate dissertation. Universidade Estadual de Campinas. São Paulo, Brazil. 102 pp.

GRIEVE R, ROBERTSON P & DENCE M. 1981. Constraints on the formation of ring impact structures, based on terrestrial data. In: SCHULTZ PH & MERRILL RB (Eds.). Multi-ring basins: Formation and Evolution. Proceedings of the Lunar and Planetary Science Conference. Houston, TX. Pergamon Press. p. 37-57.

GRIEVE RA. 1987. Terrestrial impact structures. Annual Review of Earth and Planetary Sciences, 15(1): 245–270.

KAZZUO-VIEIRA C, CRÓSTA AP, GAMBOA F & TYGEL M. 2009. Caracterização geofísica da estrutura de impacto do Domo de Vargeão, Brasil. Brazilian Journal of Geophysics, 27(3): 375–388.

MILANI EJ, FACCINI UF, SCHERER C, ARAÚJO LMD & CUPERTINO JA. 1998. Sequences and stratigraphic hierarchy of the Paraná Basin (Ordovician to Cretaceous), southern Brazil. Boletim IG-USP, 29: 125-173.

PILKINGTON M & GRIEVE R. 1992. The Geophysical Signature of Terrestrial Impact Craters. Reviews of Geophysics, 30: 161-181. doi: 10.1029/92RG00192.

POPOWSKI T, CONNARD G & FRENCH R. 2006. GMSYS-3D: 3D Gravity and Magnetic Modeling for Oasis Montaj - User Guide. Corvallis, Oregon.

THERRIAULT AM, GRIEVE RAF & REIMOLD WU. 1997. Original size of the Vredefort Structure: Implications for the geological evolution of the Witwatersrand Basin. Meteoritics & Planetary Science, 32(1): 71-77.

TURNER S, REGELOUS M, KELLEY S, HAWKESWORTH C & MANTOVANI M. 1994. Magmatism and continental break-up in the South Atlantic: High precision ^{40}Ar-^{39}Ar geochronology. Earth and Planetary Science Letters, 121: 333-348.

YOKOYAMA E. 2013. Petrologia e Magnetismo de Estruturas de Impacto da Bacia do Paraná: Reflexões sobre o Processo de Crateramento. Ph.D. thesis. Universidade de São Paulo, Instituto de Astronomia, Geofísica e Ciências Atmosféricas. São Paulo, Brazil. 259 pp.

REDUCTION IN WATER LEVELS AND REGIONAL WARMING OF THE AMAZON RIVER FROM PERU TO THE ATLANTIC OCEAN IN BRAZIL DUE TO THE EFFECTS OF THE 2016 ENSO

Newton Silva de Lima[1], Aldemir Malveira de Oliveira[2], Eriberto Barroso Façanha Filho[1],
José Olavo Nogueira Braga[1], Ricardo Silva Figueiredo[1], Robson Matos Calazães[1], William Dennis Quispe[1],
Roseilson Souza do Vale[3] and Alan dos Santos Ferreira[1]

ABSTRACT. *In situ* observations of the tendencies of the ENSO (El Niño Southern Oscillation) phenomenon combined with a trend of regional warming in both western and eastern Amazônia were registered by the Amazon River Peru-Brazil Expedition on the Amazon River. Temperatures were taken at four positions on the river (edge, middle of the canal, 1 m deep below the surface, and ambient air), air pressure and humidity, and the velocity and direction of the wind were the parameters that were sampled from the Peruvian city of Iquitos beginning in July 2016, to the Brazilian city of Macapá at the mouth of the Amazon River ending in December 2016. The results suggest that there was a decline in water levels along the river during the entire observation period due to the El Niño event that occurred in 2014, 15 and 16.

Keywords: Amazônia, El Niño, Iquitos, hydroclimate.

RESUMO. Observações *in situ* das tendências do fenômeno ENOS (El Niño Oscilação Sul) combinadas com uma tendência de aquecimento regional na Amazônia ocidental e oriental foram registradas pela Expedição Rio Amazonas Peru-Brasil no Rio Amazonas. As temperaturas foram registradas em quatro posições no rio (borda, meio do canal, 1 m abaixo da superfície e ar ambiente), pressão do ar e umidade, e a velocidade e direção do vento foram os parâmetros amostrados desde a cidade peruana de Iquitos em julho de 2016, a cidade brasileira de Macapá na foz do Rio Amazonas em dezembro de 2016. Os resultados sugerem que houve um declínio nos níveis de água ao longo do rio durante todo o período de observação devido ao evento El Niño que ocorreu em 2014, 2015 e 2016.

Palavras-chave: Amazônia, El Niño, Iquitos, hidroclima.

[1]Universidade Luterana do Brasil – Campus Manaus, Manaus, AM, Brazil – E-mails: newtonulbra@gmail.com, eribertofacanha@seduc.net, olavonbraga@yahoo.com.br, rics.fig@gmail.com, matoscalazaes@gmail.com, william.exner@bol.com.br, alans_ferreira@hotmail.com
[2]Universidade Federal do Amazonas, Matemática, Manaus, AM, Brazil – E-mail: amoliveira@gmail.com
[3]Universidade Federal do Oeste do Pará, Geociências, Santarém, PA, Brazil – E-mail: roseilsondovale@gmail.com

INTRODUCTION

Changes in atmospheric circulation in the tropical zone (Walker cell) induce change in rainfall patterns, devastating floods, and severe droughts that can drastically affect the lives of millions of people (Mohtadi et al., 2017). In the mosaic of landscapes that is tropical South America the tendencies for rainfall, in the Amazon in eastern Brazil, to the northwest of Peru are well-defined by long-term hydrological data for the Amazon basin that were recorded during the 20th century.

During this period the tendency for rainfall during the three most humid months and for the subsequent superficial runoff rate during the three months with the greatest runoff for the northeastern region of Brazil demonstrated a slow increase over long periods (Marengo et al., 1998). In 2016 the Amazon River Expedition from Peru to Brazil observed tendencies in which a prolonged ENSO event combined with a trend of regional warming increased the demand for water from the reservoirs of Brazilian hydroelectric plants in the Northeast, Central-West, and Southeastern regions of Brazil (CCEE, 2017), and caused strong rains in the Southern region of Brazil (CPTEC, 2016).

According to Jiménez-Muñoz et al. (2016), this event was associated with warming that was without precedent and an extreme drought in the Amazon, compared to other strong ENSO events in 1982/83 and 1997/98. The typical conditions of drought caused by the ENSO were observed and described by Jiménez-Muñoz et al. (2016), as occurring only in the eastern Amazon, while in the western region of the Amazon there prevailed an uncommon level of humidity. For researchers this situation can be attributed to the humid-dry dipole at the location of maximum warming of the surface of the equatorial central Pacific Ocean. This humid-dry dipole was also confirmed in the current study through a time series of temperature readings at 4 distinct points (edge, middle of the canal, 1 m deep below the surface, and ambient air) along the Amazon River from the west in Iquitos, Peru, to the east in Macapá, Brazil by the research team of the Amazon River Expedition from Peru to Brazil in 2016. According to Erfanian et al. (2017), the empirical relationships between rainfall and sea surface temperatures (SST) in the Pacific and Atlantic Oceans represent the factors of tropical ocean variability responsible for the observed precipitation anomalies. These results indicate that the warmer than normal SST for the tropical Pacific and Atlantic Oceans (including El Niño events) were the principal causes of extreme droughts in South America, however, researchers are still unable to explain the severity of the precipitation deficits observed in 2016 in a substantial portion of the Amazon region. Therefore, hydroclimatic variability in South America is strongly coupled, on a large scale, to oceanic and atmospheric phenomena. Specifically, the El Niño Southern Oscillation (ENSO) that affects climatological and hydrological conditions has a "terrestrial – atmospheric" mechanism that forms a bridge between these two domains and connects the anomalies of SST of the Pacific and Atlantic Oceans (Poveda & Mesa, 1997).
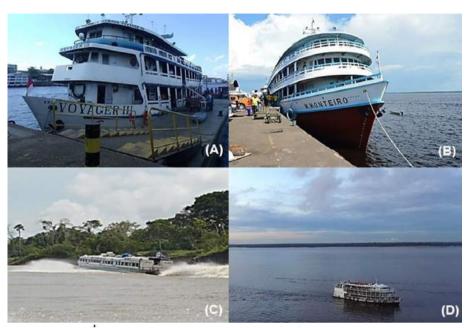
The variability of winds that favored the formation of the El Niño Southern Oscillation (ENSO) between 2014 and 2016 and their possible contribution to drought and hydrological stress of the Amazon River were mentioned in the commentaries of Zhu et al. (2016) on reliable predictions of ENSO. These inferred predictions are strongly dependent on correct modeling of the meridional Sea Surface Temperature (SST) gradient as well as its delicate feedback with the zonal ENSO mode. In Ineson et al. (2018) the western equatorial Pacific Ocean surface temperature anomalies don't seem to impede the development of the El Niño, although the strong activity of the western wind in 2015, compared to 2014, is a fundamental difference between the two years, and this was also noted by Hu & Fedorov (2018). When the causes of these changes are analyzed over the last two decades the average SST anomalies are weakened towards the west, in direction of the central Pacific, and this represents an indicator that needs more observation.

MATERIAL AND METHODS

An automatic meteorological station was installed on roof of the five passenger transport ships (Fig. 1) used in this research expedition (Fig. 2). The station was free from obstacles that would impede accurate measurement of the variables of interest (temperature, humidity, pressure, wind speed and direction, dew point, and rainfall).

Sampling and chronogram

For monitoring of weather and climate during the period of the research were used: I - FLIR-E60 thermal imager (Table 3) and II – Mira digital thermometer – LASER, Minipa MT-360 sensors. Measurement of ambient air temperature, and the temperature at the edge of the river, middle of the canal, and at 1.0 m below the river's surface a meteorological station with uninterrupted recording (15 days + 15 days) with data collection (ambient air temperature, humidity, pressure, wind speed and direction, dew point) were measured every 5 minutes, and *in situ* two liter water samples were taken at each sampling point along the entire
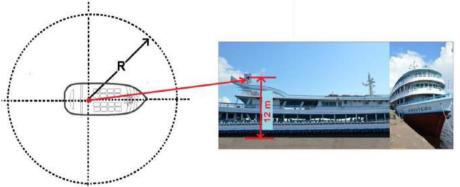
Figure 1 – Ships used in the Amazon River Expedition (2016-18).

Figure 2 – Map of the Expedition (Arequipa-Peru; Iquitos-Peru; Macapá-Brazil).

river. Temperature values are a composite of 10 *in situ* readings taken at each sampling point. The geographic coordinates of the sampling points were taken along with a description of the weather (climate) and the time at the moment of collection, and samples were labeled accordingly (Steps 1 and 2 of the Amazon River Expedition protocol).

Laboratory analysis of water samples (and methods)

1. Alkalinity (APHA, 2003; Palissa, 1972);

2. Calcium ($Ca_2{}^+$), hardness, and Magnesium ($Mg_2{}^+$) (APHA, 1985; Golterman et al., 1978);

3. Chlorides (FENANTHROLINE – FIA), (Mackereth et al., 1978; Golterman, 1971);

4. DQO with potassium dichromate (APHA, 2003; Mackereth et al., 1978);

5. Total and Dissolved iron (FIA) (APHA, 2003);

6. Phosphate (PO_4) (APHA, 2003; Palissa, 1972);

7. Total phosphorus and nitrogen (N and P-TOTAL) (Valderrama, 1981);

8. Total phosphorus (FIASTAR) (APHA, 2003; ISO 5861, s/d);

9. Nitrate (FIA) (Golterman et al., 1971);

10. Ammoniacal nitrogen (NH_3) (FIA - Flow Injection Analysis) Nessler reagent method;

11. Silicates (Silica – Molybdenum blue method) (Golterman et al., 1978; Mackereth et al., 1978);

12. pH (hydrogen ion concentration) (APHA, 2003);

13. Potassium and sodium by flame emission spectroscopy (Mackereth et al. 1978);

14. Total suspended solids (STS) (APHA, 2003);

15. Sulfate (APHA, 2003);

16. Temperature (FLIR-E60 thermal imager);

17. Turbidity (turbidity meter);

18. Color (spectrophotometer).

Done only between Manaus (Brazil) and Macapá (Brazil).

Statistical modeling and georeferencing of data

The time series of temperature reading along the Amazon River were processed and analyzed using the *Marine Modeling and Analysis Branch Oper H.R.* (Verification ensemble) of NOAA/NWS/NCEP/EMC (ftp://ftpprd.ncep.noaa.gov/pub/data/nccf/com/gfs/prod). For the characterization of the composition of the El Niño event during this period the temperature gradients of the SST of the equatorial Atlantic and the eastern equatorial Pacific were constructed. All sampling points were georeferenced using a GPS (GARMIN – E60 and the software TrackMaker®), and the creation of a thematic map for sampling points was done using ArcGIS®. Flux measurements (temperature, humidity, pressure, wind speed and direction) were taken using a meteorological station (Vantage Vue/DAVIS Instruments Corporation, WeatherLink 6.0.3), using the static method (Lima et al., 2017), for covariances (*Eddy Covariance*).

RESULTS AND DISCUSSION

The decrease in the water level of the Amazon River between 2014 – 2016 was observed through the use of meteorological and hydrological stations of National Water Agency of Brazil (ANA - Agência Nacional de Águas) in 2013, 2014, 2015 and 2016, with hydrological data coming from the Hydrometeorological Network which is operated by the Geological Service of Brazil, and also from the COLA - Center for Ocean-Land-Atmosphere Studies/Virginia-USA (http://wxmaps.org/pix/clim). Figure 3 shows these data in the form of periods of flooding and low water (Tables 2 and 3) in the periods of high water on the upper Solimões (Amazon River) at Tabatinga-AM/Brazil (No. 10100000), the frontier between Brazil-Colombia-Peru, at the Itapeuá station (No. 131500000), at the middle Solimões at Tapauá-AM/Brazil, and also at Manacapuru-AM/Brazil (No. 14100000), above the city of Manaus/Brazil. This control has a strong degree of significance and ends at Óbidos-PA/Brazil, with the cities of Itacoatiara-AM/Brazil and Parintins-AM/Brazil between Manaus and Óbidos. The station at Careiro-AM/Brazil (No. 15040000) below Manaus demonstrates the reduction in the Rio Negro which bathes the city.

Figure 3 shows prediction of COLA (Center for Ocean-Land-Atmosphere Studies) for hydrological monitoring during 2014-2015-2016 by ANA (National Water Agency). For the month of January 2014, the forecast for rainfall over the Amazon indicated areas of concentration of rainfall with significant accumulation in the States of Rondônia, the west of

Table 1 – Additionally, *in situ* analyses of pH, O$_2$, conductivity, and O$_2$ saturation were conducted on all water samples.

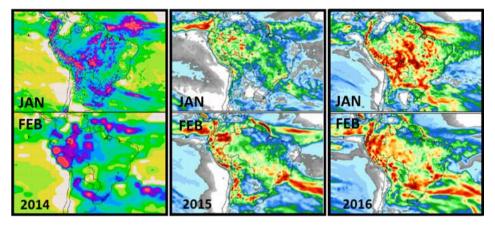| MATERIAL	SPECIFICATION	TEMP.(°C)	ELECTROMAGNETIC SPECTRUM	EMISSIVITY
WATER	LAYER THICKNESS > 0.1mm	0-100	ALL	0.95-0.98

Figure 3 – Panel of maps of the Amazon showing climatological prognostics for rainfall prediction during January through February for 2014-2015-2016. (Source: http://wxmaps.org/pix/clim - COLA/Virginia-USA).

Mato Grosso, the southeast of Amazonas and generalized rainfall over Pará. During January and February 2014 the forecast for rainfall indicated more significant accumulation over Amazonas, Acre and Rondônia. In January 2015 a frontal system occurred over the southeast of Brazil. The highest rainfall accumulation was in the Upper Solimões basin and along its principal tributaries such as the Japurá, Juruá and Purus Rivers, the West and southwest of Amazonas, the State of Acre, the north of Rondônia, and the west of Mato Grosso. In Solimões, during January and February 2015, the forecast indicated the possibility of maintenance of the rainfall pattern of the previous week with significant accumulations of rainfall concentrated in Bolivia, Peru and Colombia, and also over the basin in Brazil in the western regions of Amazonas, Acre and Rondônia. Finally, in January 2016 there were significant volumes of rainfall over a large part of the legal Amazon. These accumulations were associated with the influence of the Intertropical Convergence Zone (ITCZ) and also with the passage of frontal systems that contributed to the formation of areas of instability which organized or fortified the Humidity Convergence Zone (HCZ) or the South Atlantic Convergence Zone (SACZ). The forecast for rainfall for February 2016 indicated more significant accumulation concentrated in an area running from the northwest to the southeast over the

Colombia and Peru, passing through the central-west of Brazil in the direction of the Atlantic Ocean.

Figure 4 shows systems that were responsible for the atmosphere dynamics on July 26, 2016 between 05:00 LT and 17:00 LT, the first day of the Amazon River Expedition when it left Iquitos, Peru, for Manaus, Brazil. The Intertropical Convergence Zone (ITCZ) is in the north of South America and reaches the Amazon region, and there is a cold front that is developing in the southern Atlantic Ocean and is penetrating the southern region of Brazil.

The reduction in hydrological and water quality characteristics of the Amazon River between 2014 and 2016 (Tables 2 and 3, ANA) were registered (Tables 3 and 4) by the Amazon River Expedition during the ENSO, and these climatological observations showed little movement of the Intertropical Convergence Zone (ITCZ) towards the southern hemisphere (Figs. 4 and 5). This is a consequence supposedly caused by the weakening of the winds, and this question remains open for many researchers, including Ashok et al. (2007), Kao & Yu (2009), Kug et al. (2009), McPhaden et al. (2011), and Hu & Fedorov (2018), all of whom affirm that the changes in these winds, which are considered to be natural forcings for the El Niño, is still cause for debate, and that the occurrence of
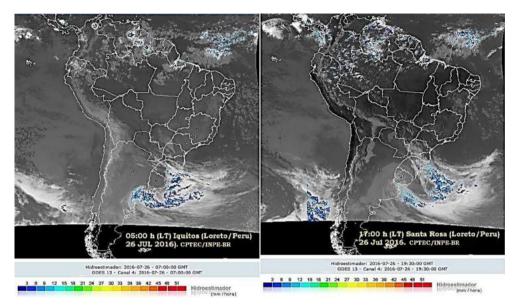
Figure 4 – Meteorological conditions on July 26, 2016, between 05:00 LT and 17:00 LT for South America. (Source: CPTEC/INPE, 2016).

Table 2 – Water levels at the hydrological monitoring stations during floods between 2013 and 2016 for the Amazon River (Solimões from Tabatinga to Manaus). Source: ANA/CPRM/SIPAM, 2016.

STATION	RIVER	MAXIMUM WATER LEVEL		RELATION WITH MAXIMUM WATER LEVEL (cm)	MOST RECENT INFORMATION	
		YEAR	WATER LEVEL (cm)		DATE	LEVEL (cm)
TABATINGA	SOLIMÕES	1999	1382	-648	11/29/2013	734
ITAPEUÁ	SOLIMÕES	2012	1765	-823	11/27/2013	942
MANACAPURU	SOLIMÕES	2012	2068	-937	11/27/2013	1131
TABATINGA	SOLIMÕES	1999	1382	-352	01/23/2014	1030
ITAPEUÁ	SOLIMÕES	2012	1765	-598	01/23/2014	1167
MANACAPURU	SOLIMÕES	2012	2068	-690	01/23/2014	1378
TABATINGA	SOLIMÕES	1999	1382	-299	01/22/2014	1083
ITAPEUÁ	SOLIMÕES	2012	1765	-491	01/22/2015	1274
MANACAPURU	SOLIMÕES	2012	2068	-712	01/15/2015	1356
FONTE BOA	SOLIMÕES	1999	2224	-304	01/22/2015	1920
CAREIRO	SOLIMÕES	2012	1743	-686	01/22/2015	1057
TABATINGA	SOLIMÕES	1999	1382	-708	01/29/2016	674
ITAPEUÁ	SOLIMÕES	2015	1801	-757	01/28/2016	1044
MANACAPURU	SOLIMÕES	2015	2078	-928	01/28/2016	1152
FONTE BOA	SOLIMÕES	2015	2282	-561	01/29/2016	1721
CAREIRO	SOLIMÕES	2012	1743	-955	01/28/2016	788

effects associated with these forcings are also open to debate and probably will be for quite some time.

Figure 5 shows a graphical rhythmic analysis of weather types between Iquitos (Loreto-Peru), Tabatinga and São Paulo de Oliveira (State of Amazonas-Brazil) on July 26, 2016, between

05:00 LT and 18:00 LT in Peru, and July 27, 2016 (09:00 LT to 05:00 LT in Brazil), in which the climatic elements involved in this analysis of atmosphere dynamics are evident (CPTEC/INPE).

Figure 6 shows the time series of temperature that was taken at three positions (ambient temperature at the ship – 100

Table 3 – Water levels at the hydrological monitoring stations during low-water between 2013 and 2016 for the Amazon River (Solimões from Tabatinga to Manaus). Source: ANA/CPRM/SIPAM, 2016.
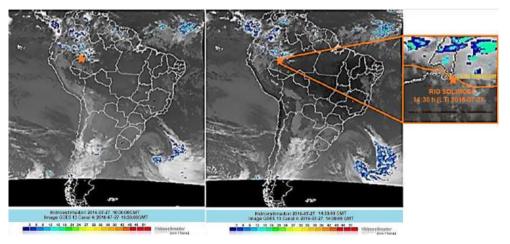
STATION	RIVER	MAXIMUM WATER LEVEL		RELATION WITH MAXIMUM WATER LEVEL (cm)	MOST RECENT INFORMATION	
		YEAR	WATER LEVEL (cm)		DATE	LEVEL (cm)
TABATINGA	SOLIMÕES	2010	-86	820	11/29/2013	734
ITAPEUÁ	SOLIMÕES	2010	131	811	11/27/2013	942
MANACAPURU	SOLIMÕES	1997	495	636	11/27/2013	1131
TABATINGA	SOLIMÕES	2010	-86	1116	01/23/2014	1030
ITAPEUÁ	SOLIMÕES	2010	131	1036	01/23/2014	1167
MANACAPURU	SOLIMÕES	1997	495	883	01/22/2014	1378
TABATINGA	SOLIMÕES	2010	-86	1169	01/22/2015	1083
ITAPEUÁ	SOLIMÕES	2010	131	1143	01/22/2015	1274
MANACAPURU	SOLIMÕES	1997	495	851	01/15/2015	1356
FONTE BOA	SOLIMÕES	2010	802	1118	01/22/2015	1920
CAREIRO	SOLIMÕES	2010	125	932	01/22/2015	1057
TABATINGA	SOLIMÕES	2010	-86	760	01/29/2016	674
ITAPEUÁ	SOLIMÕES	2010	131	913	01/28/2016	1044
MANACAPURU	SOLIMÕES	1997	495	657	01/28/2016	1152
FONTE BOA	SOLIMÕES	2010	802	919	01/29/2016	1721
CAREIRO	SOLIMÕES	2010	125	653	01/28/2016	788

Figure 5 – Meteorological conditions on July 27, 2016, between 10:30 and 14:30 GMT, for South America. (Source: CPTEC/INPE, 2016).

m from the edge of the canal – middle of the canal) during the 1st stage of the expedition (Iquitos/Peru – Manaus/Brazil), using the FLIR-E60 thermal imager. The image next to the time series shows SST in Real Time Global (RTG), High Resolution (HR) and was obtained by NOAA/NCEP/NWS/EMC (2017) by analyzing satellite images, ocean floats, sea ice cover, salinity, and conducting mathematical modeling in a second degree polynomial series (Branch analysis method), (ftp://ftpprd.ncep.noaa.gov/pub/data/

nccf/com/gfs/prod), and indicates correlation with the results obtained by the Amazon River Expedition.

The observations from this study suggest regional warming of temperature gradients in the stretch between Iquitos-Peru to Manaus-Brazil) in July 2016 (dry season), with average ambient temperature at the ship (in the shade) of 30.41°C, at the river's surface (100 m from the edge) of 27.34°C, and at the middle of the canal of 24.73°C (Fig. 6). During the 2nd stage of the

Table 4 – Water sample analysis – Stage one of the Amazon River Expedition (Peru-Brazil), July 2016.

Samples	Geographic Coordinates		Water	Temp.	Conductivity	Alkalinity	Dissolved Oxygen		Turbidity
	Longitude (S)	Latitude (W)	pH	°C	(μS/cm)	(mgHCO₃/L)	%	mg/L	(NTU)
1	S 03° 43' 37.6"	W 073° 14' 23.8"	6.61	28.8	48.30	22.57	113.50	9.50	15.60
2	S 03° 48' 18.8"	W 071° 34'25.4"	7.31	26.0	112.00	51.24	117.60	10.02	104.00
3	S 04° 00' 59.6"	W 071° 06' 07.5"	7.29	26.0	123.70	48.19	105.70	8.46	83.72
4	S 03° 55' 40.8"	W 070° 47' 10.4"	7.22	25.0	119.90	46.36	103.70	8.27	53.56
5	S 03° 53' 49.0"	W 070° 30' 19.1"	7.79	26.0	117.40	47.58	111.80	8.81	50.18
6	S 04° 06' 39.7"	W 070° 03' 13.8"	6.92	29.0	78.10	36.60	108.10	9.31	8.84
7	S 04° 13' 04.7"	W 069° 57' 19.1"	6.89	27.0	106.50	48.19	108.00	8.56	79.56
8	S 04° 13' 44.4"	W 069° 56' 41.0"	7.20	27.0	103.70	44.53	109.20	9.44	75.40
9	S 04° 22' 19.5"	W 070° 01' 34.3"	7.15	26.0	104.30	47.58	110.20	8.36	73.06
10	S 04° 18' 31.2"	W 069° 33' 27.5"	6.60	24.0	28.30	13.42	115.80	9.29	41.08
11	S 03° 27' 42.2"	W 068° 57' 26.4"	7.17	24.0	100.30	42.09	124.00	9.85	83.98
12	S 03° 21' 14.5"	W 068° 11' 04.2"	7.00	24.0	98.10	43.31	113.20	9.75	82.42
13	S 03° 06' 29.1"	W 067° 56' 39.6"	5.81	23.0	9.51	4.27	99.80	9.71	6.24
14	S 02° 51' 47.0"	W 067° 46' 13.4"	6.15	26.0	17.45	9.15	117.50	9.61	21.06
15	S 02° 44' 33.8"	W 066° 46' 19.5"	6.16	25.0	17.92	9.76	109.00	8.99	10.92
16	S 02 ° 29' 40.6"	W 066° 04' 05.1"	7.00	25.5	75.00	32.33	119.50	9.48	54.60
17	S 03° 16' 32.1"	W 064° 43' 12.1"	6.87	25.5	68.50	29.89	118.90	9.92	63.44
18	S 03° 47' 18.3"	W 064° 02' 19.8"	6.93	27.0	69.30	31.72	108.30	9.07	42.12
19	S 04° 03' 17.1"	W 063° 04' 54.0"	6.89	26.0	64.20	30.50	110.00	9.42	44.20
20	S 03° 47' 17.2"	W 061° 37' 05.8"	6.76	25.0	54.40	25.01	100.70	8.34	29.38
21	S 03° 33' 34.6"	W 060° 53' 16.0"	6.75	24.5	50.70	23.79	103.80	7.79	44.46
22	S 03° 28' 34.8"	W 060° 45' 22.9"	6.76	26.0	48.10	22.57	119.10	9.00	20.80
23	S 03° 19' 17.3"	W 060° 37' 00.6"	6.81	23.0	48.50	22.57	129.70	10.45	29.38
24	S 03° 19' 17.3"	W 060° 37' 00.6"	6.77	27.0	48.60	22.57	108.50	9.11	24.44
25	S 03° 08' 11.1"	W 059° 53' 59.1"	5.53	28.0	9.00	3.66	114.80	9.61	3.64

Table 5 – Water sample analysis – Stage two of the Amazon River Expedition (Peru-Brazil), December 2016.

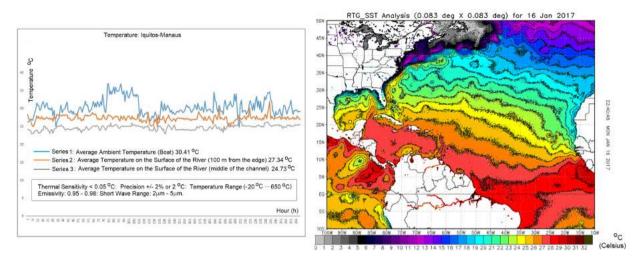| Samples	Geographic Coordinates		Water	Temp.	Conductivity	Oxygen	Saturation of Oxygen	Alkalinity	Turbidity
	Longitude (N-S)	Latitude (W)	pH	°C	(μS/cm)	mg/L	%	(mgHCO₃/L)	(NTU)
1	S 03° 08' 21.3"	W 060° 01' 35.1"	5.14	27.6	7.92	5.76	77.00	2.44	3.90
2	S 03° 08' 54.3"	W 058° 26' 54.1"	6.56	27.0	53.30	5.35	76.60	17.08	35.36
3	S 02° 38' 01.6"	W 056° 45' 21.7"	6.70	27.0	51.30	5.66	69.30	16.47	44.46
4	S 02° 09' 05.9"	W 056° 05' 43.1"	6.54	27.0	51.20	5.63	70.50	15.25	37.44
5	S 01° 55' 22.2"	W 055° 30' 55.3"	6.75	27.0	52.80	5.64	68.80	18.30	38.48
6	S 02° 24' 52.1"	W 054° 44' 13.8"	6.16	27.0	13.80	5.68	74.90	7.32	4.68
7	S 02° 25' 00"	W 054° 43' 22.2"	6.07	27.0	13.92	6.36	82.50	6.10	2.60
8	S 02° 00' 35.1"	W 054° 04' 10.0"	6.54	27.0	45.70	5.29	67.20	16.47	57.46
9	S 02° 00' 35.3"	W 054° 04' 11.8"	6.41	26.6	50.00	4.98	64.05	17.69	41.34
10	S 01° 31' 58.7"	W 052° 34' 34.5"	6.45	28.0	47.50	5.28	71.20	21.96	33.28
11	S 00° 03' 27.4"	W 051° 10' 42.1"	6.50	27.0	53.10	4.70	58.40	23.18	27.56
12	N 00° 01' 37.4"	W 051° 02' 55.1"	6.60	26.3	53.30	5.96	71.90	22.57	27.56
13	N 00° 02' 00.2"	W 051° 02' 43.1"	6.44	27.0	56.50	5.37	67.70	25.01	27.30
14	S 00° 31' 20.0"	W 051° 29' 59.7"	6.81	26.6	45.90	4.94	65.30	21.35	36.92
15	S 00° 32' 38.9"	W 051° 31' 47.7"	6.84	27.0	46.40	4.00	67.30	21.96	36.48

Figure 6 – Time series of temperature along the Amazon River during the first stage of the Expedition (Iquitos/Peru–Manaus/Brazil), and compared to data from the Marine Modeling and Analysis Branch Oper H.R. (Verification Ensembles) of NOAA/NWS/NCEP/EMC. Source: Amazon River Expedition and NOAA, 2016.
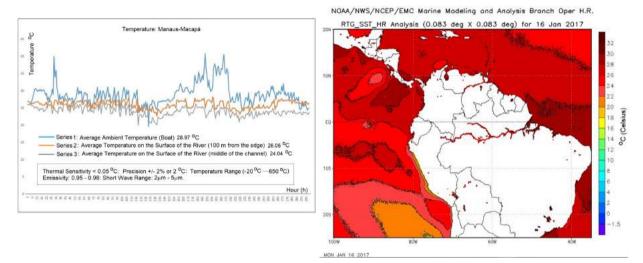

Figure 7 – Time series of temperature along the Amazon River during the second stage of the Expedition (Manaus/Brazil – Macapá/Brazil), and compared to data from the Marine Modeling and Analysis Branch Oper H.R. (Verification Ensembles) of NOAA/NWS/NCEP/EMC. Source: Amazon River Expedition and NOAA, 2016.

Expedition (Manaus-Brazil to Macapá-Brazil) in December 2016, the rainy season had already begun and average temperatures were slightly reduced, with average ambient temperature at the ship of 28.97°C, at the river's surface (100 m from the edge) of 26.06°C, and at the middle of the canal of 24.04°C. The interval between the first and second stages was taken in order to be able to verify the effect of drought on the river due to the time necessary for water to flow across the large distance from Iquitos-Peru to Macapá-Brazil (Fig. 7). The margin of error is shown in Figures 6 and 7 and in Table 1.

The time series of temperature was taken at three positions (ambient temperature at the ship – 100 m from the edge of the canal – middle of the canal) during the 2nd stage of the Expedition (Manaus-Brazil to Macapá-Brazil) in December 2016 using the FLIR-E60 thermal imager. The image next to the time series shows SST in Real Time Global (RTG), High Resolution (HR) and was obtained by NOAA/NCEP/NWS/EMC (2017) and indicates correlation with the results obtained by the Amazon River Expedition (Fig. 7).

The analyses of the water samples from both stages of the expedition are listed in Tables 4 (1st stage) and 5 (2nd stage), and these data describe the "actual state" of the Amazon River in 2016 during the dry season in the Amazon. In Tabatinga at the entry of the Amazon River into Brazil, during the month of

July 2016, the level of the Solimões River (the name given to the river from this point to Manaus, Brazil) was 5.54 m (at the end of the rainy season it was 11.62 m at this sampling point in May 2016), and the highest level recorded here was in May 1999 when the depth was 13.38 m with respect to sea level (ANA/CPRM/SIPAM, 2016). During this period of the expedition the El Niño climate phenomenon was already firmly established in the region since it had begun in 2014, lasted for all of 2015, and was still strong in 2016. The effects of this drought were clearly visible during the entire voyage along the river from Peru to the Atlantic, principally due to the marks left on trees in the lowland areas at the river's edge by the previous high-water season. However, the quality of the water from the Amazon River at the 39 georeferenced sample points (Tables 4 and 5) was satisfactory and within the standard for potable water for human consumption by communities adjacent to the river's edge from the western portion of the basin to the Atlantic, although basic sanitation services are a preoccupation for all the communities located at these 39 sampling points, including for Iquitos (Peru), Manaus, Santarém and Macapá (Brazil).

At the end of December 2016, the Tapajós River in Santarém, Pará, Brazil, located in the lower Amazon region, was more than 6 m below the base of the contention dike that serves as a waterfront walkway for urban dwellers along the Tapajós' edge in front of the city. A vertical line near the pier in front of the church of Nossa Senhora da Conceição approximately 5 m above the base of this dike represented the maximum extent of the previous high-water mark, and this mark extended for more than 60 m horizontally to near the municipal fish market. Rainfall is still sporadic during this period of the year in Santarém and almost always occurs early in the first hours of the morning before sunrise or at the end of the afternoon but is always brief in duration.

Nearing the mouth of the Amazon River, the weather was constantly cloudy with grey and dark, low nimbostratus (Ns) clouds at about 2,000 to 3,000 m, with a constant fine rain near Prainha (Pará/Brazil) and Almeirim (Pará/Brazil), (08:20 LT), and the air temperature and the dew point temperature at the level of the river's surface were very similar, indicating a condition of saturation. There was fog on the horizon, and this fog goes by the name of hot fog because the drops are well above the freezing temperature. It was most likely an advective fog in function of the horizontal dynamic of atmospheric migration that was in a situation that was more adequate for saturation, since, being nearer to the Atlantic Ocean (approximately 300 km), the ocean breeze that penetrates the coast of Amapá at Macapá (Brazilian Atlantic coast), in this period of the year has favorable conditions for the trade winds, including for the ITCZ, that can stimulate the development of climatic variation in this region of the Amazon River.

RECOMMENDATION

At the website https://sites.google.com/view/amazonriverexpedition there is more information about the "actual state" of the Amazon River in 2016, not only with respect to climatology, but also with respect to the life of people in the communities in this region.

CONCLUSION

The Amazon River, during the dry season of 2016, was influenced by a prolonged El Niño climatic tendency (2014, 2015 and 2016). The results show that there was a reduction in water levels along the entire sampling trip on the river, from the city of Iquitos in Peru to the Brazilian city of Macapá near the interface of Brazil and the Atlantic Ocean. The sea surface temperature stimulated the establishment of an increasing temperature gradient in the equatorial region along the river, up to its mouth at the Atlantic Ocean, where the river accompanied the same temperature regime as the ocean during this period. This gradient established the climatic phenomenon called the wet-dry dipole, combined with a tendency for regional warming during the El Niño event of 2016.

However, it is important to note that the ITCZ, which normally migrates to the south from its northern position during an El Niño, has not crossed the equator since 1998 (Hu & Fedorov, 2018), and this for us is a strong indicator of the reduced quantity of rainfall over the Amazon. The improved determination of ENSO predictability, teleconnections, and impacts requires a better understanding of event-to-event differences in ENSO spatial patterns and evolution (Capotondi et al., 2015).

Mauá group at INPA in Manaus/Brazil. Furthermore, the authors thank the Secretary of Education and Quality of Teaching of the State of Amazonas, that through the DEPPE, provided logistical support in sampling areas in the State of Amazonas, Brazil, and the Environmental Engineering sector of Honda of the Amazon, the engineers Feijão, Mirian, Mário, and Murakami for physical support with material used in the field, and also the Consul of Peru in Manaus, Dr. Javier Arteta Valencia for his orientation, and the Consul of Brazil Dr. Salvador R. Vecchio in Iquitos for providing access to sites in Peru. Additionally, the authors thank the Institute of Investigation of the Peruvian Amazon (IIAP) in Iquitos, Peru, specificaly the Director Dr. Luis Campo Baca and his team, for the logistical support and the dissemination and promotion of this research expedition, the Superintendency of the Federal Police –Tabatinga-Amazonas/Brazil, the Migration and Foreign Visitor Service of Peru (Manaus, Santa Rosa and Iquitos), and the collaborators Eliomar Oliveira, Maurício Benzecry, Abrahão Barros, Gilberto Carvalho, and Francisco Santana.

REFERENCES

ANA/CPRM/SIPAM. 2016. Hydrological Monitoring. National Water Agency. Geological Service of Brazil. Protection System of the Amazon. Report card. # 18. Available on: <https://www.cprm.gov.br/sace/boletins/Amazonas/20160513_19-20160513%20-%20191650.pdf>. Access on: September 2, 2017.

APHA. 1985. Standard Methods for the examination of water and wastewater. American Public Health Association.

APHA. 2003. Standard Methods for the examination of water and wastewater. American Public Health Association.

ASHOK K, BEHERA S, RAO S, WENG H & YAMAGATA T. 2007. El Niño Modoki and its possible teleconnection. Journal of Geophysical Research, 112: C11007. doi: 10.1029/2006JC003798.

CAPOTONDI A, WITTENBERG AT, NEWMAN M, DI LORENZO E, YU JY, BRACONNOT P, COLE J, DEWITTE B, GIESE B, GUILYARDI E, JIN FF, KARNAUSKAS K, KIRTMAN B, LEE T, SCHNEIDER N, XUE Y & YEH SW. 2015. Understanding ENSO Diversity. Bulletin of the American Meteorological Society, 96(6): 921-938.

CCEE. 2017. Câmara de Comercialização de Energia Elétrica. Available on: <https::/economia.uol.com.br/noticias/Reuters/2017/09/20>. Access on: September 10, 2017.

CPTEC. 2016. DSA - Satellite Division and Environmental Systems. Centro de Previsão de Tempo e Estudos Climáticos - CPTEC/INPE. Available on: <http://satelite.cptec.inpe.br/home/index.jsp>. Access on: July/December, 2016.

ERFANIAN A, WANG G & FOMENKO L. 2017. Unprecedented drought over tropical South America in 2016: significantly under-predicted by tropical SST. Scientific Reports, 5811(2017). doi: 10.1038/s415998-017-05373-2.

GOLTERMAN HL, CLYMO RS & OHNSTAD MAM. 1978. Methods for Physical and Chemical Analysis of Fresh Waters. Volume 8 of IBP Handbook. United Kingdom: Blackwell. Reporting year: 1978.

HU S & FEDOROV AV. 2018. Cross-equatorial winds control El Niño diversity and change. Nature Climate Change, 8: 798-802. doi: 10.1038/s41558-018-0248-0.

INESON S, BALMASEDA M, DAVEY M, DECREMER D, DUNSTONE N, GORDON M, REN H, SCAIFE A & WEISHEIMER A. 2018. Predicting El Niño in 2014 and 2015. Scientific Reports, 8: 10733. doi: 10.1038/s41598-018-29130-1.

JIMÉNEZ-MUÑOZ JC, MATTAR C, BARICHIVICH J, SANTAMARÍA-ARTIGAS A, TAKAHASHI K, MALHI Y, SOBRINO JA & VAN DER SCHRIER G. 2016. Record-breaking warming and extreme drought in the Amazon rainforest during the course of El Niño 2015–2016. Scientific Reports, 6: 33130.

KAO HY & YU JY. 2009. Contrasting Eastern-Pacific and Central-Pacific Types of ENSO. Journal of Climate, 22(3): 615-632.

KUG JS, JIN FF & AN SI. 2009. Two Types of El Niño Events: Cold Tongue El Niño and Warm Pool El Niño. Journal of Climate, 22(6): 1499-1515.

LIMA NS, TÓTA J, BOLZAN MJA, FERREIRA AS & PIETZSCH M. 2017. A brief observation of the formation of coherent structures and turbulence over a rain forest area in Central Amazonia: the Atto-Claire/IOP–1/2012 experiment. Brazilian Journal of Geophysics, 35(3): 187–199.

MACKERETH FJH, HERON JT, TALLING JF. 1978. Water analysis: some revised methods for limnologists. Ambleside (UK): Freshwater Biological Association.

MARENGO JA, TOMASELLA J & UVO CR. 1998. Trends in streamflow and rainfall in tropical South America: Amazonia, eastern Brazil, and northwestern Peru. Journal of Geophysical Research: Atmospheres, 103(D2): 1775-1783.

McPHADEN MJ, LEE T & McCLURG D. 2011. El Niño and its relationship to changing background conditions in the tropical Pacific Ocean. Geophysical Research Letters, 38(15): L15709.

MOHTADI M, PRANGE M, SCHEFUSS E & JENNERJAHN TC. 2017. Late Holocene slowdown of the Indian Ocean Walker circulation. Nature Communications, 8: 1015.

NOAA/NCEP/NWS/EMC. 2017. Available on: <ftp://ftpprd.ncep.noaa.gov/pub/data/nccf/com/gfs/prod>. Access on: July/December, 2016/July, 2017.

PALISSA A. 1972. Mitteilungen aus dem Museum für Naturkunde in Berlin. Zoologisches Museum und Institut für Spezielle Zoologie (Berlin), 48(2): 449-450.

POVEDA G & MESA OJ. 1997. Feedbacks between Hydrological Processes in Tropical South America and Large-Scale Ocean–Atmospheric Phenomena. Journal of Climate, 10(10): 2690-2702.

VALDERRAMA JC. 1981. The simultaneous analysis of total nitrogen and total phosphorus in natural waters. Marine Chemistry, 10(2): 109–122.

ZHU J, KUMAR A, HUANG B, BALMASEDA MA, HU ZZ, MARX L & KINTER III JL. 2016. The role of off-equatorial surface temperature anomalies in the 2014 El Niño prediction. Scientific Reports, 6: 19677.

THE NANOSATC-BR, CUBESAT DEVELOPMENT PROGRAM –
A JOINT CUBESAT PROGRAM DEVELOPED BY UFSM AND INPE/MCTIC –
SPACE GEOPHYSICS MISSION PAYLOADS AND FIRST RESULTS

Nelson J. Schuch[1], Otávio S. C. Durão[2], Marlos R. da Silva[2], Fátima Mattiello-Francisco[2],
João B. dos S. Martins[3], Andrei P. Legg[3], André L. da Silva[3] and Eduardo E. Bürguer[3]

ABSTRACT. The INPE-UFSM's NANOSATC-BR, CubeSats Development Program started in 2008. Currently, the Program counts with two CubeSats: the NANOSATC-BR1 (1U) launched in 2014 and still in operation & the NANOSATC-BR2 (2U), under development, which is expected to be launched in the last quarter of 2019. In this article, the scientific and technological results of the NANOSATC-BR1 and the finalization of NANOSATC-BR2 are presented. Considering the Capacity Building, the major target of the Program, the paper emphasizes the involvement of Universidade Federal de Santa Maria - UFSM undergraduate/graduate students in the conception, development and operation of NANOSATC-BR1, as well as the participation of the Instituto Nacional de Pesquisas Espaciais - INPE graduate students in the on-board data handling (OBDH) software subsystem development, verification and validation for the NANOSATC-BR2. In addition, the collaborations of other Space Science, Engineering and Computer Science institutions involved in Brazil and abroad are discussed. The Program has received financial support from the Brazilian Space Agency (Agência Espacial Brasileira - AEB) and the Ministry of Science, Technology, Innovation and Communications (MCTIC).

Keywords: CubeSats, nanosatellites, capacity building.

RESUMO. O programa NANOSATC-BR, Desenvolvimento de CubeSats, parceria INPE – UFSM, teve início em 2008. Atualmente, o Programa conta com dois CubeSats: o NANOSATC-BR1 (1U), lançado em 2014 e ainda em operação, e o NANOSATC-BR2 (2U), que está em desenvolvimento e tem expectativa de lançamento no último trimestre de 2019. Nesse artigo, a finalização do desenvolvimento do NANOSATC-BR2 e os resultados científicos e tecnológicos do NANOSATC-BR1 são apresentados. Considerando a Capacitação Profissional, o maior objetivo do Programa, o artigo dá ênfase ao envolvimento dos alunos de graduação da Universidade Federal de Santa Maria (UFSM) na concepção, desenvolvimento e operação do NANOSATC-BR1, ao mesmo tempo em que enfatiza a participação dos alunos de pós-graduação do Instituto Nacional de Pesquisas Espaciais (INPE) no desenvolvimento, verificação e validação do Subsistema de Computador de Bordo para o NANOSATC-BR2. Além disso, colaborações de outras instituições de Ciência Espacial, Engenharia e institutos de computação aplicada do Brasil e exterior, são igualmente discutidas. O Programa recebeu suporte financeiro da Agência Espacial Brasileira (AEB) e do Ministério da Ciência, Tecnologia, Inovações e Comunicações (MCTIC).

Palavras-chave: CubeSats, nanosatélites, formação de recursos humanos.

---

[1]Instituto Nacional de Pesquisas Espaciais, Centro Regional Sul de Pesquisas Espaciais – CRS/COCRE/INPE-MCTIC, Santa Maria Space Science Laboratory – LACESM/CT-UFSM, Santa Maria, RS, Brazil – E-mail: njschuch@gmail.com

[2]Instituto Nacional de Pesquisas Espaciais – INPE/MCTIC, São José dos Campos, SP, Brazil – E-mails: otavio.durao@inpe.br, marlos.silva@inpe.br, fatima.mattiello@inpe.br

[3]Universidade Federal de Santa Maria – UFSM, Technology Center, Santa Maria, RS, Brazil – E-mails: batista@inf.ufsm.br, andrei.legg@gmail.com, andre.silva@ufsm.br, eduardoebrg@gmail.com

INTRODUCTION

The NANOSATC-BR, CubeSat Development Program, consists of a Brazilian INPE-UFSM Capacity Building Program on space science, engineering and computer sciences for the development of space technologies based in the CubeSat standard, which started with the first Brazilian Scientific Nanosatellite: the NANOSATC-BR1. The Capacity Building Program was conceived at the Southern Regional Space Research Center (Centro Regional Sul de Pesquisas Espaciais – CRS), from the Brazilian National Institute for Space Research (Instituto Nacional de Pesquisas Espaciais – INPE/MCTIC), where acts the Program's General Coordinator and Manager, with technical collaboration and management of the Mission's General Coordinator for Engineering and Space Technology at INPE's Headquarter (HQ), in São José dos Campos, São Paulo. The Program has the involvement of undergraduate students from the Universidade Federal de Santa Maria – UFSM and graduate students from INPE/MCTIC, ITA/DCTA/CA-MD and UFRGS.

This article explains the Program institutional arrangement and the technical characteristics of the satellites and their missions. The Program has support from the Brazilian Space Agency (Agência Espacial Brasileira – AEB) and from the Ministry of Science, Technology, Innovation and Communications – MCTIC.

NANOSATC-BR: CAPACITY BUILDING

The major objective of the INPE-UFSM's NANOSATC-BR, CubeSats Development Program, through the NANOSATC-BR1 & NANOSATC-BR2 CubeSats Projects, is to perform a Specialized Human Resource Capacity Building Program through the training of UFSM's undergraduate students, through Science, Technological & Innovation Initiation at INPE/MCTIC, in the main areas of Engineering, Computer Sciences and Physics.

Students have an important weight on the Project's technical and scientific branches, since their tasks provide results for each subsystem. The results are consequence of their hard work developed in conjunction with the UFSM's and INPE's specialists (Engineers, Technologists and Researchers), which are the main providers of information.

The brand new Laboratory of Integration and Tests of Nanosatellites (LITN), established at INPE – CRS in the end of 2017, provides an unique environment for students to perform hands on training, by the usage of the Engineering Model of the first satellite of the Program: the NANOSATC-BR1 (or NCBR1). LITN provides to students the adequate tools to perform basic Assembly and Integration operations on a CubeSat Platform, as well as basic Tests, that is, ATT – Assembly, Integration and Tests, with the equipment from the Ground Station (GS), which is now fully integrated to the LITN workbench (Fig. 1).
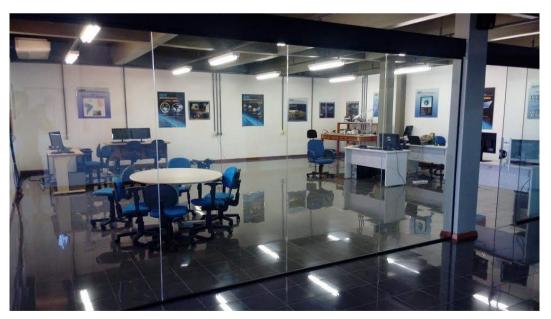

Figure 1 – The Santa Maria Ground Station Control Room (GS) and the Laboratory of Integration and Tests of Nanosatellites (LITN) integrated at the CRS/COCRE/INPE – MCTIC, in Santa Maria, RS, Brazil.
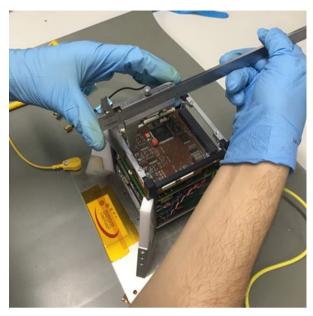
Figure 2 – Aerospace and others Engineering student at LITN using a caliper to perform measurements in a CubeSat.

Figure 3 – Electrical Engineering student at LITN using a micrometer to evaluate the thickness of a PCB.

Students from the new Aerospace Engineering and others Engineering courses at the Universidade Federal de Santa Maria (UFSM) can now use instruments, such as calipers (Fig. 2) and micrometers (Fig. 3), at LITN, in order to correctly evaluate mechanical and mass properties of satellite components.

Through the NANOSATC-BR Program, it was possible to approximate the Brazilian Space Program to universities, such as: UFSM, UFRGS, UFRN, UFABC, UFMG and USP. Therefore, the Program provides hands-on training and learning with Aerospace Engineering & Technologies and Space Weather issues.

Students also had the opportunity to perform further training at universities and space industries abroad: University of Würzburg and German Aerospace Center (DLR) – Germany; Innovative Solutions In Space (ISIS) – The Netherlands; Sapienza Università di Roma – Italy; University at Buffalo, University of Tennessee and NASA – Goddard Space Flight Center – USA. Funding came from several institutions, such as the CubeSat Dutch company Innovative Solutions in Space (ISIS), the Van Allen Project-NASA, the Brazilian Space Agency (AEB) and the Brazilian Program Science without Borders (SwB).

NANOSATC-BR: MISSIONS

The Program already consists of two CubeSats, the NANOSATC-BR1 and NANOSATC-BR2 (Fig. 4) and has the possibility of launching three other CubeSats in the next five years, operating them in space for at least 6 months each. These new missions aim to study and monitor the Geospace and Space Weather.

The NANOSATC-BR1 concept was developed to: i) monitor, in real time, the Geospace, the disturbances at the Earth's Magnetosphere over the Brazilian territory, and ii) the determination of their effects on regions such as the South America Magnetic Anomaly (SAMA). Its payloads are:

- A XEN-1210 three-axis magnetometer with a resolution of 15nT from the Dutch company XI – Xensor Integration (www.xensor.nl);

- One board has the magnetometer, which is the scientific payload. It is responsible to measure the perturbations associated with the SAMA.

The NANOSATC-BR1 Technological Mission carries a FPGA (Guareschi et al., 2010) and one integrated circuit (IC) designed by the Santa Maria Design House (SMDH), together with the Graduate Program in Microelectronics from UFRGS (Universidade Federal do Rio Grande do Sul), that were developed

Figure 4 – The NANOSATC-BR1 and NANOSATC-BR2 Engineering Model Platforms.

for space use due to their radiation resistance. The two technological payloads then use two different techniques for fault tolerance due to radiation in space: design (IC) and embedded (software) FPGA. These were the first circuits designed in Brazil for space applications.

NANOSATC-BR1: CURRENT SITUATION

The NANOSATC-BR1, is a 10x10x11.3 cm cube, weighing 0.965 kg. Its name and up and down frequencies link were determined by The International Amateur Radio Union – IARU, in 2011.

The NANOSATC-BR1's Engineering Model Platform (EM), the Flight Model Platform (FM), the Ground Support Equipment and the Ground Station for the INPE-UFSM's NANOSATC-BR1 mission and equipment were provided, integrated and pre-tested by the ISIS company from Delft, The Netherlands, except for the integration of the flight model done at the INPE/MCTIC's Integration and Testing Laboratory (LIT). The full Assemble, Integration and Tests (AIT) of the complete CubeSat (platform and payload) were also done at LIT.

The NANOSATC-BR's Ground Station Network (GS) is already installed and in operation: GS(INPE-CRS), at CRS/COCRE/INPE-MCTIC, Santa Maria, RS; and GS(INPE-ITA) at ITA/DCTA-MD, in São José dos Campos, SP, in Brazil (Fig. 5).

The NANOSATC-BR1 was launched as a tertiary payload by ISIS in the event ISILAUNCH 07, by a DNEPR launcher, at The Yasny Launching Base, in The Donbarovsky Region, Russia, on June 19th, 2014 – Launch time (T): 19:11:11 UTC – Local time at Yasny: 01:11.

The NANOSATC-BR1 already completed more than three years in orbit sending payloads and subsystems data. All payloads and subsystems, except the batteries in the power subsystem, continue to operate normally. The battery can no longer hold a charge because it was damaged by magnetic solar storms in September-October 2014. Therefore, the NANOSATC-BR1 can transmit only when it is in sight by the Sun. However, weekly Mr. Reiner Rothe, a german radio amateur and Mr. Paulo Leite (PV8DX), a radio amateur from Boa Vista, RR, Brazil, are performing the NANOSATC-BR1 tracking, downloading and sending systematically these data to the Program's data base, at INPE, in São José dos Campos, SP, in Brazil.

THE NANOSATC-BR1 TECHNOLOGICAL PAYLOAD – THE SMDH-IC RESULTS

The Santa Maria Design House (SMDH), with design techniques and others considerations, developed Integrated Circuits (IC) for space application regarding Total Ionization Dose (TID): instantaneous radiation dose effects denominated Single Event Effects (SEE) and Displacement Damage (DD). Specific Integrated Circuit (ASIC) was developed for one of the technological payloads of the NANOSATC-BR1 Project. The radiation hardened digital cells designed by SMDH proved a tolerance to solar energetic particles with energies of up to 100 MeV.

The SEE tolerance of two shift-registers, with 256 stages and 8 inverters between each chain, is shown in Figure 6. The blue bar corresponds to the shift registers designed using the conventional digital cells provided by the foundry. On the other hand, the red bars represent the radiation hardened digital cells

Figure 5 – The NANOSATC-BR's Ground Station Network (GS) was installed and it is in operation: on the left – The GS(INPE-CRS) at CRS/COCRE/INPE-MCTIC, in Santa Maria, RS; and on the right – The GS(INPE-ITA) at ITA/DCTA-MD, in São José dos Campos, SP, in Brazil.
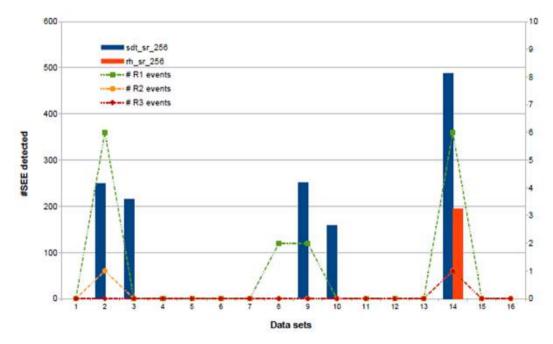

Figure 6 – The NANOSATC-BR1 SEE tolerance comparison of two shift-registers (256 stages, 8 inverters) (Medeiros et al., 2014; Noval et al., 2016).

designed by SMDH. It is remarkable to mention that radiation hardened cells designed by SMDH proved tolerance to SEE with X-rays events of severity R1 and R2 (Noval et al., 2016) – Minor and Moderate Radio Blackouts, respectively. In relation to the R3 event (Noval et al., 2016) – Strong Radio Blackout, the designed cells reported some errors by SEE. The amount of errors in the shift-registers designed using the standard cell library is larger than the shift registers using rad-hard cell library.

The Solar Energetic Protons detected by GOES-15 satellite during September 2014 were used in order to analyze and quantify the energy levels measured during the R3 occurrence and thus estimate the tolerance of customized cells. The fluency of Solar Energetic Protons – SEPs (Medeiros et al., 2014) during September 2014 at different levels of energy is shown in Figure 7. During the first two weeks were reported SEPs with energies above 100 MeV.

Figure 7 – The Solar Energetic Protons – SEPs detected by GOES-15 satellite during September 2014 (Medeiros et al., 2014).

THE GEOMAGNETIC FIELD INTENSITY RESULTS DETECTED BY THE NANOSATC-BR1 MISSION PAYLOAD

The NANOSATC-BR1 data were collected by the Scientific Mission Payload, which is a XEN-1210 magnetometer. The observations showed an excellent correlation with the theoretical figures for the Geomagnetic Field intensity, given by the International Geomagnetic Reference Field model (IGRF-IAGA/IUGG) in the same altitude. A map of the total intensity of the Geomagnetic Field for an altitude at 614 km over South America, in the domain of the SAMA (Heirtzler, 2002), is presented in Figure 8. The spatial variation of the total intensity of the Geomagnetic Field varies between 24.000 nT and 17.000 nT at the center of the SAMA, signalized by a black star in Figure 8. The Nanosatellite Earth Tracking and Control Station, GS(INPE-CRS), in Santa Maria – RS, is lying near the center of SAMA. The red line in Figure 5 indicates the approximate orbit of the NANOSATC-BR1 on August 17, 2014, from 10:57h to 11:07h. During this period, the NANOSATC-BR1 moved from South Pole towards to the geographic North Pole.

NANOSATC-BR2: CURRENT SITUATION

Since the NANOSATC-BR2 is a 2U CubeSat (10x10x22.6 cm), it permits a more ambitious mission than its predecessor, the NANOSATC-BR1, with three major objectives: academic and capacity building, scientific mission and technological mission development. The scientific mission is to monitor the Earth's Ionosphere and Magnetic Field. The Ionosphere composition disturbances in the SAMA region over Brazil have severe effects on satellite telecommunications, as well as the precise location with services such as the GPS. The payload equipment for the scientific mission will be a Langmuir probe and a XEN-1210 Magnetic Field sensor based on the Hall effect. The Langmuir probe is normally available in a larger size, however it is being miniaturized for a small satellite mission.
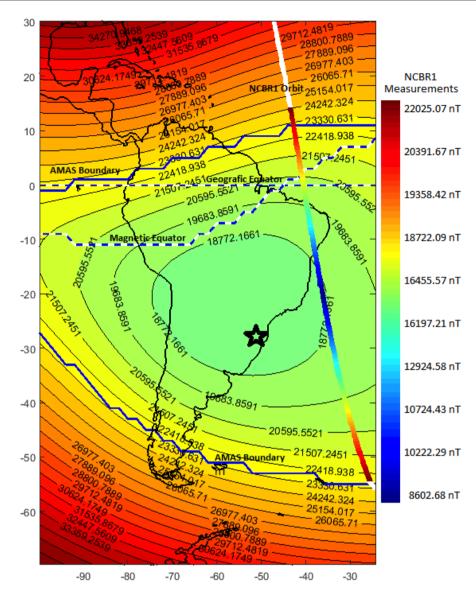
Figure 8 – SAMA Geomagnetic Field total Intensity modeled by the IGRF-10 and NANOSATC-BR1 Scientific mission payload measurements at 614 km altitude in 2014 for the Geomagnetic Field. The black star indicates the location of the Tracking and Control Station, GS(INPE-CRS), in Santa Maria – RS, which located near the center of the SAMA.

In order to finalize the NANOSATC-BR2, which is now also known by the acronym NCBR2, its platform was developed to satisfy the payload equipment's requirements. The on-board data handling (OBDH) software is a key element for payload integration in NCBR2. It is a software developed at INPE by graduate students of the Space System Engineering Course (INPE/CSE) in collaboration with emergent companies leaded also by INPE's former students. A short Verification and Validation (V&V) process was defined, addressing the interoperability and

robustness issues on the interactions among the OBDH and the mission payloads (Conceição et al., 2016). Model-based Testing approaches support the integration testing of the communicating software-intensive systems with the use of a fault-Injection mechanism for robustness verification purposes (Almeida & Mattiello-Francisco, 2017; Batista et al., 2018).

The NANOSATC-BR2 also has the first satellite attitude determination subsystem, fully developed in Brazil, from software to hardware, as one of its experiments. It has triple redundancy

using three microprocessors with one in hot standby. It's a joint project led by the UFMG with UFABC and INPE. The NCBR2 CubeSat will also carry two other technological experiments as version 2 of those that are flying in NANOSATC-BR1. It also carries an amateur radio communication experiment from Amateur Radio in Space – Brazil (AMSAT-Br) and Brazilian Amateur Radio Broadcasting League (LABRE).

All of those payloads are being integrated and tested with the OBDH software in the Engineering Model (EM), with the exception of the version 2 of the board flying in NANOSATC-BR1, during the final of the integration phase:

- Langmuir Probe – Delivered for testing and integration with the NANOSATC-BR2 EM platform and the on-board software – OBDH;

- Communication Experiment Packet (store forward) – AMSAT-BR and SP-LABRE;

- CubeSat board with three experiments – FPGA/UFRGS; Magnetometer; IC/SMDH/UFSM, first unit scheduled for delivery in October 2018.

The entire platform flight software was developed in Brazil, by researchers and engineers from INPE/MCTIC, already working in this area (Attitude Determination & Control and Data Management), taking advantage of the experience of NANOSATC-BR1; students graduated at INPE/MCTIC on the course of the Space System Engineering (CSE), undergraduate and graduate students and third parties startup company created by former INPE/MCTIC graduate students. The Control Law for the control software has also been developed in house.

The Project has already received the budget from AEB for contracting the launch and future operation of NANOSATC-BR2 in orbit. The NANOSATC-BR2 is expected to be launched in the last quarter of 2019. Likewise NANOSATC-BR1 and other CubeSat projects, the NANOSATC-BR2 will be launched in a piggyback launch, as a tertiary payload. The launch opportunities as well as the Launch Vehicle are under contract.

CONCLUSION

Since it provides to young people contact with low cost and fast development on Space Technology, the Brazilian: INPE-UFSM, NANOSATC-BR, CubeSat Development Program, proved to be an excellent tool for developing a new generation of Scientists, Engineers and Researchers in Aerospace Technologies in Brazil.

It is expected an increase in the Brazilian Government Agencies support with more investments for the development of Space Technology and new university initiatives. Examples such as the Brazilian INPE-UFSM NANOSATC-BR, CubeSats Development Program, with its two models (the NANOSATC-BR1 & NANOSATC-BR2 Projects) should be taken into account in this sense.

REFERENCES

ALMEIDA DP & MATTIELLO-FRANCISCO F. 2017. Modeling of the interoperability between on-board computer and payloads of the NanoSat-BR2 with support of the UPPAAL tool. In: 1st IAA Latin American Symposium on Small Satellites. Colombia, Session 9/IAA-LA-09-01. Available on: <http://www.unsam.edu.ar/institutos/Colomb/Presentaciones/Session.9/IAA-LA-09-01.pdf>.

BATISTA CLG, MARTINS E & MATTIELLO-FRANCISCO MDF. 2018. On the use of a failure emulator mechanism at nanosatellite subsystems integration tests. In: 19th IEEE Latin-American Test Symposium (LATS). São Paulo, Brazil. p. 1–6.

CONCEIÇÃO CA, MATTIELLO-FRANCISCO F & BATISTA CL. 2016. Dependability verification of nanosatellite embedded software supported by a reusable Test System. In: Seventh Latin-American Symposium on Dependable Computing (LADC). Cali, Colombia. p. 157–163.

GUARESCHI WN, SCHUCH NJ, PETRY A, CHARÃO A & TAMBARA LA. 2010. Analysis of Field Programmable Gate Array Alternatives for use in Nanosatellites. In: 61st IAC, International Astronautical Congress. Prague, Czech Republic: International Astronautical Federation. IAC-10.B4.6B.12.

HEIRTZLER J. 2002. The future of the South Atlantic anomaly and implications for radiation damage in space. Journal of Atmospheric and Solar-Terrestrial Physics, 64(16): 1701–1708.

MEDEIROS L, ZAFFARI C, NOVAL J, TEIXEIRA L & MARTINS J. 2014. Using the NANOSATC-BR1 to evaluate the effects of space radiation incidence on a radiation hardened ASIC. In: 1st IAA Latin American CubeSat Workshop. Brasília, Brazil.

NOVAL J, MEDEIROS L, MARTINS J, SCHUCH N, DURÃO O & MACHADO R. 2016. Design considerations for Radiation Hardened ASIC used as technological payload in NANOSATC-BR1. In: 2nd IAA Latin American CubeSat Workshop. Florianópolis, Brazil. IAA-BR-16-0S-0P.

Brazilian Journal of Geophysics

RBGf

GEOACOUSTIC PATTERNS OF THE GUAÍBA RIVER BOTTOM AND SUB-BOTTOM AND THEIR RELATIONSHIP WITH SEDIMENTARY AND HYDRODYNAMIC PROCESSES

Fernando Comerlato Scottá, Mauro Michelena Andrade, Vicente Oliveira Silva Junior, Natacha Oliveira,
Jair Weschenfelder, Eduardo Calixto Bortolin and José Carlos Nunes

ABSTRACT. This work aimed at studying the bottom and sub-bottom geoacoustics of the Guaíba River, whose echo patterns are related to hydrodynamic patterns and sedimentary processes. A total of 324 km of seismic transects were surveyed using the Stratabox high-frequency (10 kHz) profiler with concomitant imaging using a side-scan sonar in the northern and central areas of the Guaíba system. The records were interpreted with the aid of complementary data (bathymetry and bottom samples), and maps containing the spatial arrangement of echo-characters were developed. The echo-characters were classified into seven different types according to the presence of sediments controlled by the hydrodynamics of the system or modified by human action. In general, the echoes related to the deposition of fine sediments occurred in deeper areas, the navigation channel or surrounding areas. The echoes in the shallower areas presented strong acoustic reflectivity at sites with lower deposition of fine sediments and predominance of sandy sediments. The occurrence and morphology of asymmetric subaqueous dunes indicated a predominant north-to-south flow and a river behavior.

Keywords: shallow geophysics, sedimentology, hydrodynamics, geoprocessing.

RESUMO. Este trabalho tem por objetivo o estudo geoacústico de fundo e subfundo do rio Guaíba, cujos padrões de ecos são relacionados aos padrões hidrodinâmicos e aos processos sedimentares atuantes. Foram levantados 324 km de perfis sísmicos em extensão, com o perfilador de alta frequência (10 kHz) Stratabox e concomitante imageamento com sonar de varredura lateral nas áreas norte e central do Guaíba. Os registros foram interpretados com o auxílio de dados complementares (batimetria e amostras de fundo) e foram confeccionados mapas com a disposição espacial dos eco-caráteres. Os eco-caráteres foram classificados em sete diferentes tipos, de acordo com a presença de sedimentos controlados pela hidrodinâmica do sistema ou modificados pela ação humana. De uma forma geral, os ecos relacionados à deposição de sedimentos finos ocorrem nas áreas mais profundas, no canal de navegação ou adjacências. Os ecos nas áreas mais rasas apresentam forte refletividade acústica, em locais com menor deposição de sedimentos finos e predomínio de sedimentos arenosos. A ocorrência e morfologia de dunas subaquosas assimétricas indicam um fluxo preponderante no sentido norte-sul e um comportamento fluvial do sistema aquático.

Palavras-chave: geofísica rasa, sedimentologia, hidrodinâmica, geoprocessamento.

Universidade Federal do Rio Grande do Sul – UFRGS, Instituto de Geociências, Avenida Bento Gonçalves, 9500, 91540-000 Porto Alegre, RS, Brazil – E-mails: fernandoscotta.sema@gmail.com, mauromichelena@gmail.com, voliveirasjr@gmail.com, natoliveiran@gmail.com, jair.weschenfelder@ufrgs.br, eduardo_bortolin_22@hotmail.com, jose.nunes@ufrgs.br

INTRODUCTION

Integrated management of the coastal zone and its various associated environments requires precise spatial datasets covering large areas, which are sometimes inaccessible by direct sampling methods (Kotilainen & Kaskela, 2017). In the submerged environment of coastal areas, seismic data sampling is important and can help in the management of these environments since it allows the recognition of the type of bottom and sub-bottom, knowing sedimentary processes, and also infer in the environment hydrodynamics (Catanzaro et al., 2004; Veronez Jr et al., 2009a, 2009b).

The first studies using seismic data were carried out in marine environments (Damuth, 1975; Damuth & Hayes, 1977) and later were applied in shallow areas, facing a greater navigability restriction imposed to large vessels (e.g. Baptista Neto et al., 1996; Nitsche et al., 2004). The advancement of technology has contributed to a larger portability of geophysical equipment, allowing the development of studies in restricted areas that were previously inaccessible onboard large vessels (Souza, 2006). In these environments, geoacoustic sensors have been increasingly used since the late 1990s (Clarke et al., 1996).

In Brazil, several seismic studies have been conducted in areas of bays, lakes, rivers, and estuaries (Quaresma et al., 2000; Catanzaro et al., 2004; Hatushika et al., 2007; Paolo & Mahiques, 2008; Veronez Jr et al., 2009a, 2009b; Quaresma et al., 2011; Marino et al., 2013; Silva et al., 2014; Barros et al., 2017). These research works have identified and classified echo-characters and sonographic patterns, which can be defined according to their reflection patterns (seismic facies). Thus, the echo-character can be correlated with the size and texture of the bottom sediments (Veronez Jr et al., 2009a).

In the state of Rio Grande do Sul (RS), southern Brazil, several studies carrying out seismic surveys have been conducted in Patos Lagoon (Toldo Jr et al., 2000; Weschenfelder et al., 2006; Weschenfelder et al., 2010; Baitelli, 2012; Weschenfelder et al., 2014; Santos-Fischer et al., 2016; Bortolin, 2017; Bortolin et al., 2019). These works mainly aimed at constructing an evolutionary model of Patos Lagoon (PL), a large water body with an area of 10,000 km². Seismic records revealed channels that deeply dissected the region before the formation of the current coastal plain (Weschenfelder et al., 2010; Baitelli, 2012; Weschenfelder et al., 2014). In another study, Weschenfelder et al. (2006) indicated the PL sectors that contain gas accumulation, which were areas with paleo-topographic lows associated with river channels and valleys that were developed in the RS coastal plain during the regressive/transgressive events from the Quaternary.

More recently, studies relating sonographic patterns to the bottom sediment were conducted in the RS coastal areas. Oliveira (2017) analyzed the southern portion of the RS continental shelf near the PL mouth and identified acoustic anomalies as a response to the presence of interstitial gas in the sediment. Bexiga (2016) also carried out a similar study in the PL Southern Sector, describing three echo patterns and the presence of gas in seismic profiles. Moreover, Silva Jr. (2017) analyzed some of the seismic data used here and preliminarily identified some echo-facies patterns from the northern portion of the Guaíba River.

Important RS water bodies lack geoacoustic studies to identify the bottom and sub-bottom depositional architecture as well as sedimentary characteristics and processes. Thus, the objective of this work is to study the bottom and sub-bottom geoacoustics of the Guaíba River, whose echo patterns are related to hydrodynamic patterns and sedimentary processes.

STUDY AREA

The Guaíba system is a water body of about 496 km² (Fig. 1) located next to the city of Porto Alegre, capital of RS. It is formed by the confluence of the Jacuí, Sinos, Caí, and Gravataí rivers, receiving the drainage of nine sub-basins that extend through the center and northeast of RS, covering an area of approximately 84,763 km². It supplies water to the cities of Porto Alegre, Guaíba, Barra do Ribeiro, and Viamão. In addition to the water supply, it has several uses such as fishing, leisure, and cargo and people transportation.

In terms of bathymetry, the Guaíba River presents an average depth of 2 m (Nicolodi, 2007), but with recorded values over 30 m near the city of Itapuã (CHM, 2012). However, its important morphological characteristic is the presence of a navigation channel that mainly varies between 4 and 8 m deep (DNAEE, 1983), reaching 14 m deep at some sites.

The definition of Guaíba Lake or River is the subject of frequent debates in the most diverse sectors of our society. The Guaíba system is officially defined as a river by the Brazilian Navy (CHM, 2012) and as a lake by the city hall of Porto Alegre (DMAE, 2018). Academic divergences are also frequent. Menegat & Carraro (2009) define the Guaíba system as a lake and state that its flow only occurs superficially, a common feature of lakes. Toldo Jr & Almeida (2009) recognize the Guaíba system as a river due to the presence of a main channel that presents strong water flows, a feature that would not be observed in lakes.
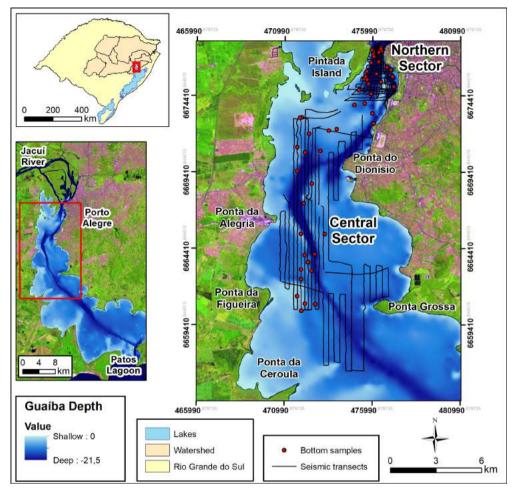
Figure 1 – Location of the study area. Seismic lines and collected bottom samples. The Northern Sector corresponds to the upstream end of the Guaíba River; the Central Sector represents the area from the south of Pintada Island until near Ponta da Ceroula. Landsat 8 image, OLI sensor, 6R5G4B composition. Coordinates in UTM, zone 22S.

Despite the strong anthropic pressure exerted on this water body, one factor to be highlighted is the lack of available data and published studies, which itself makes it difficult to classify it as a river or lake. Information on its bottom is found on the textural maps available in CECO (1999), which were developed using field sampling and allowed the analysis of this environment general behavior. Seismic studies using an acquisition grid with significant data and information on the bottom and sub-bottom have not been found.

MATERIAL AND METHODS

Sampling and data collection in the field

A total of 324 km of data transects (Fig. 1) were acquired with a 10 kHz Stratabox seismic profiler and concomitant bottom imaging using a 455 kHz Humminbird 798ci SI Side-Scan Sonar (SSS), both coupled to a Differential Global Positioning System (DGPS). For logistic reasons, this study focused on the Northern (NS) and Central (CS) sectors of the Guaíba River. Ten campaigns were carried out in the following periods and locations: January 2016 in the NS (3 days); June 2016 in the NS and CS (5 days); February 2017 in the CS (2 days).

Seismic data were sampled by navigating at speeds between 3 and 4 knots, allowing the generation of an adequate aspect ratio for the images (Paolo & Mahiques, 2008). In order to aid the interpretation of seismic profiles, 42 bottom samples were preferentially collected on the acquired seismic transects (Fig. 1). A type of Van Veen bottom sampler was used, which does not allow the loss of fine sediments when it is being hoisted to the vessel (Carvalho et al., 2000).

Data from seismic profilers sampled in previous years were also used to support the interpretation of the geoacoustic grid in some specific regions. The data corresponded to the following dates and equipment operating frequencies:

- Data acquired in 2006 at a 3.5 kHz frequency in the navigation channel area (deeper areas);

- Data acquired in 2012 and 2014 with the same seismic profiler used in the mapping from this study (10 kHz Stratabox).

Data analysis

The main steps of this study were: granulometric analysis of bottom samples; interpretation and classification of seismic profiles; integration of data to produce maps with geoprocessing techniques; and finally, hydrodynamic and sedimentological interpretation.

The bottom samples were dry sieved at 0.5-phi intervals. The silt and clay fraction was separated from the rest with a 4-phi sieve. The bottom samples served as field truth for further interpretation of seismic transects.

The seismic profiler data were interpreted and classified using the SonarWiz, Reflexw, and Stratabox computer programs. The SSS data were used to support the interpretation of the seismic records acquired by the sub-bottom profiler. Different echo-characters were classified according to the sediment acoustic response, microtopography and morphology of the bottom and sub-bottom as proposed by Damuth (1980). The bathymetry data from Nicolodi (2007) was also used as a basis for the interpretation of echograms.

Seismic data were arranged into vector (line) data in geoprocessing applications. From there, maps with the classifications of echo-characters were made. Finally, the sedimentation and hydrodynamics of the Guaíba system were interpreted.

Classification of subaqueous features

The classification of large-scale features according to Ashley (1990) was used, which names and standardizes the bottom undulations as subaqueous dunes and categorizes them into sizes based on their spacing (S) and height (H): very large dunes: $S > 100$ m, and $H > 5$ m; large dunes: $10 \leq S \leq 100$ m, and $0.75 \leq H \leq 5$ m; medium dunes: $5 \leq S < 10$ m, and $0.4 \leq H < 0.75$ m; small dunes: $0.6 \leq S < 5$ m, and $0.075 \leq H < 0.4$ m.

In addition to size and shape, Ashley (1990) also established a hierarchy with three orders of description on the main morphological characteristics of subaqueous dunes: first order: wavelength, height, and two (2D) or three (3D) dimensions; second order: size and orientation of overlapping features, and sediment characteristics (type and grain size); third order: facies angle and profile symmetry, area of bed coverage, and temporal evolution.

RESULTS AND DISCUSSION

Echo-character types

The echo-characters were classified based on the acoustic backscatter and bottom microtopography (Catanzaro et al., 2004), and were divided into seven different echo types named EC-1 to EC-7 (Tab. 1). The Northern (NS) and Central (CS) sectors of the Guaíba River, represented by Figures 2 and 3, respectively, were presented separately to facilitate the results visualization.

The main characteristic of echo 1 is that it has a low sub-bottom penetration and a predominantly flat terrain without any bottom features. This echo is mainly related to sandy sediments and is frequent in the Guaíba system (Figs. 2 and 3).

Echo 2 has bottom features, strong reflectivity, and low sub-bottom penetration. Its occurrence is concentrated at the upstream end of the Guaíba River and more sporadically in areas near the main channel (Figs. 2 and 3). The behavior of these two types of echo-characters – with strong reflection and low penetration – is similar to other studies in different areas of Brazil (Catanzaro et al., 2004; Paolo & Mahiques, 2008; Veronez Jr et al., 2009a; Baptista Neto et al., 2011; Silva et al., 2014).

Echo 3 presents abrupt and sporadic relief variations. It is similar to echo 1 regarding its strong reflection, but they differ with respect to the abrupt relief variation of echo 3. This type of echo is concentrated in the eastern areas from the NS, close to the Dilúvio Stream and the Beira Rio Stadium (Fig. 2).

Echo 4 is formed by discontinuous and chaotic reflectors and occupies widely varied elevations above the bottom, ranging from 6 to 14 m deep. This echo has high reflectivity and no penetration in most profiles. Sometimes its sound signal penetrates in the first reflector, evidencing a highly reflective and irregular sub-bottom surface. This echo is concentrated in the NS (Fig. 2) and CS at the upstream end of the Guaíba River and in the areas near Ponta do Dionísio and Ponta Grossa (Fig. 3), respectively. Echoes 3 and 4 are related to the presence of irregular bathymetry areas on the Guaíba River bottom.

Echo 5 presents sub-bottom reflectors located in the NS at the upstream end of the Guaíba River (Fig. 2). The bottom morphology is dominantly flat on this echo and sometimes

Table 1 – Types of classified echo-characters in the Guaíba River.

Echo	Description	Sediment	Occurrence	Profile
EC-1	Highly reflective surface, low penetration. Without bed forms.	Sand	Predominant in the CS.	
EC-2	Highly reflective surface, low penetration. With bed forms.	Sand	Upstream end of the Guaíba River and channel areas.	
EC-3	Highly reflective surface, low penetration. Abrupt relief variations.	Sand	Areas at the eastern margin. Only Northern Sector.	
EC-4	Basement highs or outcrops.	–	Upstream end of the Guaíba River and near rocky basement areas.	
EC-5	High penetration. Presence of several reflectors and one strong sub-bottom reflector.	Mud	Guaíba entrance. Only Northern Sector.	
EC-6	High penetration. Presence of sub-bottom reflectors.	Mud	Varied only in CS.	
EC-7	High penetration. Presence of regular sub-bottom reflector.	Sand	Sandy areas in Ponta da Figueira.	

presents irregular bottom shapes in the form of single ripples that may have migrated from nearby subaqueous dune areas (echo 2). This echo has several sub-bottom reflectors and presents a well-defined, flat, and high-amplitude one. While the other sub-bottom reflectors do not continuously appear in any area, this strong reflector was recorded over the entire extent of the echo 5 occurrence.

Echo 6 indicates a flat-bottom relief in most profiles and one or more sub-bottom reflectors located in several portions from the CS predominantly in the channel or deeper areas (Fig. 3). This echo was classified into three subtypes according to the sub-bottom reflector response (subtypes shown in Figure 11 and detailed later in the discussion). Echoes 5 and 6 have a better penetration of the acoustic signal and resolution of the sub-bottom reflectors. Echo 7 has a flat and regular reflector on the sub-bottom. This type is located near Ponta da Figueira, in the western Guaíba River area.

Previous studies have highlighted that SSS images do not allow the separation of echo-characters with the same degree of detail as a seismic profiler (Paolo & Mahiques, 2008; Veronez Jr et al., 2009a). Many features were not adequately recorded by the SSS and were indirectly interpreted by the variation of the water column (in the center of the image) in the sonographic records, similar to what was commented by Paolo & Mahiques (2008). One of the factors that made it difficult to acquire and interpret the SSS data was the shallow depths of the Guaíba system, which have an average of 2 m deep. In the shallower regions, SSS images had only a few meters of imaging extension (< 10 m long).

HYDRODYNAMIC AND SEDIMENTOLOGICAL INTERPRETATIONS BASED ON SEISMIC ANALYSES

Echo 2 and the mapping of subaqueous dunes

In the NS, the presence of subaqueous dunes (Echo 2) was recorded in the western portion of the studied area, parallel to Pintada Island, as well as in the shallower portions to the east of the navigation channel (Fig. 2). These dunes were asymmetrical, indicating a predominant flow in the north-to-south direction. The area to the east of the navigation channel presented small and medium dunes predominantly with medium sand grains. This variation occurred due to the shallow depths in referred site, ranging from 1 to 4 m.
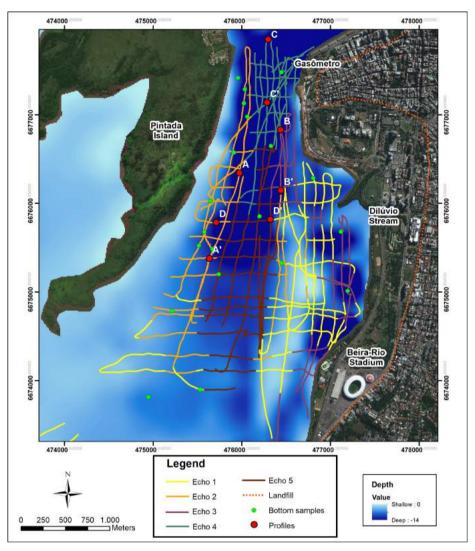
Figure 2 – Classification of echo-characters from the NS of the Guaíba River. The landfill areas were manually delimited based on the map by Hasenack (2008). Coordinates in UTM, zone 22S.

In the areas with subaqueous dunes in the western portion, a large north-to-south variation in the size of features was verified (Fig. 4), with very large dunes in the north end that gradually varied to medium and small dunes in the southern border of the study area. Variations in wavelength were also observed as a function of depth. Smaller dunes were concentrated in shallower regions, closer to the western margin, and larger dunes were found at greater depths farther from the shore. The presence of dunes and their size gradient was also confirmed in the profiles from 2006, 2012, and 2014.

The bottom samples showed more than 90% of sand in the areas with subaqueous dunes, as also observed in different environments in the literature (Fenster et al., 1990). However, the changes in the size of dunes were followed by a variation in the grain size of the sandy sediments that constituted them. The sediments with larger grain size – mainly the coarse sand fraction – and the medium to very fine sand fractions were concentrated in the north at the upstream end of the Guaíba River and in the southern portions, respectively.

In the CS, in the areas near the navigation channel close to Ponta do Dionísio, small and medium dunes were also mapped at 2.5 to 7 m deep (Fig. 3). In other regions to the south until Ponta da Ceroula and Ponta Grossa, no subaqueous dunes were found. The presence of subaqueous dunes in the channel
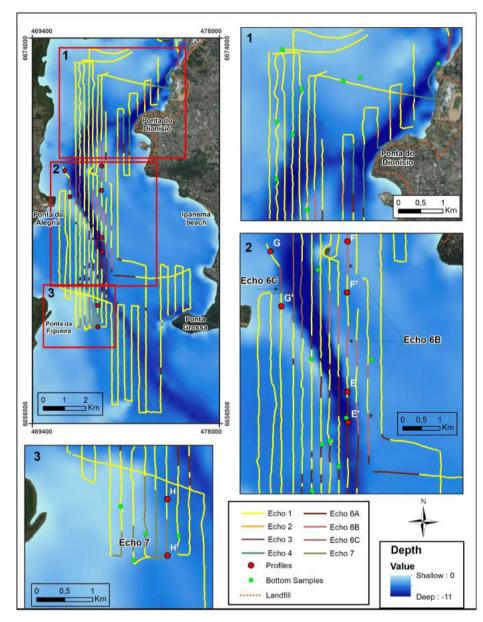
Figure 3 – Classification of the echo-characters from the CS of the Guaíba River. The landfill areas were manually delimited based on the map by Hasenack (2008). Coordinates in UTM, zone 22S.

area indicated higher flow velocities and gave evidence of a predominant north-to-south flow due to their asymmetry, which was constant along the seismic profiles.

The decrease in the size of ripples until their total absence showed that the flow competence decreased towards the south. The Guaíba River cross-section is initially about 0.8 km wide at Gasômetro and gets wider towards the south, reaching 4.3 km and 5.9 km wide in the sections at Ponta do Dionísio and Ponta Grossa, respectively (Fig. 3). This widening coincided with the

loss of transport competence of thicker sediments observed with the seismic profiles and the bottom samples, which showed a decrease of the sand grain size deposited on the bottom. This behavior was previously reported by other authors (Bacchi et al., 2000; Nicolodi, 2007), who observed that the river flow from the tributaries loses competence as a transport agent when draining into the Guaíba River.

The conditions required for the formation of subaqueous dunes according to Ashley (1990) are: environments deeper than
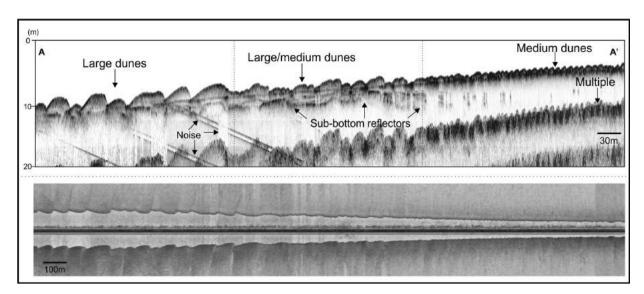
Figure 4 – Echo-character type 5. Subaqueous dunes profile in the NS from the Guaíba system. Top – acoustic profiler Stratabox. Bottom – SSS. Modified from Silva Jr (2017).

1 m; grain size greater than very fine sand (> 0.15 mm); and velocity of currents greater than 0.4 m.s^{-1}. The first and second conditions were met and confirmed by the use of the bathymetry and bottom samples, respectively. The higher velocities in the northern area were confirmed in the study by Andrade et al. (2017), who used a Doppler current acoustic profiler to measure currents at Ponta do Gasômetro in the Northern Sector of the Guaíba River (Fig. 5). In an example profile from September 15, 2015, the highest velocities, which were over 40 cm.s^{-1} (0.4 m.s^{-1}), occurred in the western area of the section, exactly where the dunes were located.

Subaqueous dunes were also mapped at the Guaíba River mouth in Itapuã (Fig. 6) using data measured by a 3.5 kHz seismic profiler in July 2006. These ripples were the size of medium dunes and presented asymmetry, indicating that the flow was predominantly from north to south. These bottom features are common in zones of intense current velocities and were previously described by Baitelli (2012). The longitudinal section of Itapuã is a few kilometers long – ranging from 3.6 to 5 km –, similarly to the section of Dionísio (Fig. 3), which is 4.3 km long. The narrowing of the section causes an increase in the current velocities in the flow channel area, producing the subaqueous ripples.

The presence of subaqueous ripples indicated that the flow reached the entire water column in these areas and did not only occur superficially as proposed by Menegat & Carraro (2009). This condition is also highlighted in Figure 5, where intense

velocities were evident at depths greater than 10 m and near the channel bottom.

The asymmetry of the subaqueous dunes confirmed that the flow in the Guaíba River is preferentially from north to south (DNAEE, 1983; Nicolodi, 2007; CHM, 2012), corroborating that the Guaíba system has a predominant river behavior. According to Ashley (1990), the formation of subaqueous dunes only takes place in three environments: rivers, tide-dominated coastal environments, and shallow marine environments. Since it is not a marine environment and has no tidal effect, the Guaíba system falls into the classification of a river.

Echo 3

Echo 3 occurred throughout the eastern area of the NS at the margins of the city of Porto Alegre (Fig. 2). Irregularities and abrupt relief variations indicated dredging and dredged material disposal (Fig. 7). Baptista Neto et al. (2011) also defined a similar echo using data from a similar equipment (10 kHz Stratabox) in Rodrigo de Freitas Lagoon, city of Rio de Janeiro, Brazil, and they associated it to dredging in the area.

The occurrence of echo 3 was related to the occupation history of the city, which has undergone seven landfill processes in its margin (Bohrer, 2001). The first landfill took place in the 19th century in 1888 aiming at expanding and modernizing its port area (Branco Filho, 2005). This operation continued in the 20th century to implement the other six landfills, finished between 1917 and 1978. According to Branco Filho (2005), the Praia de
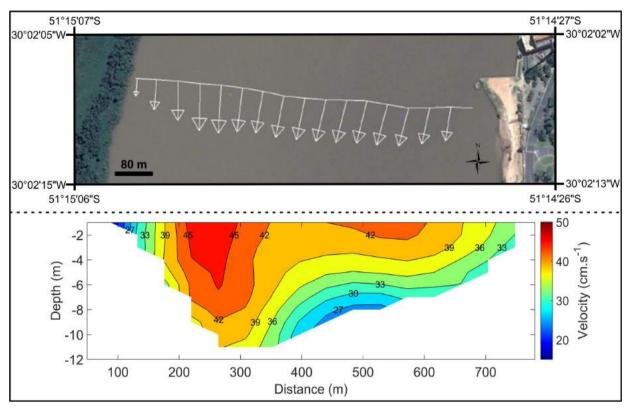
Figure 5 – Cross-section at Gasômetro. Top panel – velocity vectors from the surface layer. Bottom panel – side view of the cross-section. Source: Andrade et al. (2017).

Belas beach (next to Beira Rio Stadium) landfills in the 1970s were made with sediments from the Guaíba River, which were removed by dredging and using large pipes. On the other hand, regarding the other previously made landfills, there is no record on the methodology used.

Changes in the bottom morphology and depths can be observed comparing the 1960s nautical chart from the Brazilian Navy with the actual bathymetric map of this study (Fig. 8). According to the nautical chart this region had depths ranging from 0.1 to 1.4 m prior to the construction of the landfill, which are shallower than the current configuration of these areas with depth locally greater than 10 m.

Echo 4

Echo 4 was characterized by discontinuous and chaotic reflectors and a highly irregular and reflective bottom (Fig. 9). This echo-character was located close to the margins of Ponta do Gasômetro (Fig. 2), Ponta do Dionísio, and Ponta Grossa (Fig. 3), which are areas that present granitic rocks (Hasenack, 2008). These echo characteristics are associated with rock outcrops, which are the extension of nearby basement.

These echo-character has also been described with similar characteristics in other works, which have associated it with rock outcrops and rock blocks (Catanzaro et al., 2004; Veronez Jr et al., 2009a), showing a strong reflectivity due to the high intensity of its acoustic return signal (Veronez Jr et al., 2009a).

On the other hand, the Ponta do Gasômetro area is a landfill area that served as foundation to build a prison, which was destroyed in the 1960s and left debris that are still present at the Guaíba margins. In this specific area, the disposal of these remains is also a possible explanation for the echo-facies pattern observed in this study.

Echoes 5 and 6, and deposition of fine sediments

Echo-characters 5 and 6 showed more-pronounced sub-bottom reflectors and were related to the presence of fine sediments on the bottom and shallow sub-bottom. The bottom samples resulted in the predominance of fine sediments (65-99%) in these areas.

Echo 5 occurred in the NS of the Guaíba River aligned with the Dilúvio Stream mouth, which is where the Guaíba River practically doubles its cross-section width (Fig. 2). Veronez Jr et al. (2009a) also reported a similar echo using 10 kHz seismic
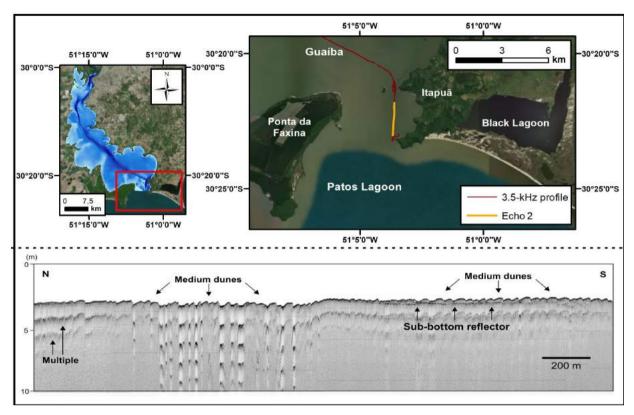
Figure 6 – Location and seismic profile (3.5 kHz) of subaqueous dunes mapped at the Guaíba River mouth in Itapuã. The north and south orientations are indicated in the profile.
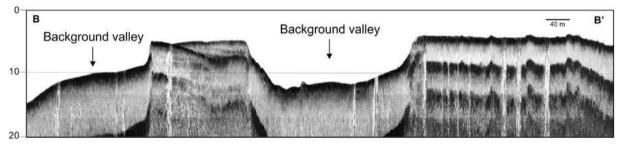

Figure 7 – Echogram associated with echo 3. Presence of large troughs on the bed and dredging disposals between the troughs. Modified from Silva Jr (2017).

profiling data from Vitória Bay and associated it with the mud or muddy-sand bottom.

These echograms showed thick tabular layers formed by the deposition of fine sediments and presented concordant reflectors on the sub-bottom (Fig. 10). It is possible to visualize several sub-bottom reflectors, but there was one presenting a high-amplitude (Fig. 10, Reflector R3) and a weaker deeper one (low-amplitude), not being present throughout the profile.

The high-amplitude sub-bottom reflector (R3) was identified throughout the echo 5 occurrence area, which was

a characteristic that defined this echo-character. At the sites adjacent to the channel margins, these echoes showed isolated sandy bars close to the formation of the echo 2 subaqueous dunes. These bars represented an intermediate phase between these sectors of high and low flow speed.

It is also noted that the echo 5 location was associated with the navigation channel and that it was found in its deeper portions, with depths varying from 5 to 14 m (Fig. 2). In probable conditions of low flows, the loss of competence favors the deposition of finer sediments. Nicolodi et al. (2010) defined three
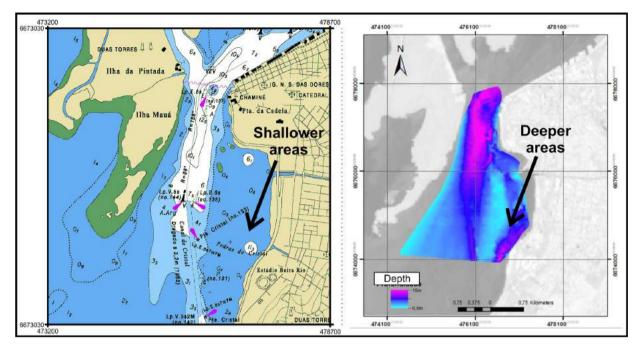
Figure 8 – Comparison between the 1960s Brazilian Navy nautical chart (CHM, 2012) and the bathymetric map from this work. The bathymetric map on the right was performed with seismic profiler data. Coordinates in UTM, zone 22S. Modified from Silva Jr (2017).
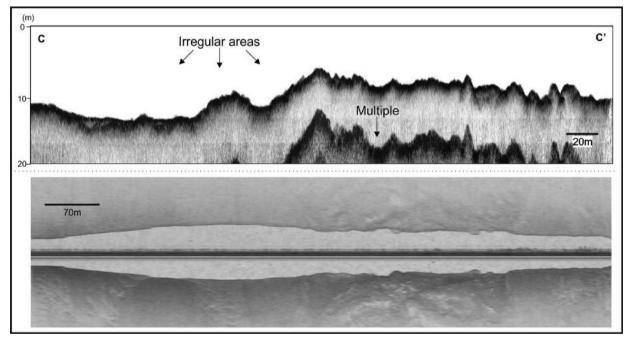

Figure 9 – Profile showing the echo type 4. Top – acoustic profiler Stratabox. Bottom – SSS. Modified from Silva Jr (2017).

different sedimentary environments according to the potential for fine sediment resuspension in the Guaíba River: erosional, transitional, and depositional bottoms. The depositional bottom corresponds to areas with fine sediment deposition, characteristic of regions that are protected from the main resuspension forces and that have low hydrodynamic energy (Nicolodi et al., 2013).
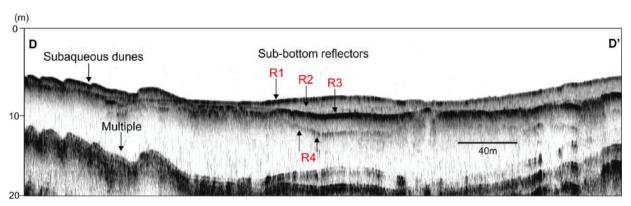
Figure 10 – Echo-character type 5 and sub-bottom strata. Modified from Silva Jr (2017).

These areas showed great spatial similarity with the areas classified as echo 5 and confirmed the dominance of a fine sediment depositional area in the NS of the Guaíba River.

The coastal fluvial courses from the Guaíba watershed maintained their positions relatively fixed during the Quaternary period. The sub-bottom morphology that showed strong amplitude of the echo 5 reflector can be interpreted as the position of the paleochannel bed of the former Jacuí River course, which dissected the entire length of the Guaíba River basin until it met PL (Weschenfelder et al., 2010, 2014). This paleochannel had the same position of the current navigation channel from the Guaíba River, thus being a morphological inheritance of the relief dissection during periods of lower base level, drowned by the high and transgressive sea from the end of Holocene (Weschenfelder et al., 2016; Santos-Fischer et al., 2016, 2018).

Echo 6 occurred in the CS in the channel and in other predominantly deeper areas, ranging from 2.5 to 11 m deep. The quantity and arrangement of reflectors was varied and did not present a uniform pattern. Thus, this echo was divided into 3 subtypes shown in Figure 11. Echo 6A showed a pattern of various sub-bottom strata, which were concordant in most profiles. Eventually, the presence of a high-amplitude sub-bottom reflector was exclusively identified in the channel areas, also interpreted as the position of the Jacuí River paleochannel bed (Fig. 11). This reflector resembled the characteristics of echo 5, which presented a high-amplitude sub-bottom reflector throughout its extension.

Echo 6B was located in an area to the east of the channel in shallower depths, between 2.5 and 4.5 m deep (Fig. 3). This echo subtype presented an irregular sub-bottom reflector at approximately 1 m under the bottom reflector located to the east of the navigation channel. Echo 6C sporadically occurred in the channel area near Ponta da Alegria (Fig. 3) between 4.5 and 7.5 m deep. The characteristic that defined this echo was the bed irregularity in a sub-bottom reflector (Fig. 11) and the eventual presence of others. The echo 6 areas were associated with the muddy sediment present in the bottom.

The deposition of fine sediments was recorded by the bottom samples in deeper areas, the navigation channel and surrounding areas. This result, in general, is in agreement with the work by Bacchi et al. (2000), which reported the presence of fine sediments under the 3-m isobath. Despite that, some deeper regions close to the channel were classified as echo 1 areas. This echo can be observed in the CS in transects that covered the northern and southern areas (Fig. 3), which must have more-consolidated muds due to the echo 1 strong reflectivity.

Echo 7

Echo 7 showed a concordant flat sub-bottom reflector (Fig. 12) and was locally mapped at Ponta da Figueira (Fig. 3), a shallow area (1 to 3 m deep) with sandy bottom. The bottom samples presented over 64% of sand with a predominance of medium sand. The thickness between the bottom and sub-bottom reflectors ranged from 0.4 to 1.1 m.

This type of echo was not found in the shallowest areas of Ponta da Figueira – between 0.6 and 1 m deep, but it occurred to the south and southwest of these regions. It also occurred parallel to the navigation channel at approximately 750 m from it. The echo-character 7 was associated with the reworking of submerged sandy sediments parallel to Ponta da Figueira. Its inclination was similar to the main orientation of the navigation channel in that area, which is towards the southwest.
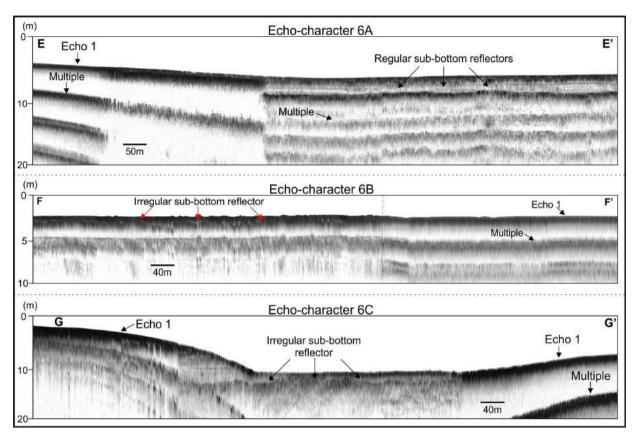
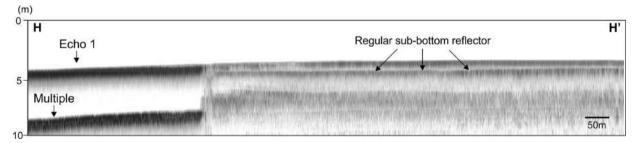**Figure 11** – Echo-character type 6 and its variations (6A, 6B, and 6C) in the CS of the Guaíba River.

Figure 12 – Echogram associated with echo 7. Presence of flat relief and concordant reflectors on the right. Echo 1 area is shown on the left.

Morphological, hydrodynamic, and evolutionary patterns of the Guaíba River

In general, the echoes associated with the deposition of fine sediments occurred in deeper areas, the navigation channel or surrounding areas. The echoes in the shallower areas presented strong acoustic reflectivity at the sites with lower deposition of fine sediments and predominance of sandy sediments. The deposition of fine sediments was confirmed in the deeper areas

with bottom samples. This result, in general, is in agreement with the work by Bacchi et al. (2000), which reported the presence of fine sediments under the 3-m isobath.

The Guaíba River flow, predominant in the north-to-south direction, presented interaction with the bottom and modification of bed forms, indicating that the flow was towards the south. The occurrence of subaqueous dunes in the Guaíba upstream end and river mouth corresponded to higher current flows in these areas. This factor indicates different types of environments that are

mainly influenced by the longitudinal section. Narrower sections lead to higher current velocities and a greater system competence regarding sediment transport. The central areas from the Guaíba River did not present subaqueous dunes, thus showing a lower transport competence. Therefore, they had lower hydrodynamic energy when compared to the upstream end and river mouth areas from this system.

The predominant north-to-south direction of the flow with currents reaching the entire water column suggests that the Guaíba system has a slope in the channel, a requirement that defines a river channel. These factors allowed us to conclude that this system has a predominant river behavior: the Guaíba River.

The progressive decrease in the current speeds in the transition from the Northern and Central sectors causing the reduction of sediment transport competence. This decrease suggests that the sand is minimal or non-existent in the Central area of Guaíba. According to Scottá et al. (submitted), the areas outside the navigation channel have velocities that are not sufficient for the sandy sediment erosion and transport under normal net river discharge conditions. Only flood conditions with high net river discharges are sufficient for the sandy sediment erosion to take place, which occur sporadically.

The high-amplitude sub-bottom reflectors of echoes 5 and 6A pointed to the position of the Jacuí River paleochannel bed, preserved in the areas of the Guaíba River navigation channel. Echoes 6B, 6C, and 7 – recorded near the navigation channel and parallel to it – indicated possible locations of the Jacuí River flood plain.

CONCLUSION

The sampled data, which included high-resolution (10 kHz) seismic profiles, side-scan sonar imaging, and geological sampling, allowed to advance and update the knowledge of the microtopography and of the geological and hydrodynamic processes in the Guaíba River. The approach focusing on seismic methods gave the support to recognize and map – in a pioneer way – the areas of occurrence of subaqueous dunes and the seismic-depositional architectural elements of the Guaíba River.

It was possible to identify, analyze, and map the sedimentary distribution of the Guaíba River bottom and sub-bottom from geoacoustic data. Fine sediments were present in deeper areas along the navigation channel or adjacent areas, which are regions of fine sediment deposition when under lower hydrodynamic energy. The occurrence and morphology of asymmetric subaqueous dunes indicated a predominant north-to-south flow and a river behavior.

REFERENCES

ANDRADE MM, SCOTTÁ FC, TOLDO Jr EE, WESCHENFELDER J & NUNES JC. 2017. Hidrodinâmica do Rio Guaíba: resultados preliminares. In: XXII Simpósio Brasileiro de Recursos Hídricos. 2017, Proceedings... Florianópolis, Brazil. ABRH, 2017.

ASHLEY GM. 1990. Classification of large-scale subaqueous bedforms: a new look at an old problem. J. Sediment. Petrol., 60(1): 160-172.

BACCHI FA, BARBOZA EG & TOLDO Jr EE. 2000. Estudo da sedimentação do Guaíba. Ecos, 17: 32-35.

BAITELLI R. 2012. Evolução Paleogeográfica do Sistema de Paleodrenagem do Rio Jacuí na Planície Costeira do Rio Grande do Sul. Doctorate Thesis, Programa de Pós-graduação em Geociências, Instituto de Geociências, Universidade Federal do Rio Grande do Sul, Brazil. 149 pp.

BAPTISTA NETO JA, SILVA MAM & FIGUEIREDO Jr AG. 1996. Sísmica de alta frequência e o padrão de distribuição de sedimentos na Enseada de Jurujuba (Baía de Guanabara) – RJ/Brasil. Brazilian Journal of Geophysics, 14(1): 51-58.

BAPTISTA NETO JA, SILVA CG, DIAS GTM & FONSECA EM. 2011. Distribuição sedimentar da Lagoa Rodrigo de Freitas através de sísmica de alta resolução. Brazilian Journal of Geophysics, 29(1): 187-195.

BARROS MVS, ROLLNIC M & WATANABE FK. 2017. Caracterização das principais feições superficiais de fundo e em subsuperfície no limite sudoeste da Baía de Macapá, canal do Norte, rio Amazonas. Trop. Oceanography, 45(1): 1-25.

BEXIGA GM. 2016. Estudo geoacústico para mapeamento de eco-caráter em registros sísmicos de alta resolução do interior da Lagoa dos Patos, RS, Brasil. Master Dissertation, Programa de Pós-Graduação em Geociências, Instituto de Geociências, Universidade Federal do Rio Grande do Sul, Brazil. 63 pp.

BOHRER MD. 2001. O aterro Praia de Belas e o aterro do Flamengo. Master Dissertation, Programa de Pesquisa e Pós-Graduação em Arquitetura, Universidade Federal do Rio Grande do Sul, Brazil. 237 pp.

BORTOLIN EC. 2017. Paleovales quaternários na Lagoa dos Patos, Rio Grande do Sul, Brasil: preenchimento, evolução e influência na dinâmica lagunar. Doctorate Thesis, Programa de Pós-graduação em Geociências, Instituto de Geociências, Universidade Federal do Rio Grande do Sul, Brazil. 113 pp.

BORTOLIN EC, WESCHENFELDER J & COOPER A. 2019. Holocene Evolution of Patos Lagoon, Brazil: The Role of Antecedent Topography. J. Coast. Res., 35(2): 357–368.

BRANCO FILHO CC. 2005. A orla do Lago Guaíba no município de Porto Alegre-RS: análise ambiental urbana e proposta de revitalização. 2005. Master Dissertation, Curso de Pós-Graduação em Geografia, Instituto de Geociências, Universidade Federal do Rio Grande do Sul, Brazil. 174 pp.

CARVALHO NO, FILIZOLA Jr NP, SANTOS PMC & LIMA JEFW. 2000. Guia de práticas sedimentométricas. ANEEL, Brasília, Brazil. 154 pp.

CATANZARO LF, BAPTISTA NETO JA, GUIMARÃES MSD & SILVA CG. 2004. Distinctive sedimentary processes in Guanabara Bay – SE/Brazil, based on the analysis of echo-character (7.0 kHz). Brazilian Journal of Geophysics, 22(1): 69-83.

CECO - Centro de Estudos de Geologia Costeira e Oceânica. 1999. Projeto Sedimentação do Complexo Guaíba. Convênio CECO/UFRGS - DVP/DEMAE, Porto Alegre, Brazil. 17 pp.

CHM - Centro de Hidrografia da Marinha. 2012. Lagoa dos Patos - De Itapuã a Porto Alegre. N. 2111. Available on: <https://www.mar.mil.br/dhn/chm/box-cartas-raster/raster_disponiveis.html>. Access on: Jan. 09, 2017.

CLARKE J, MAYER L & WELLS DE. 1996. Shallow-water imaging multibeam sonars: A new tool for investigating seafloor processes in the coastal zone and on the continental shelf. Mar. Geophys. Res., 18: 607-629.

DAMUTH JE. 1975. Echo character of the western equatorial Atlantic floor and its relationship to the dispersal and distribution of terrigenous sediments. Mar. Geol., 18(2): 17-45.

DAMUTH JE. 1980. Use of high-frequency (3.5-12 kHz) echograms in the study of near-bottom sedimentation processes in the deep-sea: a review. Mar. Geol., 38(1-3): 51-75.

DAMUTH JE & HAYES DE. 1977. Echo character of East Brazilian continental margin and its relationship to sedimentary processes. Marine Geology, 24(2): 73-95.

DMAE - Departamento Municipal de Água e Esgotos. 2018. Lago Guaíba. Available on: <http://www2.portoalegre.rs.gov.br/dmae/default.php?p_secao=197>. Access on: Feb. 13, 2018.

DNAEE - Departamento Nacional de Águas e Energia Elétrica. 1983. Mecânica de Correntes do Guaíba: Relatório Síntese. Ministério das Minas e Energia, Porto Alegre, Brazil. 61 pp.

FENSTER MS, FITZGERALD DM, BOHLEN WF, LEWIS RS & BALDWIN CT. 1990. Stability of Giant Sand Waves in Eastern Long Island Sound, U.S.A. Mar. Geol., 91(3): 207-225.

HASENACK H. 2008. Diagnóstico ambiental de Porto Alegre: Geologia, Solos, Drenagem, Vegetação/Ocupação e Paisagem. Secretaria Municipal do Meio Ambiente, Porto Alegre, Brazil. 84 pp.

HATUSHIKA RS, SILVA CG & MELLO CL. 2007. Sismoestatigrafia de alta resolução no lago Juparanã, Linhares (ES – Brasil) como base para estudos sobre a sedimentação e tectônica quaternária. Brazilian Journal of Geophysics, 25(4): 433–442.

KOTILAINEN AT & KASKELA AM. 2017. Comparison of airborne LiDAR and shipboard acoustic data in complex shallow water environments: Filling in the white ribbon zone. Mar. Geol., 385: 250-259.

MARINO IK, SANTOS MAC & SILVA CG. 2013. Processing of high-resolution, shallow seismic profiles, Guanabara Bay – Rio de Janeiro State, Brazil. Brazilian Journal of Geophysics, 31(4): 579-594.

MENEGAT R & CARRARO CC. 2009. Manual para saber por que o Guaíba é um lago. Armazém Digital, Porto Alegre, Brazil. 108 pp.

NICOLODI JL. 2007. O padrão de ondas no Lago Guaíba e sua influência nos processos de sedimentação. Doctorate Thesis, Programa de Pós-graduação em Geociências, Instituto de Geociências, Universidade Federal do Rio Grande do Sul, Brazil. 179 pp.

NICOLODI JL, TOLDO Jr EE & FARINA L. 2010. Dinâmica e ressuspensão por ondas no lago Guaíba e suas implicações nos locais de captação de água para abastecimento humano. Pesqui. Geocienc., 37(1): 25-39.

NICOLODI JL, TOLDO Jr EE & FARINA L. 2013. Dynamic and resuspension by waves and sedimentation pattern definition in low energy environments. Guaíba Lake (Brazil). Braz. J. Oceanogr., 61: 55-64.

NITSCHE FO, BELL R, CARBOTTE SM, RYAN WBF & FLOOD R. 2004. Process-related classification of acoustic data from the Hudson River Estuary. Mar. Geol., 209(1-4): 131-145.

OLIVEIRA N. 2017. Caracterização de ocorrências de gás raso na plataforma continental interna do Rio Grande do Sul. Porto Alegre. Master Dissertation, Programa de Pós-Graduação em Geociências, Instituto de Geociências, Universidade Federal do Rio Grande do Sul, Brazil. 71 pp.

PAOLO FS & MAHIQUES MM. 2008. Utilização de métodos acústicos em estudos de dinâmica costeira: exemplo na desembocadura lagunar de Cananéia. Brazilian Journal of Geophysics, 26(2): 211-225.

QUARESMA VS, BASTOS AC, LOUREIRO DV & PAIXÃO S. 2011. Utilização de métodos geofísicos para mapeamento de lama fluída no porto de Tubarão, Vitória (ES-Brasil). Brazilian Journal of Geophysics, 29(3): 487-496.

QUARESMA VS, DIAS GTM & BAPTISTA NETO JA. 2000. Caracterização da ocorrência de padrões de sonar de varredura lateral e sísmica de alta frequência (3,5 e 7,0 kHz) na porção sul da Baía de Guanabara – RJ. Brazilian Journal of Geophysics, 18(2): 201-214.

SANTOS-FISCHER CB, CORRÊA ICS, WESCHENFELDER J, TORGAN LC & STONE JR. 2016. Paleoenvironmental insights into the Quaternary evolution of the southern Brazilian coast based on fossil and modern diatom assemblages. Palaeogeography, Palaeoclimatology, Palaeoecology, 446: 108-124.

SANTOS-FISCHER CB, WESCHENFELDER J, CORRÊA ICS, STONE JR, DEHNHARDT BA & BORTOLIN EC. 2018. A Drowned Lagunar Channel in the Southern Brazilian Coast in Response to the 8.2-ka Event: Diatom and Seismic Stratigraphy. Estuaries and Coasts, 41: 1601-1625.

SCOTTÁ FC, ANDRADE MM, WESCHENFELDER J, TOLDO Jr EE & NUNES JC. 2019. Descarga líquida e sólida em suspensão do sistema Guaíba. Pesq. Geoc. Unpublished.

SILVA Jr VO. 2017. Identificação geoacústica de ecofácies de fundo e subfundo da porção norte do Lago Guaíba, RS. Trabalho de Conclusão de Curso em Geologia. Instituto de Geociências, Universidade Federal do Rio Grande do Sul, Brazil. 64 pp.

SILVA AE, MENANDRO PS, NASCIMENTO KA, QUARESMA VS & BASTOS AC. 2014. Interpretation of sedimentary processes using echo-character distribution: case study of Piraquê-Açu and Piraquê-Mirim estuarine system, Aracruz – ES (Brazil). Brazilian Journal of Geophysics, 32(2): 301-309.

SOUZA LAP. 2006. Revisão Crítica da Aplicabilidade dos Métodos Geofísicos na Investigação de áreas submersas rasas. Doctorate Thesis, Curso de Oceanografia Química e Geológica, Universidade de São Paulo, Brazil. 311 pp.

TOLDO Jr EE & ALMEIDA LESB. 2009. Rio Guaíba. PROCEMPA, Porto Alegre, Brazil. 7 pp.

TOLDO Jr EE, DILLENBURG SR, CORREA ICS & ALMEIDA LESB. 2000. Holocene sedimentation in Lagoa dos Patos Lagoon, Rio Grande do Sul, Brazil. J. Coast. Res., 16(3): 816-822.

VERONEZ Jr P, BASTOS AC, PIZZIN BF, GAVA RD, QUARESMA VS & SILVA CG. 2009a. Sonar de varredura lateral e sísmica de alta resolução aplicados no estudo de ecofácies na Baía de Vitória - ES. Brazilian Journal of Geophysics, 27(3): 411-425.

VERONEZ Jr P, BASTOS AC & QUARESMA VS. 2009b. Morfologia e distribuição sedimentar em um sistema estuarino tropical: Baía de Vitória, ES. Brazilian Journal of Geophysics, 27(4): 609-624.

WESCHENFELDER J, CORRÊA ICS, ALIOTTA S, PEREIRA CM & VASCONCELLOS VEB. 2006. Shallow gas accumulation in sediments of the Patos Lagoon, southern Brazil. An. Acad. Bras. Ciênc., 78(3): 607-614.

WESCHENFELDER J, CORRÊA ICS, ALIOTTA S & BAITELLI R. 2010. Paleochannels related to late Quaternary sea-level changes in Southern Brazil. Braz. J. Oceanogr., 58: 35-44.

WESCHENFELDER J, BAITELLI R, CORRÊA ICS, BORTOLIN EC & SANTOS-FISCHER CB. 2014. Paleochannels related to late Quaternary sea-level changes in Southern Brazil. J. South Am. Earth Sci., 55: 83-93.

WESCHENFELDER J, KLEIN AHF, GREEN NA, ALIOTTA S, DE MAHIQUES MM, AYRES NETO A, TERRA LC, CORRÊA ICS, CALLIARI LJ, MONTOYA I, GINSBERG SS & GRIEP GH. 2016. The control of palaeo-topography in the preservation of shallow gas accumulation: Examples from Brazil, Argentina and South Africa. Estuar. Coast. Mar. Sci., 172: 93-107.